Frequency-Resolved Ultrafast Dynamics of Phonon Polariton Wavepackets in the Ferroelectric Crystals LiNbO$_3$ and LiTaO$_3$.

DISSERTATION

Zur Erlangung des akademischen Grades

„Doctor rerum naturalium "

(Dr. rer. nat.)
in der Wissenschaftsdisziplin: Experimentalphysik

eingereicht an der

Mathematisch-Naturwissenschaftlichen Fakultät
der Universität Potsdam

von

Jewgenij Goldshteyn

geboren am 22.01.1983 in Saporoge, Ukraine

Selbständigkeitserklärung:

Hiermit erkläre ich, dass ich die vorliegende Dissertation **Frequency-Resolved Ultrafast Dynamics of Phonon Polariton Wavepackets in the Ferroelectric Crystals LiNbO₃ and LiTaO₃** selbständig erarbeitet und verfasst habe und alle Hilfsmittel und Hilfen angegeben habe. Ich erkläre weiterhin, dass ich mich nicht für einen Doktorgrad anderwärts beworben habe und auch den dementsprechenden Doktorgrad nicht besitze. Desweiteren erkläre ich, dass ich von der zugrunde liegenden Promotionsordnung Kenntnis genommen habe.

Potsdam, den 25. Juni 2014   Jewgenij Goldshteyn

Abstract

During this work I built a four wave mixing setup for the time-resolved femtosecond spectroscopy of Raman-active lattice modes. This setup enables to study the selective excitation of phonon polaritons. These quasi-particles arise from the coupling of electro-magnetic waves and transverse optical lattice modes, the so-called phonons. The phonon polaritons were investigated in the optically non-linear, ferroelectric crystals $LiNbO_3$ and $LiTaO_3$.

The direct observation of the frequency shift of the scattered narrow bandwidth probe pulses proofs the role of the Raman interaction during the probe and excitation process of phonon polaritons. I compare this experimental method with the measurement where ultra-short laser pulses are used. The frequency shift remains obscured by the relative broad bandwidth of these laser pulses. In an experiment with narrow bandwidth probe pulses, the Stokes and anti-Stokes intensities are spectrally separated. They are assigned to the corresponding counter-propagating wavepackets of phonon polaritons. Thus, the dynamics of these wavepackets was separately studied. Based on these findings, I develop the mathematical description of the so-called homodyne detection of light for the case of light scattering from counter propagating phonon polaritons.

Further, I modified the broad bandwidth of the ultra-short pump pulses using bandpass filters to generate two pump pulses with non-overlapping spectra. This enables the frequency-selective excitation of polariton modes in the sample, which allows me to observe even very weak polariton modes in $LiNbO_3$ or $LiTaO_3$ that belong to the higher branches of the dispersion relation of phonon polaritons. The experimentally determined dispersion relation of the phonon polaritons could therefore be extended and compared to theoretical models. In addition, I determined the frequency-dependent damping of phonon polaritons.

Zusammenfassung

Während dieser Arbeit habe ich ein optisches Vier-Wellen-Misch-Experiment aufgebaut, um zeitaufgelöste Femtosekunden-Spektroskopie von Raman-aktiven Gittermoden durchzuführen. Dieser Aufbau erlaubt die Untersuchung selektiv angeregter Phonon Polaritonen. Diese Quasiteilchen entstehen durch die Kopplung von elektromagnetischen Wellen und transversal-optischer Gittermoden, den sogenannten Phononen. Die Phonon Polaritonen wurden in den optisch nichtlinearen, ferroelektrischen Kristallen $LiNbO_3$ und $LiTaO_3$ untersucht.

Durch die direkte Beobachtung der Frequenzverschiebung der gestreuten, schmalbandigen Abfragepulse konnte die Raman-Wechselwirkung im Abfrage- und Erzeugungsprozess von Phonon Polaritonen nachgewiesen werden. Diese experimentelle Methode vergleiche ich mit der Messung mittels ultrakurzen Laserpulsen. Hierbei ist die Frequenzverschiebung wegen der relativ großen Bandbreite der Laserpulse nicht auflösbar. Die Stokes- und Anti-Stokes-Intensitäten sind hingegen in einem Experiment mit schmalbandigen Abfragepulsen spektral getrennt. Diese konnten den jeweiligen, entgegengesetzt propagierenden Wellenpaketen der Phonon Polaritonen zugeordnet werden. Deshalb war es möglich, die Dynamik dieser Wellenpakete einzeln zu untersuchen. Basierend auf diesen Erkenntnissen konnte ich eine mathematische Beschreibung der sogenannten homodynen Detektion des Lichtes für den Fall von Lichtstreuung an entgegengesetzt propagierenden Phonon Polaritonen entwickeln.

Desweiteren habe ich die breitbandigen, ultrakurzen Pumppulse mithilfe von zwei Bandpassfiltern so modifiziert, dass zwei spektral unterschiedliche und spektral nicht überlappende Anregepulse zur Verfügung standen. Dadurch wurde die frequenz-selektive Anregung von Polariton-Moden in der Probe ermöglicht. Diese Technik erlaubt mir die Untersuchung auch sehr schwacher Gittermoden in $LiNbO_3$ und $LiTaO_3$, die zu den höheren Ästen der Dispersionsrelation der Phonon Polaritonen gehören. Die experimentell bestimmte Dispersionsrelation der Phonon Polaritonen wurde erweitert und mit theoretischen Modellen verglichen. Zusätzlich habe ich die frequenzabhängige Dämpfung der Phonon Polaritonen bestimmt.

Contents

1 Introduction

The rapid progress in the field of signal processing, telecommunication technology, and processor technology continues for more than thirty years. Beside the miniaturization of integrated circuits in microelectronics, the speed of data processing continuously increases and nowadays is in the frequency range of several gigahertz. Slowly, a frequency regime is reached at which the functionality of the electronic circuits starts to fail. Therefore, recent developments try for instance implementing the optical data communication in order to overcome these limitations. However, most dielectric materials have optical active modes in the far-infrared spectral region and hence absorb strongly at these frequencies. In this region, the signals are neither transported as current nor as light but as a mixed mode consisting of electromagnetic radiation and a vibrational mode of the polar dielectric medium. These modes first discovered by Henry *et al.* [1] can be described as quasi-particles and commonly called phonon polaritons. Their existence had previously been predicted by Huang [2,3]. These quasi-particles can coherently be excited via optical rectification or difference frequency generation (DFG) of optical light that undergoes Raman scattering. The first experimental and theoretical investigations of phonon polaritons and their interaction with light were made in the mid-sixties of the last century [4–6]. However, it was only after the progress in femtosecond-pulse generation in laser science in the mid-eighties that phonon polaritons could coherently be excited. More than ten years later, an improved wavevector selective excitation of these wavepackets was experimentally demonstrated [7]. An important outcome of these studies is the use of phonon polaritons as an efficient source for intense ultra-short terahertz radiation [8,9].

In this thesis, the transient dynamics of impulsively excited phonon polaritons in optically non-linear $LiNbO_3$ are investigated. During this work, several different aspects concerning the physics of phonon polaritons were covered. In the following, the most important findings are summarized. These are:

Wavevector-selective excitation of phonon polaritons

The wavevector-selective excitation of phonon polaritons leads to an excitation of narrow bandwidth wavepackets. This is achieved using the so-called transient grating geometry of the pump pulses. This approach allows investigating the dynamics of phonon polaritons as function of the wavevector. The generation of polariton modes with low damping ensures a long propagation

distance and hence allows their detailed examination at a region that is spatially well-separated from the excitation region. For probing of the coherent phonon polaritons variably delayed ultra-short laser pulses are used. This corresponds to impulsive stimulated Raman scattering (ISRS) experiment performed in the time domain. A complimentary experiment is performed using narrow bandwidth probe pulses and employing a spectrometer to resolve the inelastic light scattering process. This elegantly verifies the role of the Raman mechanism in the pump and probe process. Moreover, the data obtained in the frequency domain are used for the unambiguous interpretation of transients observed in the time domain.

Measurement of the dispersion relation of phonon polaritons in LiNbO$_3$

As a consequence of the selective excitation of phonon polaritons, the direct mapping of their dispersion relation is possible. The experiment with temporally short probe pulses measures the dispersion relation of phonon polaritons, which allows to determine the frequency-dependence of the real and imaginary parts of the phonon polariton wavevector. The use of a spectrometer and narrow bandwidth probe pulses allows detecting energetically higher lying and only weakly excited polariton modes that were not observed in the ISRS experiments with short probe pulses. This also means that the measurement of the dispersion relation in this work is extended toward higher wavevectors, away from the classical polariton region. As a consequence, studying the transition from the mixed state of the phonon polariton toward the pure phonon state it becomes possible.

Wavevector-dependent damping of phonon polaritons in LiNbO$_3$

The frequency-dependent damping of phonon polaritons is close related to the imaginary part of the complex dispersion relation of phonon polaritons. The lower dispersion branch, which approaches the frequency of the lowest phonon mode in LiNbO$_3$, is measured with temporally short pulses. The appearance of an additional coupling mechanism to other low-frequency modes is observed. This coupling leads to an increase of the damping rate of the phonon polaritons. These findings could be of great interest for the generation of terahertz radiation via optical rectification of visible laser light in non-linear crystals with subsequent excitation of phonon polaritons. Especially, the efficiency of the terahertz radiation, which can be coupled out, is very sensitive to its absorption in the material.

Frequency-selective preparation of single narrow-band wavepackets of phonon polaritons

Using pump pulses with narrow bandwidths and different content of spectral components leads to an excitation of phonon polaritons with a certain frequency and well-defined direction of propagation. In addition, this is advantageous for the study of weak optically active modes of

solids, which are selectively enhanced. It allows us to overcome the interference of scattered light from simultaneously generated counter-propagating phonon polaritons. The relative efficiency of the generation of a single polariton wavepacket is higher than for the case of the excitation with spectrally broad pulses.

This thesis is structured as follows: in chapter 2 an introduction to the properties of the phonon polaritons in $LiNbO_3$, such as their dispersion relation and group velocity, is given. The impulsively stimulated excitation and the subsequent detection processes of phonon polaritons are explained in detail. Both are explained in the context of stimulated Raman scattering and difference frequency generation. The relation between both models is illustrated. The optical four wave mixing setup, which has been used in this work, is discussed in detail in chapter 3. The spectral and temporal characterization of the pump and probe pulses is explained and the uncertainty of the selectively excited wavevector of the phonon polaritons is discussed. In chapter 4 the observation of the impulsively stimulated wavepackets of phonon polaritons in $LiNbO_3$ is exemplarily presented for the cases of broad and narrow bandwidth probe pulses. The advantages and limits of both measurement methods in the context of the mapping of the dispersion relation of phonon polaritons is elucidated. Both methods are compared and the wavevector and frequency selectivity of the excitation and detection in the transient grating geometry is discussed in detail. Different mechanisms that cause a spectral broadening of the spectrum of the excited phonon polaritons are examined. Chapter 5 deals with the so-called homodyne detection scheme in the four wave mixing experiment with phonon polaritons. The probe light simultaneously undergoes Raman scattering from left- and right-propagating phonon polaritons and subsequently mix on the detector. A mathematical description of the frequency resolved detection of the scattered light fields with a spectrometer is developed. The special cases of the homodyne detection that intrinsically occurred during this work, namely the cases of a negligible elastic Rayleigh contribution, a displaced probe region with respect to the excitation region, a detection with spectrally narrow probe pulses, and an increased contribution of Rayleigh light due to light scattering from impurities, are discussed. The following chapter 6 covers the observation of propagating wavepackets of phonon polaritons for which the probe region is displaced with respect to the excitation volume. Both, narrow and broad bandwidth measurements are compared. In chapter 7.1 the frequency-selective excitation of phonon polaritons is realized by modifying the spectra of both pump pulses. This allows to prepare a single polariton wavepacket with a well-defined direction of propagation. Moreover, a polariton mode of the second dispersion branch of $LiNbO_3$ is uncovered by the selective enhancement using this narrow bandwidth excitation. In chapter 8 the measured dispersion relation of phonon polaritons in $LiNbO_3$ is discussed. The fitting of a theoretical dispersion function is illustrated and the result

is compared to the calculated dispersion relations of phonon polaritons with different sets of parameters taken from the literature. Chapter 9 discusses the frequency-dependent damping of phonon polaritons in $LiNbO_3$. The data are corrected for the effect of polaritons leaving the observation volume. The obtained sub-structure in the damping rate of phonon polaritons indicates additional damping contributions, which can be explained by assuming a coupling to low-frequency defect modes in $LiNbO_3$. In chapter 10 an outlook on the measurement of impulsively excited phonon polaritons in $LiTaO_3$ and to the detection of the transient lattice changes, which are caused by impulsively excited phonon polaritons, by means of ultrafast X-ray diffraction (UXRD) is given.

2 Background

This work concentrates on the investigation of coherently excited optical modes in the optically non-linear insulator $LiNbO_3$. The used experimental technique is based on transient grating pump-probe experiment. The time-resolved spectroscopic observations of the laser generated and selectively excited vibrational and polar lattice modes reveal ultrafast dissipation and propagation dynamics. In this chapter the basic physics that are necessary for the understanding of the interaction of intense light pulses with condensed matter, namely non-linear optical effects, the propagation of electromagnetic fields in a dispersive medium, and inelastic light scattering (Raman scattering), is introduced. The experimental methods described in this thesis rely on the generation of femtosecond (fs) laser pulses, which provide large intensities in order to drive non-linear light-matter interactions. Ultra-short laser pulse generation is covered extensively in the literature [10, 11].

This chapter opens with a brief overview of the crystal structure of $LiNbO_3$ (2.1). Next, the optical and non-linear optical properties that are of special interest in the course of this thesis are addressed (2.2). In the same section the Raman and infrared spectroscopic measurements of optical phonons in $LiNbO_3$ are presented and the dielectric function in the terahertz region is derived. Hereafter, the physics of the phonon polariton, particularly the complex dispersion relation and the group velocity of phonon polaritons in $LiNbO_3$ are thoroughly discussed in section 2.3. In section 2.4 the excitation of phonon polaritons in the transient grating geometry by two optical pulses is described in the view of energy and momentum conservation by three interacting particles. In the same section the excitation process is illustrated on the basis of the Cherenkov-like radiation emission from a transient optical grating in the material. A closer look is taken on the issue of the non-linear optical microscopic generation process of phonon polariton wavepackets at the end of section 2.4. Finally, the optical probing of phonon polaritons is discussed in section 2.5 considering stimulated Raman scattering, non-linear wave mixing, and diffraction from the transient modulation of the refractive index.

2.1 Crystal Structure of $LiNbO_3$

Lithium niobate is a chemical compound with the formula $LiNbO_3$. It is a transparent, colorless and crystalline solid material that is not found in the nature. The single crystals of lithium

niobate are usually grown using the Czochralski method [12]. Lithium niobate belongs to the group of materials that crystallize in a perovskite unit cell. At room temperature the unit cell is doubled along the optical c-axis and exhibits the lattice constants $a_H = 5.142$ Å and $c_H = 13.863$ Å [13]. This is described by the distorted trigonal crystal system with the space group $R3c$ and point group $3m$ [14]. This structure is shown in figure 2.1 and lacks inversion symmetry. The central cation Li^{1+} and Nb^{5+} are displaced from the centrosymmetric position into directions along the c-axis with respect to the centers of the oxygen planes or the centers between two oxygen planes, respectively. The displacement is of the order of $x \sim 0.55$ Å for lithium and $x \sim 0.26$ Å for the oxygen octahedron [13]. This corresponds to a relative displacement of $x/c_H \sim 0.04$ and $x/a_H \sim 0.019$, respectively. Consequently, the unit cell experiences an electrical polarization $P_s = 71$ μC cm^{-2} [15]. The volume of the hexagonal unit cell amounts to $V = 318$ Å^3. $LiNbO_3$ is a well-known ferroelectric material [16] with a relatively high Curie point of $T_C = 1167°C$ [13] as well as a high melting point $T_m = 1260°C$. The exact stoichiometry of the sample strongly influences the Curie temperature and other physical properties [17, 18]. The ferroelectric-to-paraelectric phase transition involves a softening of the ferroelectric soft modes with temperature approaching towards T_C [19]. This issue is closely related to the polarizability of the phonon and phonon polariton modes.

2.2 Optical Properties of LiNbO$_3$

The next sections deal with characteristic physical properties of $LiNbO_3$ that determine the interaction of the laser light with the sample. First, the visible range of the radiation is considered in section 2.2.1 because the wavelength of the used laser system is centered around 800 nm. In section 2.2.2 the terahertz range is discussed where the optical phonon modes determine the dielectric constant of the material (sec. 2.2.3) and thus are of great importance for the description of the propagation of the electromagnetic radiation in this frequency range and particularly of the phonon polaritons.

2.2.1 Linear and Non-Linear Optical Properties of LiNbO$_3$

$LiNbO_3$ is an insulator and thus transparent in the spectral region from 320 nm to 5600 nm. The indirect band gap is at 3.78 eV (330 nm) [20]. An interband transition driven by a two photon absorption process is expected to occur below 1.9 eV (660 nm). Thus no interband transition or resonant excitation effects are expected in the experiments which are here conducted with 800 nm light. $LiNbO_3$ single crystals are birefringent with the optical axis oriented parallel to the tetragonal c-axis of the crystal. For 800 nm light the values of the ordinary and the extra-ordinary refractive index are $n_0(800 \text{ nm}) = 2.257$ and $n_e(800 \text{ nm}) = 2.163$, respectively [21].
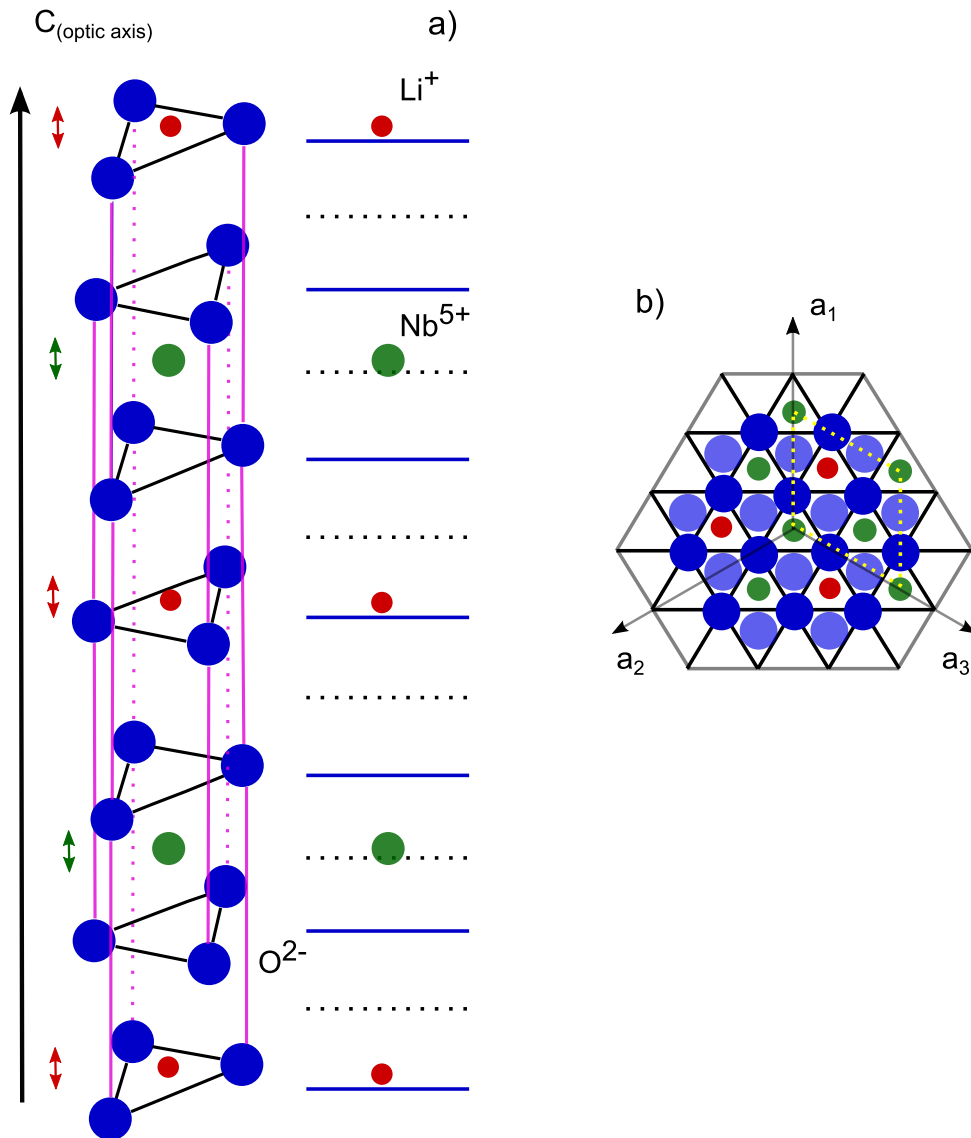
Figure 2.1: The crystal structure of LiNbO$_3$ in the ferroelectric phase below $T_c \sim 1170$ after Abrahams *et al.* [14]. a) Sequence of distorted octahedra along the polar c-axis. The positions of the oxygen layers and the position of the centers between the oxygen layers are indicated by the blue and black dashed lines, respectively. The position of Li^{+1} and Nb^{+5} is also drown. The unit cell is doubled along the *c*-axis. The A$_1$ vibrational mode is indicated by the red and green arrows, which show the displacement of Li^{+1} and Nb^{+5} ions relative to the oxygen planes. b) View down the *c*-axis. The dark blue oxygen atoms form the top layer and the light blue oxygen atoms the bottom layer. The hexagonal unit cell is indicated by the yellow dashed line.

At room temperature the non-centrosymmetric unit cell is the reason for several pronounced non-linear optical effects: the observed $\chi^{(2)}$ processes during this work are the sum frequency

generation (SFG), second harmonic generation (SHG) and difference frequency generation (DFG).
The electro-optic tensor [22], $\bar{\bar{T}}$, consist of the following elements:

$$\bar{\bar{T}} = \begin{pmatrix} 0 & -r_{22} & r_{13} \\ 0 & r_{22} & r_{13} \\ 0 & 0 & r_{33} \\ 0 & r_{51} & 0 \\ r_{51} & 0 & 0 \\ -r_{22} & 0 & 0 \end{pmatrix}, \tag{2.1}$$

with $r_{13} = 9.6$, $r_{22} = 6.8$, $r_{33} = 30.9$, $r_{51} = 21.1$ [23] (all values are given in (pm/V)). The largest
coefficient is r_{33}. For incident light polarized along the c-axis–this case applies for the experiments
discussed in this work–only this element contributes to the DFG and leads to the highest possible
generation efficiency of the phonon polaritons in LiNbO$_3$ [24]. Note, the electro-optic coefficients
r_{ijk} are related to the non-linear optical coefficients for the optical rectification d_{ijk} via the
relation $d_{ijk} = -0.25 \cdot r_{ijk} \cdot n_{vis}^4$, where n_{vis} is the refractive index in the visible range [25, 26], in
our case $n_{vis} = n_e = 2.163$ and $d_{33} = -169$ pm/V.

2.2.2 Infrared- and Raman-Active Phonon Modes in LiNbO$_3$

Infrared- and Raman-active phonon modes in polar LiNbO$_3$ crystal were intensively studied by
infrared reflectivity measurements [27] and conventional Raman scattering technique [19, 27]. A
more recent Raman measurement is shown in figure 2.2 by the black circles. Four transverse
optical (TO) modes are observed which have an A_{1g}-symmetry and the associated displacements
point parallel to the optical axis (c-axis), as indicated in figure 2.1. The Raman tensor $\bar{\bar{R}}$, which
describes coupling of visible light to optical phonon modes, is given by [27]:

$$\bar{\bar{R}} = \begin{pmatrix} a & 0 & 0 \\ 0 & a & 0 \\ 0 & 0 & b \end{pmatrix}. \tag{2.2}$$

Again, the largest element of the tensor is the b. The Raman lines in figure 2.2 can be analyzed to
obtain information about the central frequency υ, the linewidth γ, and the integrated intensity A
under the four resonances that correspond to the four TO phonons. The determined parameters
will be used later for the calculation of the dielectric function and the dispersion relation of
phonon polaritons in section 2.2.3 and 2.3.1, respectively. These parameters are obtained using a
fit analysis with Lorentzian functions. The result is shown in figure 2.2 as red circles. The values
are summarized in the third column of table 2.1. Note, the integrated intensity A is in general
not directly proportional to the infrared absorption strength of a mode, because the Raman
polarizability influences the cross-section in Raman scattering experiments [4, 30]. In the second
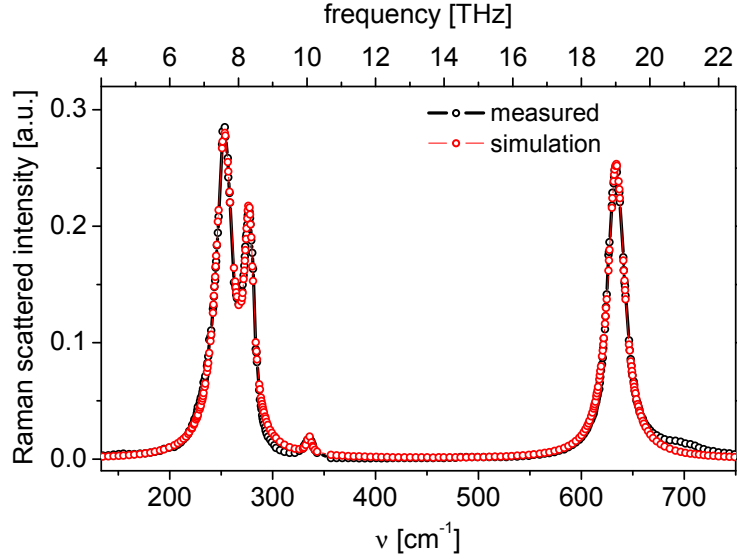
Figure 2.2: Raman $x(zz)y$ spectrum (black circles) of a nearly stoichiometric LiNbO$_3$ sample measured at room temperature (after reference [28]). Four transverse optical (TO) modes are visible at 252.9, 277.1, 335.5 and 633.9 cm^{-1}. The fitted spectrum (red circles) assumes a Lorentzian line shapes. The fit parameters are tabulated in table 2.1 on the right side. The nomenclature of $x(zz)y$ is as follows: x and y denotes the direction of incoming and scattered light with respect to the principal axis of the examined crystal. The first and second latter denotes the orientation of the polarization of the same incoming and scattered light. For more details see reference [29].

column of table 2.1 the Raman parameters from reference [27] are given that are often cited by authors discussing the phonon polariton dispersion relation. The parameters determined by the analysis of the Raman data exhibit smaller damping rates for the first, second and fourth mode compared to the Raman study reported by Barker and Loudon [27] and which are listed in the second column of table 2.1. On the other hand, the values of the damping are very close to the ones determined from the infrared reflectivity measurement [27] that are listed in the first column.

2.2.3 Dielectric Function in the Terahertz Region of LiNbO$_3$

The propagation of electromagnetic fields in media is determined by the complex dielectric function $\epsilon(\omega)$. In the terahertz region ($\omega \sim 10^{13}$ Hz), the polar modes of a solid dominate the ionic part of the dielectric function and $\epsilon(\omega)$ diverges as it approaches the resonance of an infrared active TO-mode. The dielectric function is described by the Lorentzian form

$$\epsilon(\omega) = \epsilon_\infty + \sum_{i=1}^{4} \frac{(\epsilon_{0,i} - \epsilon_\infty)\omega_{T,i}^2}{\omega_{T,i}^2 - \omega^2 - i\Gamma_i\omega} \quad , \tag{2.3}$$

i	v (cm^{-1})	Γ (cm^{-1})	S	v (cm^{-1})	Γ (cm^{-1})	v (cm^{-1})	Γ (cm^{-1})	A
1	248	21	16.0	252	28	252.9	19.9	9.5
2	274	14	1.0	276	20	277.1	11.1	3.5
3	333	25	0.16	333	13	335.5	5.8	0.15
4	628	34	2.55	634	28	633.9	20.0	8.85
	ϵ_∞ = 4.6							

Table 2.1: Room temperature central frequency v, linewidth Γ, integral intensity A of the Raman line, and absorption strength S of the four TO phonons in LiNbO$_3$ with the E-field polarized parallel to the c-axis. First column: parameters are obtained from an infrared reflectivity measurement [27]. Second column: parameters are determined from a conventional Raman scattering experiment [27]. Third column: parameters as obtained by the analysis of the Raman scattering data from reference [28].

where ϵ_∞ is the high frequency dielectric constant, $\epsilon_{0,1} = \epsilon(\omega = 0)$ is the low frequency dielectric constant, $\omega_{T,i}$ is the frequency of the (TO) phonon mode i, Γ_i is the phenomenological damping factor of the resonance i. The quantity $S_i = \epsilon_{0,i} - \epsilon_\infty$ is the oscillator strength of the resonance i. In the case of LiNbO$_3$ the sum takes into account four infrared-active modes which are for example observed by conventional Raman scattering studies [28].

In figure 2.3 the obtained real and the imaginary parts of the dielectric function $\epsilon(\omega) = \epsilon_{r,1}(\omega) + i\epsilon_{i,1}(\omega)$ of LiNbO$_3$ are depicted. The imaginary part $\epsilon_{i,1}(\omega)$ exhibits a maximum at the resonance frequency ω_{TO} of a TO phonon mode. At the same time the real part $\epsilon_{r,1}(\omega)$ increases as it passes one resonance by the value of its oscillator strength S. In the frequency region where the real part $\epsilon_{r,1}(\omega)$ is negative, the propagation of electromagnetic waves in medium is impossible. The so-called Reststrahlen band of the medium is indicated by the points (1) and (2) in figure 2.3. Thus the electromagnetic waves are reflected from the sample surface.

The situation for $\epsilon_{r,2}(\omega)$ is different. Although the integrated intensity A of the Raman line is not equal to the oscillator strength S, A can be used for the calculation of the dielectric function. In other words, the different Raman polarizabilities [4,30] of the phonon modes are neglected and it is consequently assumed that $A \approx S$. The used strength A together with the lower damping rates of the resonances cause a region (indicated by point (3)) inside the Reststrahlen band where the real part is positive. In the small range around $\omega = 8.15$ THz (272 cm^{-1}) the propagation of electromagnetic waves becomes allowed. The mathematical condition for the positive value
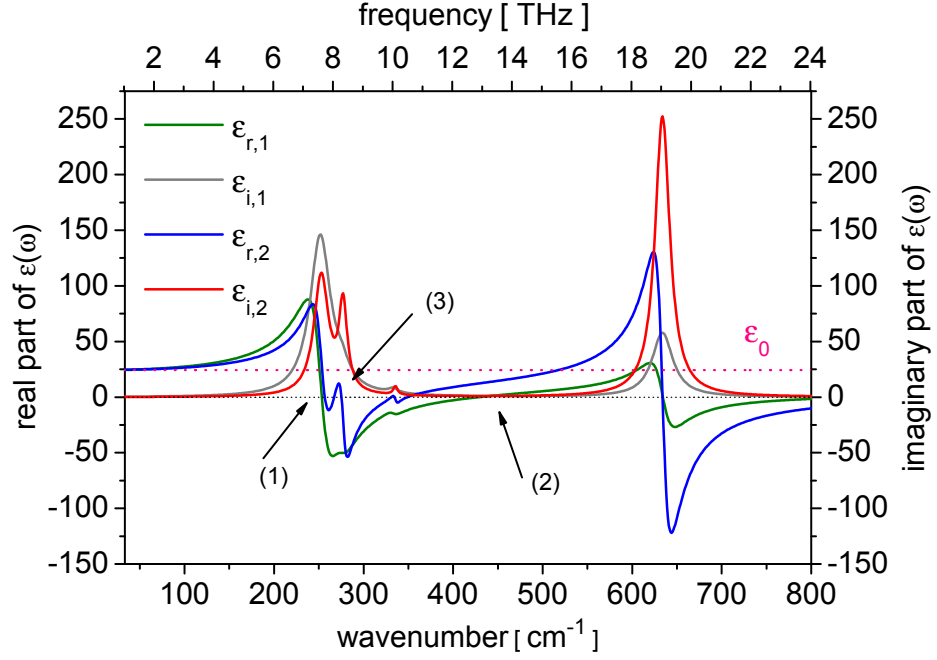
Figure 2.3: Derived real ϵ_r and imaginary ϵ_i part of the dielectric function of LiNbO$_3$ using the equation 2.3 and parameters from the literature [27] (1) or from the analysis of the measured Raman [28] spectrum (2). In the frequency region between the point (1) and point (2) the real part (green line) of the dielectric function becomes negative. This frequency range is named the Reststrahlen band. Around 8 THz at point (3) $\epsilon_{r,2}$ gets positive indicating allowed phonon polariton states inside the Reststrahlen band. The low-frequency constant ϵ_0 is depicted by the pink line.

of the real part of the dielectric function is dependent on the strength, damping and central frequency of the two phonon modes under discussion.

2.3 Phonon Polaritons in LiNbO$_3$

The coupling of a terahertz light field to a transverse optical vibrational mode of an ionic lattice is described by a quasi-particle that is called phonon polariton. This concept can be applied in the region where the frequency of the light and the phonon mode match. Hence, the frequency of a phonon polariton exhibits a strong dispersion. In the following sections, the properties of phonon polaritons and their interaction with light are discussed.

2.3.1 Dispersion Relation of Phonon Polaritons in LiNbO$_3$

The nature of a phonon polariton and consequently the shape of its dispersion relation are determined by the coupling between the terahertz light and the TO phonon. In figure 2.4 the

unperturbed dispersion relations of a TO phonon ω_{TO} and terahertz light c/n_{THz} are shown by the dark green and dark blue line, respectively. The light field strongly couples to a TO-mode in the region where the frequency ω and the wavevector q are similar for both. The dispersion relation of a phonon polariton $\omega_{pp}(q)$ can be calculated from the following equation[1]:
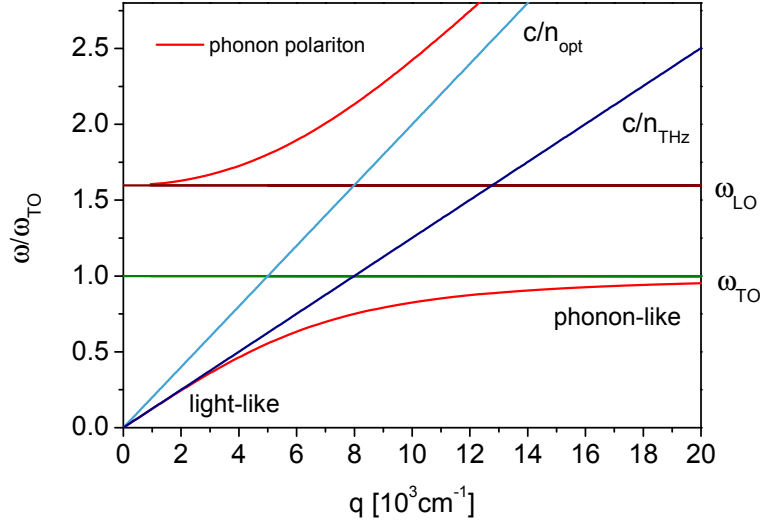
Figure 2.4: Dispersion relation of phonon polaritons (red line) in a dielectric material with an assumption of light coupling to only one TO phonon mode. The branches of the unperturbed TO phonon (dark green line), the light below (dark blue line) and above (light blue line) the resonance are indicted. The frequency of the LO mode, which is defined as the root of the dielectric function above the resonance frequency ω_{TO}, is shown by the brown line.

$$\omega_{pp} = \frac{c_o}{\sqrt{\epsilon(\omega)}}q \quad , \tag{2.4}$$

with the frequency-dependent dielectric function $\epsilon(\omega)$ from equation 2.3. In figure 2.4 the calculated dispersion relation of phonon polaritons is shown by the red line for the case of one phonon mode. Near the phonon resonance frequency the phonon polaritons become mostly phonon-like. They exhibit a large damping and behave like a standing wave with almost negligible group velocity v_g. For the lower phonon polariton branch, that is for $\omega_{pp}{<}\omega_{\text{TO}}$, this is true for large wavevectors q.

In the regions where the polariton dispersion approaches the linear dispersion of light, the polariton exhibits mostly light-like properties: it propagates with the speed of light in the medium and shows a linear dispersion. For the lower polariton branch this case applies for small wavevectors q of phonon polaritons. In the intermediate frequency region phonon polaritons

---

[1]Because of the relatively large thickness of the sample (~ 0.5 mm), waveguide effects are not important in this work.
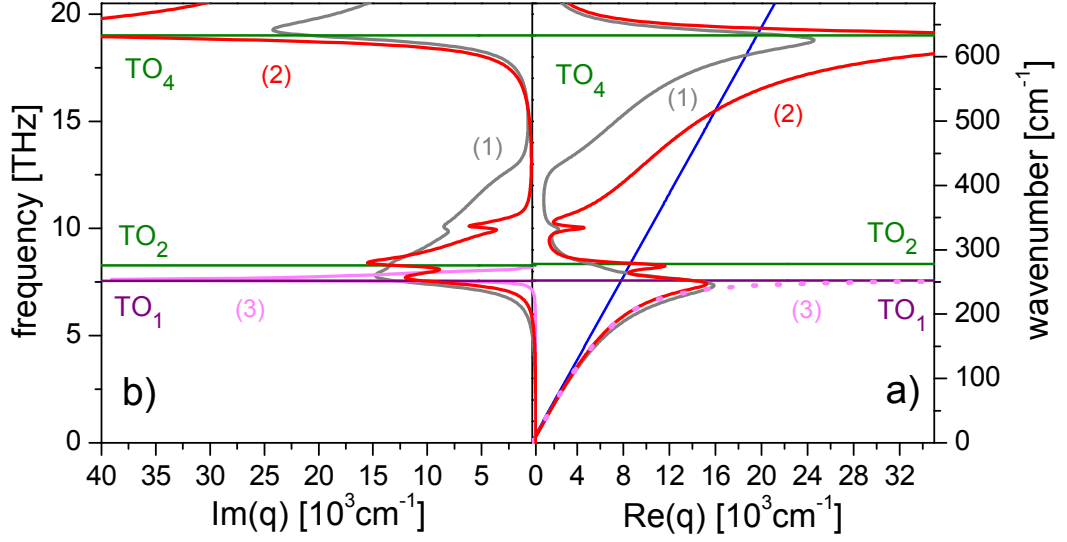
Figure 2.5: Calculated dispersion relation of phonon polariton in LiNbO_3. a) The real part of the polariton wavevector q versus frequency. The unperturbed light (blue line) and three phonon branches TO_1, TO_2, TO_4 are shown. The dispersion is calculated using equation 2.4 and 2.3 with the parameters, which were obtained by infrared reflectivity from reference [27] (gray line (1)), using the values obtained by the analysis of the Raman scattering data from reference [28] (red line (2)), and using the data from the Raman analysis but with ten times smaller damping rates (pink line (3)) according to Barker and Loudon [6]. b) The imaginary part of the phonon polariton wavevector q–which describes the damping–is plotted versus frequency. The curves have the same color code as in a). Note, the absorption coefficient α in the law of Lambert is related to the imaginary part of the polariton wavevector q via $\alpha(\omega) = 2\text{Im}(q(\omega))$.

exhibit both, light and phonon character. The more complicated dispersion relation of phonon polaritons in LiNbO_3 is shown in figure 2.5a. Here, four TO modes have to be considered which couple to the light in the terahertz region. Three different parameter sets are used to calculate the polariton dispersion relation: (1) values taken from reference [27], (2) values obtained from the analysis of the Raman scattering data from Ref. [28], and (3) the same parameters as in (2) but with the damping rates decreased by a factor of 10. The latter set resembles to the previously discussed simple dispersion relation that considers only one TO mode and which is

most commonly discussed in the solid state physics literature [31–33]. The difference of these different calculations of the lower polariton branch (between (1) and (2) in figure 2.5a) amounts up to 0.25 THz. As can clearly been seen in figure 2.5b, the deviation is much larger for the higher polariton branch.

Figure 2.5b shows corresponding frequency ω_{pp} plotted against the imaginary part of the polariton wavevector, q. This representation of the dispersion is proportional to the frequency-dependent damping of the phonon polaritons. Its magnitude increases as expected in the vicinity of a phonon resonance, as it is evident for example from the red line. Around a frequency of 8 THz, a local minimum of the damping is observed whereas the real part of q in figure 2.5a rises toward $\omega_{pp} = \omega_{TO,2}$. Thus, the life-time of the polariton states increases here which is a indication of allowed polariton modes.

2.3.2 Group and Energy Velocity of Phonon Polariton Wavepackets

The envelope of a wavepacket–such as a phonon polariton–propagates with the group velocity v_{gr}. The group velocity is the velocity at which the energy or a signal moves through a medium. For transparent, weakly absorbing media, the dielectric function $\epsilon(\omega)$ can be assumed to be mostly real and the group velocity can be calculated from the relation [34]

$$v_{gr}(\omega) = \left[\mathrm{Re} \left(\frac{\partial q}{\partial \omega_{pp}} \right) \right]^{-1} . \tag{2.5}$$

This equation has an analytic solution that is not explicitly given here due to its complexity. The red line in figure 2.6 shows the numerically calculated polariton group velocity in $LiNbO_3$ as a function of frequency. In the linear regime of the dispersion relation, i.e. for small values of ω_{pp}, phonon polaritons propagate with $\sim 0.2 \cdot c_0$. In this frequency region the imaginary part of the polariton wavevector is negligibly small compared to the real part of the polariton wavevector. Equation 2.5 can be well applied to describe the propagation of a polariton wavepacket. The group velocity decreases to zero, as the frequency of phonon polaritons approaches the frequency of the TO phonon resonance at $\nu_{TO} = 7.56$ THz. For absorbing media the group velocity is not exactly equal to the speed at which the energy is transported [35, 36] and thus, this equation is not valid anymore in the region where the damping of phonon polariton increases. This is especially the case for frequencies that are close to the resonance frequency of the TO phonons. As can be seen in figure 2.6 the group velocity v_{gr}–drown as red line– starts to increase near $\nu_{TO} = 7.56$ THz, reaches the value of plus infinity, jumps to minus infinity, and finally approaches zero frequency. As discussed by Loudon [36], the group velocity defined by equation 2.5 violates the principles of causality and the concept of group velocity breaks down for the case of an absorbing medium. Starting with a classical model of a damped harmonic oscillator, Loudon derives an expression for the velocity at which the energy is transported through an absorbing
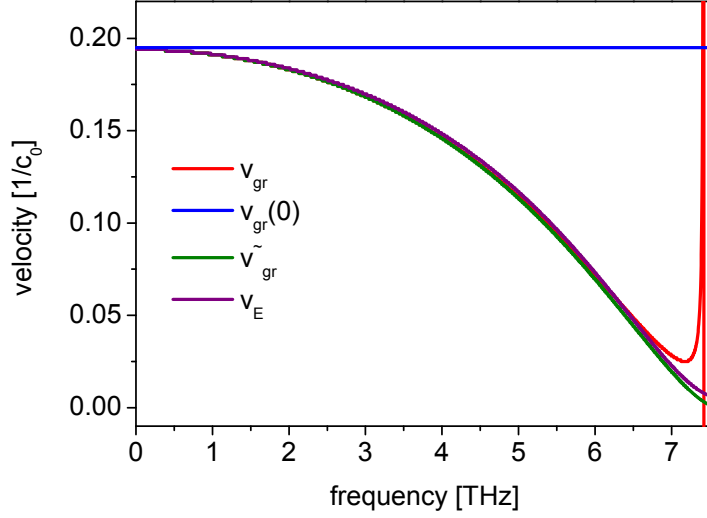
Figure 2.6: Calculated group velocity v_{gr} (red line) of phonon polariton wavepackets in LiNbO$_3$ for frequencies lower than the first TO mode, $\omega < 7.56$ THz. The velocity is given as fraction of the velocity of light in vacuum, c_0. All calculations use parameters that are obtained by the Raman scattering experiment and are listed in the third column of table 2.1. The velocity of low-frequency phonon polaritons, $v_{gr}(\omega_{pp} = 0) = 0.195 \cdot c_0$ is shown as blue line. The calculated group velocity $\tilde{v}_{gr}$ and energy velocity v_E are indicated by the green and violet lines, respectively.

dielectric material [36]. Moreover, he makes the assumption that the whole energy, namely the energy stored in the electromagnetic wave and the energy stored in the excited harmonic oscillator, has to be taken into account. The derived energy velocity,

$$v_E(\omega) = \frac{1}{\text{Re}(\sqrt{\epsilon(\omega)}) + 2 \cdot \text{Im}(\sqrt{\epsilon(\omega)})/\Gamma} \quad , \tag{2.6}$$

remains always positive and smaller than the speed of light in free space. The calculated energy velocity for the case of LiNbO$_3$ is shown as the violet line in figure 2.6. For small frequencies v_E is equal to v_{gr}. For frequencies close to the frequency of the phonon resonance the curve continues to approach zero frequency. Furthermore, the green line in figure 2.6 shows a calculation of the group velocity of phonon polaritons. In this case, the damping constant is assumed to be $\Gamma_1 = 19.9/10$ cm^{-1}, which is ten times smaller than the value, which is used in the calculation of the function shown by the red line. This curve coincides with the previously calculated group velocity v_{gr} and the energy velocity v_E for small frequencies and the curve approaches zero frequency even faster than the energy velocity for frequencies in the vicinity of the phonon resonance. In this work, the high group velocity of phonon polaritons has to

explicitly be considered in the analysis of the obtained frequency-dependent damping rate of phonon polaritons. This is later discussed in section 9.2.

2.4 Impulsive Excitation of Phonon Polaritons

So far, the dispersion relation and the group velocity of the phonon polaritons in $LiNbO_3$ were discussed. In this section we discuss the coherent optical excitation of phonon polaritons with ultra-short laser pulses. The excitation of the phonon polaritons is impulsive: the pulse duration τ_γ is shorter than the period τ_{pp} of the lattice mode. Consequently, the spectral width ω of the laser pulse is larger than the spectral frequency of the polaritons, $\omega_{Laser} > \omega_{pp}$. Moreover, in this work the generation of the phonon polaritons is realized by two simultaneously incident laser pulses with wavevectors $\mathbf{k}_1$ and $\mathbf{k}_2$ that are crossed under an angle Θ in the sample. This allows us to selectively excite a certain wavevector of the phonon polariton under the constraint $q_{pp} = |\mathbf{k}_1 - \mathbf{k}_2|$. If this condition is fulfilled, all photons of the first pulse with the energy ω_1 and all photons with the energy ω_2 from the second pulse can mix and coherently excite phonon polaritons. Simultaneously, the energy conservation $|\omega_1 - \omega_2| = \omega_{pp}$ has to be fulfilled. For broad band excitation this is not a constraint as long ω_1 and ω_2 lie within the bandwidth of the laser pulse. But the use of spectrally narrow pulses in the excitation process is more restrictive for the energy $\hbar\omega_{pp}$ of the quasi-particle. Thus only one specific mode of the dispersion relation of the polaritons is excited and its dynamics can subsequently be examined, as will be later shown in section 2.5.1. In the following, the excitation process of phonon polaritons is described in detail.

2.4.1 Excitation of Phonon Polaritons by Stimulated Stokes Scattering

In order to excite phonon polariton wavepackets, the femtosecond laser pump pulse is split into two parts. One pulse is labeled $\mathbf{k}_1$ and the other $\mathbf{k}_2$. The two coherent laser pulses are crossed under a well-defined intersection angle Θ in the sample. The excitation pulses are non-divergent and simultaneously arrive at the sample. Further details of the experimental arrangement are described in chapter 3. The laser pulses overlap in an elliptical spot where they interfere and form a periodical transient intensity pattern as shown in figure 2.7. The so formed excitation profile in the transparent medium has a transient grating period

$$\lambda_{tg} = \frac{\lambda_c}{2 \cdot \sin(\Theta_{air}/2)} \ , \tag{2.7}$$

where λ_c is the central wavelength of the excitation pulses and Θ_{air} is the intersection angle in air [37]. Both pulses possess the same spectrum. Thus they can simultaneously act as stimulation or pump beams. Let us first consider $|\mathbf{k}_1| > |\mathbf{k}_2|$ (see Fig. 2.8a). A photon with wavevector $\mathbf{k}_1$ will be decomposed into a right-propagating phonon polariton $\mathbf{q}_R$ and a photon with a wavevector
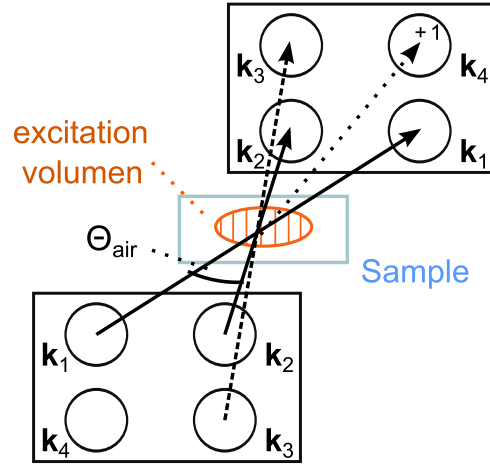
Figure 2.7: Schematic representation of the boxcar arrangement 3.3 for forward four wave mixing experi-
ments: two laser beams $\mathbf{k}_1$ and $\mathbf{k}_2$ intersect in a transparent sample S in order to create a
transient spatial modulation of the refractive index of the medium. A delayed third beam $\mathbf{k}_3$
is diffracted from the transient grating into the direction $\mathbf{k}_4$.

$\mathbf{k}_2$ with a lower energy, which is present in the spectrum of the second pulse that acts as seed
here. Simultaneously, in the case $|\mathbf{k}_1| < |\mathbf{k}_2|$ a photon with the wave vector $\mathbf{k}_2$ will in turn be
decomposed into a left-propagating phonon polariton $\mathbf{q}_L$ and a photon $\mathbf{k}_1$. Now the pulse $\mathbf{k}_1$
acts as stimulation beam and the pulse $\mathbf{k}_2$ as the pump beam. In that case, the excitation of
the left- and right-propagating phonon polariton is equally likely. The generation of the phonon
polaritons[2] is described by Stokes scattering which requires energy and momentum conservation.
The angular frequencies ω_1 and ω_2 of the first and second pulse have to satisfy the conservation
of energy

$$\omega_{pp} = |\omega_1 - \omega_2| \quad , \tag{2.8}$$

describing the creation process of a phonon polariton with angular frequency ω_{pp}. All angular
frequencies of two pump pulses which fulfill this requirement contribute to the Stokes scattering
process. The direct observation of the inelastically scattered light is not possible due to the
geometry of the experiment: both pulses act at the same time as stimulation and pump beams
during the creation of counter propagating phonon polaritons. Raman scattered light is diffracted
into the same direction and with the same energy as the corresponding spectral components of
the opposite beam.

---

[2]At room temperature the phonon polariton modes are thermally occupied according to the Boltzmann distribution.
Although a frequency of $f = 6.25$ THz corresponds to a temperature of $T = 300$ K, the annihilation of thermal
phonon polaritons is negligibly small compared to stimulated Stokes scattering. Raman scattering of ultra
short pulses by optical active vibrational modes is described in terms of impulsive stimulated Raman scattering
(ISRS) [38–40].
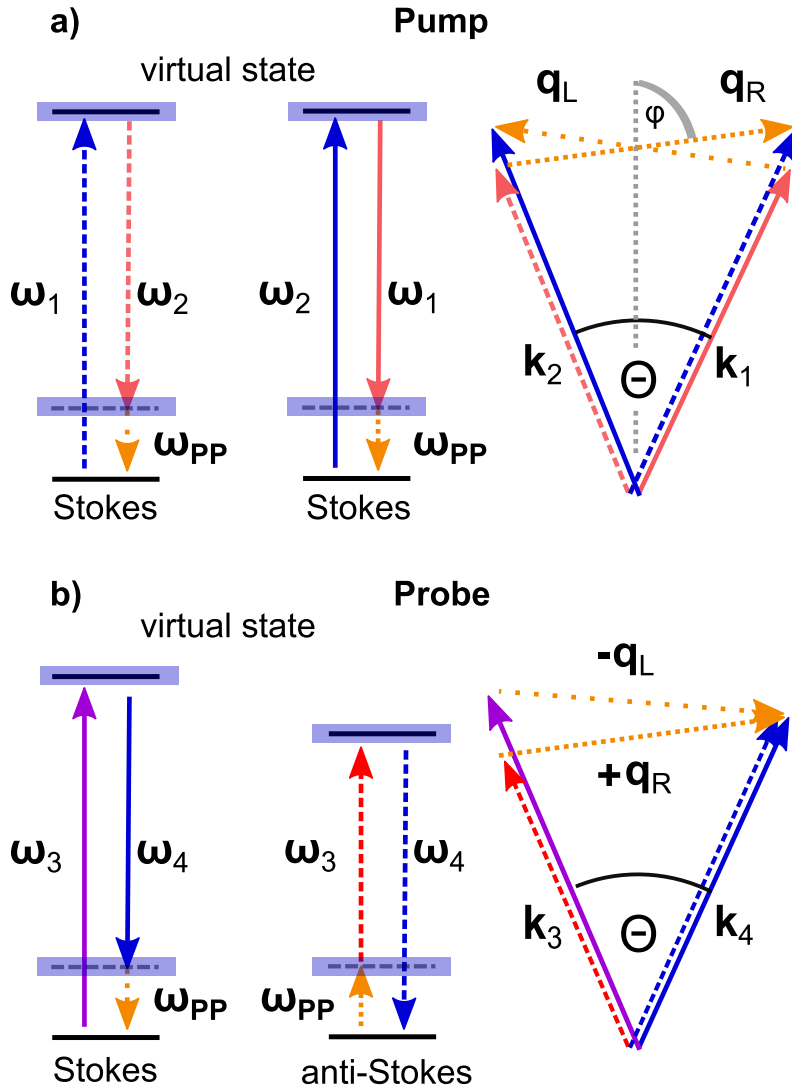
Figure 2.8: a) Energy level and momentum conservation diagrams considered in the impulsive generation of phonon polaritons. a) Two counter propagating phonon polaritons $\mathbf{q}_R$ and $\mathbf{q}_L$ are excited within the bandwidth of the laser pulses. The photons with the energy ω_1 (ω_2) are decomposed into the photons with the lower energy ω_2 (ω_1) and the right-propagating (left-propagating) phonon polaritons with the energy ω_{pp}, whereby the photons in the second pulse $\mathbf{k}_2$ ($\mathbf{k}_1$) act as the seed photons in the stimulated excitation of the phonon polaritons with the wavevector $\mathbf{q}_R$ ($\mathbf{q}_L$). b) The probe process is sensitive to the light scattered from the left and right propagating phonon polariton with the wavevector $\mathbf{q}_L$ and $\mathbf{q}_R$. The frequency of the probe light ω_3 is Stokes or anti-Stokes shifted by the amount of the frequency $\pm\omega_{pp}$ of the phonon polariton. The position of the spectrometer selects the direction $\mathbf{k}_4$ along which the light is detected and the spectrometer pixel fixes the wave vector magnitude $|\mathbf{k}_4|$ of the detected light.

Note, the same rules of energy and wavevector conservation applies for stimulated Stokes (or Raman gain) measurements [41,42], where the scattered intensity is detectable as the amplification of the seed beam. The main difference between ISRS and stimulated Stokes amplification is the bandwidth of the laser pulses and the induced inelastic Raman shifts of the light. In the ISRS the bandwidth is larger and in stimulated Stokes amplification the bandwidth is smaller than the frequency shift. The magnitude of the phonon polariton wave vector q can be calculated using the law of cosine in the wave vector diagram in figure 2.9:

$$q = \frac{n_e}{c_0}\sqrt{\omega_1^2 + \omega_2^2 - 2\omega_1\omega_2\cos(\Theta)} \ , \tag{2.9}$$

where n_e is the extraordinary refractive index for 800 nm light, ω_1 and ω_2 the angular frequency of the beam $\mathbf{k}_1$ and $\mathbf{k}_2$, respectively, c_0 the speed of light in vacuum, and Θ the intersection angle of the laser pulses in the medium. This equation is well-known in conventional Raman scattering [1] and holds as well for femtosecond laser pulses [43,44].

2.4.2 The Relation of the Wavevector of the Transient Grating and the Phonon Polariton

The relation of the wavevector $\mathbf{k_{tg}}$ of the transient grating [37] and the phonon polariton wavevector $\mathbf{q}$ is demonstrated here. $\mathbf{k_{tg}}$ holds for the elastic interaction where no energy is transferred into the system and consequently no quasi-particle is generated. In the present work a phonon polariton is excited by in an inelastic Stokes process, where the energy is conserved for three interacting particles, namely: incident photon, Stokes scattered photon and created phonon polariton. In figure 2.9a the momentum conservation, which applies in the excitation process of a phonon polariton, is illustrated for the case $|\mathbf{k}_1| > |\mathbf{k}_2|$. The spectrum of both pulses is identical and the central wavevector is $\mathbf{k}_c$. In this case the wavevector magnitude of the transient grating k_{tg} is calculated taking the intersection angle Θ of the crossed pump beams, which is fixed:

$$k_{tg} = 2k_c\sin(\Theta/2) \tag{2.10}$$

This equation just rewrites formula 2.7 in terms of the central wavevector of the incident laser pulse. The wavevector k_{tg} is parallel to the x-axis which is shown in figure 2.9c. The momentum and energy conservation for three interacting particles holds:

$$\vec{q} = \vec{k}_1 - \vec{k}_2 \ , \tag{2.11}$$

$$\omega_{pp} = \omega_1 - \omega_2 = c_l(k_1 - k_2) \ , \tag{2.12}$$

where ω_{pp} is the frequency of phonon polariton, ω_1 is the frequency of the incident laser light and ω_2 is the frequency of the Stokes scattered light. The right hand side of the equation 2.12
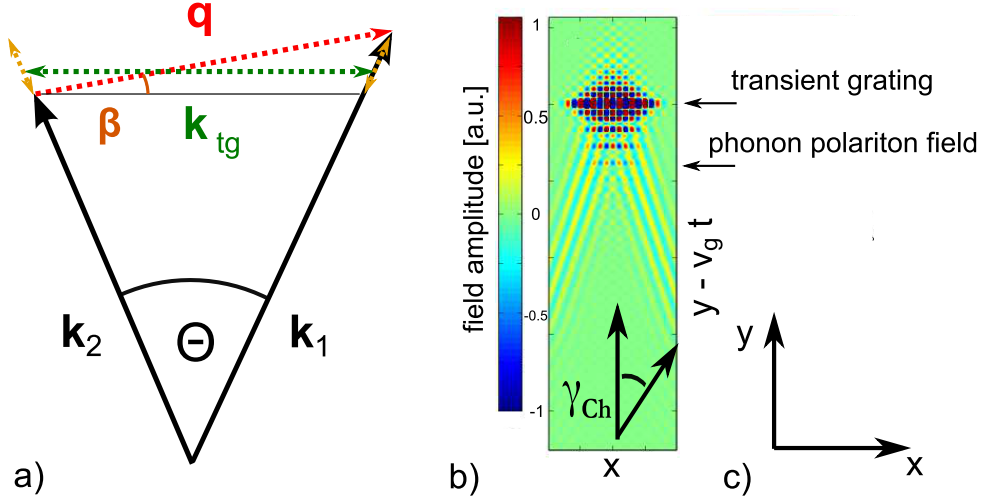
Figure 2.9: a) Wavevector diagram for the momentum conservation in stimulated Stokes scattering by a phonon polariton. b) Calculated electric field of a phonon polariton generated by a transient grating assuming Cherenkov-like emission (copied from [45]). c) Coordinate system of the propagation plane of phonon polaritons.

simply restates ω_{pp} in terms of the wavevectors k_1 and k_2, where c_l is the speed of light in the sample. The wavevector components of the polariton wavevector $\vec{q}$ can be rewritten as follows:

$$\vec{q}_x = k_1 \cdot \sin(\Theta/2) + k_2 \cdot \sin(\Theta/2) = (k_1 + k_2) \sin(\Theta/2) \tag{2.13}$$

$$q_y = k_1 \cdot \cos(\Theta/2) - k_2 \cdot \cos(\Theta/2) = (k_1 - k_2) \cos(\Theta/2) \tag{2.14}$$

Now, for convenience we define $k_1 = k_c + q/2$ and $k_2 = k_c - q/2$ and rewrite the equation 2.13:

$$q_x = (k_c + q/2 + k_c - q/2) \sin(\Theta/2) = 2k_c \sin(\Theta/2) \quad , \tag{2.15}$$

$$q_x = k_{tg} \quad . \tag{2.16}$$

The x-component of the excited polariton is equal to the wavevector of the transient grating k_{tg}, which is the excitation grating of phonon polaritons. The magnitude of the polariton wavevector q is included as $q^2 = q_x^2 + q_y^2$. In combination with equations 2.12 and 2.14 it can be expressed in the following way:

$$q^2 = k_{tg}^2 + \left(\frac{\omega_{pp}}{c_l}\right)^2 \cos^2(\Theta/2) \quad . \tag{2.17}$$

This equation relates the magnitude of the excited phonon polariton wavevector q to the frequency ω_{pp} with respect to the intersection angle Θ of the excitation laser beams. The first term (k_{tg}^2) is

easily calculated or even directly measured, for example with a CCD-camera. It is often set equal to the polariton wavevector $q = k_{tg}$ whereby q_y is commonly neglected because it is assumed that $q_x \gg q_y$. The second term in equation 2.17 can be seen as a small correction to ensure the energy conservation rules. For a good approximation we can set $\cos(\Theta/2) \approx 1$ because the angles in forward Raman scattering do not exceed 0.17 Rad $\approx 10°$. The reason for this is that the magnitude of the wavevector of the incoming light k is much larger than the magnitude of the polariton wavevector q. Assuming the dispersion relation of light $k = \omega/c_l$ and of phonon polariton $q = \omega_{pp}/c_{THz}$, equation 2.17 can be rewritten as follows:

$$\left(\frac{\omega_{pp}}{c_{THz}}\right)^2 = k_{tg}^2 + \left(\frac{\omega_{pp}}{c_l}\right)^2 \tag{2.18}$$

$$\implies \omega_{pp}^2 = k_{tg}^2 c_0^2 (n_{THz}^2 - n_l^2)^{-1} \ , \tag{2.19}$$

n_{THz} and n_l denote the refractive index of the medium in the terahertz and visible range, respectively. The deviation from the often applied approximation $q = k_{tg}$ [44, 46] is denoted by the difference of the squared refractive indexes: for $n_{THz}^2 \gg n_l^2$ the above assumption holds and the expression simplifies to

$$\omega_{pp}^2 = k_{tg}^2 c_0^2 / n_{THz}^2 \ . \tag{2.20}$$

In the following, the approximation $q = k_{tg}$ is discussed in the context of the ISRS measurement of the phonon polaritons in LiNbO$_3$. The experimental measured quantities are: the selected intersection angle Θ, the central wavelength of the laser pulse λ_c, and the frequency ω_{pp} of the phonon polariton. The dispersion relation of phonon polaritons is obtained, if the measured frequency ω_{pp} is plotted versus the polariton wavevector q calculated using equation 2.17. This is shown in figure 2.10 by the red line.

The case where the polariton frequency ω_{pp} is plotted versus the calculated wavevector of the transient grating using equation 2.10 is shown in figure 2.10 by the gray line. The so deduced dispersion relation displays larger polariton frequencies for the same magnitude of the wavevector. The error of the approximation $q = k_{tg}$ can reach ~ 0.2 THz for determined polariton frequencies in the lower polariton branch in LiNbO$_3$. Even larger deviations are expected for the higher polariton branch, where $\nu > 10$ THz, as depicted in figure 2.10. One further aspect which influences the deviation between k_{tg} and q is the wavelength of the excitation laser, because in equation 2.19 the index of refraction n_l is a function of the wavelength of the light. For example, the extraordinary index of refraction for 400 nm in lithium niobate amounts to 2.33. This is approximately 10% higher than for the 800 nm light $n_{800} = 2.16$, which has been used in the calculation shown in figure 2.10.
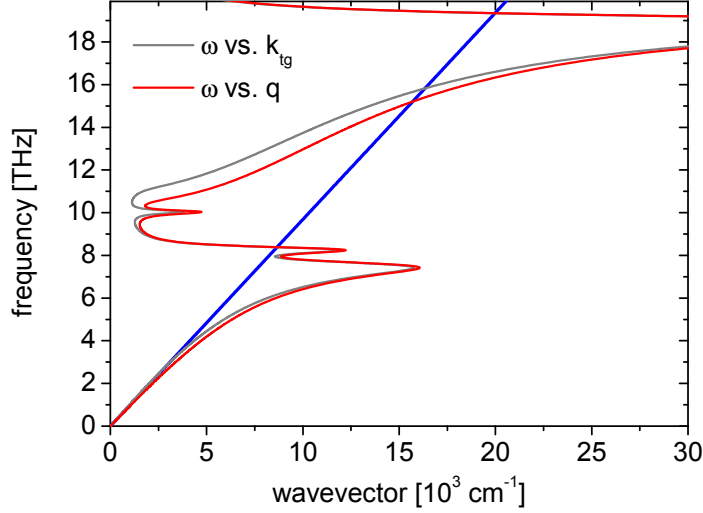
Figure 2.10: Dispersion relation of phonon polariton in LiNbO$_3$ as obtained if the measured frequency ω_{pp} is plotted versus the wavevector of phonon polariton using equation 2.17 (red line), or versus the wavevector k_{tg} of the transient grating using equation 2.10 (gray line). Blue line shows the branch of terahertz light.

2.4.3 Propagation Direction of Phonon Polaritons

With respect to k_{tg} the internal angle β of the polariton propagation direction can be calculated using a simple trigonometric relation:

$$\cos\beta = \frac{k_{tg}}{q} = \frac{\sqrt{n_{THz}^2 - n_l^2}}{n_{THz}} \quad . \tag{2.21}$$

The right hand side of the expression is derived with the help of equations 2.20 and 2.4. In figure 2.11 the frequency dependence of the internal angle $\beta(\omega)$ of the generated phonon polariton by the transient excitation grating is depicted. For $\omega_{pp} = 0$ the propagation angle is $\beta = 26$ degree. At the same time the intersection angle Θ of the two exciting laser beams is about zero degree. For larger frequencies of phonon polaritons, when Θ gets larger, the internal angel β decreases. Because of the finite sample thickness and the non-neglectable angle β the polariton wave undergoes a total internal reflection from the back and front face of the sample. It is effectively guided parallel to the surface of the crystal. The angle β of the polariton propagation will decrease even stronger for larger magnitudes of the wave vector q, if much lower damping rates for TO phonon modes are considered in the calculation (dark red solid line in figure 2.11). The phonon polariton is almost oriented parallel to the surface of the sample. A similar situation is observed for the higher dispersion branch (ω>10 THz).
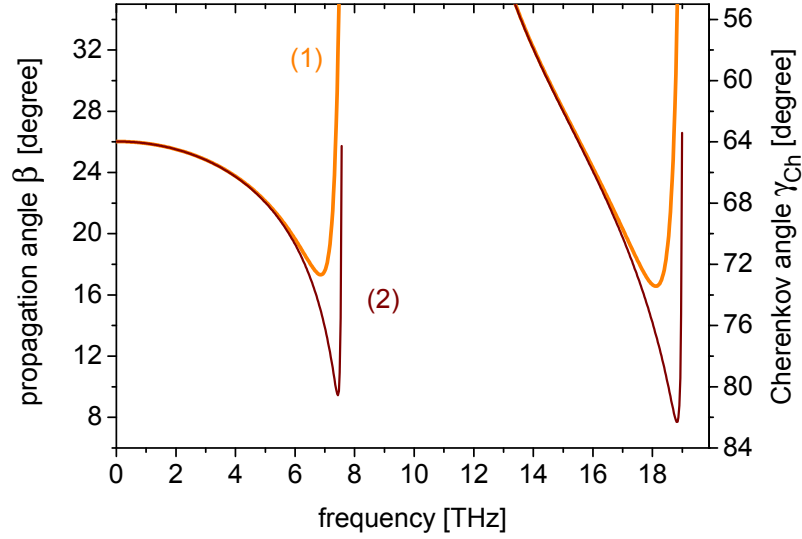
Figure 2.11: Calculated internal angle of the phonon polariton propagation β in LiNbO$_3$ versus the frequency ω_{pp}. (1) Equations 2.21 and 2.3 with the parameters from reference [27] are used in the calculation. (2) The same as in (1) but with assumption of ten times lower damping rates for the optical phonon modes. The right y-axis indicates the Cherenkov angle $\gamma_{Ch} = 90 - \beta$. Note, the critical angle in LiNbO$_3$ for the terahertz field is always smaller than γ_{Ch} and reaches 11.7°. Thus, excited phonon polaritons are internally reflected from the sample surface sites.

2.4.4 Cherenkov-like Radiation Emission from a Transient Grating Source

In the previous section 2.4.2 the relation between the wavevectors of the transient optical grating and the generated phonon polaritons was discussed. The underlying physical process of the transient grating and the generated phonon polaritons is based on the fact that the transient grating acts as a source for the emitted radiation, namely the polariton waves. In this section the Cherenkov-like emission is applied to describe the excitation process of phonon polaritons. The concept of the Cherenkov-like emission applies if a relativistic source – such as a dipole– travels faster than the emitted radiation. In polar media, such as ferroelectric materials like LiNbO$_3$ the laser induced transient grating moves with relativistic speeds faster than the emitted radiation [45, 47], which in this case are the phonon polaritons. In the visible range the velocity of the transient grating is given by $v_{tg} = c_l / \cos(\Theta/2)$. This can be inferred from the propagation of the phase fronts of both pump pulses which travel under an angle of $\Theta/2$ with respect to their bisector. v_{tg} is equal to the velocity at which the crossing point of the two phase fronts

propagates. The illustration is shown in figure 2.9b. To derive the expression for the Cherenkov angle γ_{Ch} we start with equation 2.17, which we divide by q^2 :

$$1 = \left(\frac{k_{tg}}{q}\right)^2 + \left(\frac{\omega_{pp}}{q\ c_l}\right)^2 \cos^2(\Theta/2). \tag{2.22}$$

Now one can rewrite the equation using of v_{tg}, v_{pp} and $\cos\beta$:

$$1 = \cos^2\beta + \left(\frac{v_{pp}}{v_{tg}}\right)^2 \quad , \tag{2.23}$$

$$\sin^2\beta = \left(\frac{v_{pp}}{v_{tg}}\right)^2 \quad . \tag{2.24}$$

With the identity $\sin\beta = \cos\gamma_{Ch}$ as shown in figure 2.9b, equation 2.24 can be rewritten in order to obtain the final expression for the Cherenkov angle with respect to the bisector of the excitation laser pulses:

$$\cos\gamma_{Ch} = \frac{v_{pp}}{v_{tg}} \tag{2.25}$$

The Cherenkov angle γ_{Ch} relates the velocity v_{tg} of the transient grating to the polariton velocity v_{pp}. The right y-axis in figure 2.11 shows the Cherenkov angle $\gamma_{Ch} = 90 - \beta$ versus the polariton frequency ω_{pp}. In LiNbO$_3$ the critical angle for the terahertz field is always smaller than $\gamma_{Ch} \leq 11.7°$. Thus, the excited phonon polaritons are always internally reflected from the sample surfaces. Moreover, the electromagnetic part of the excited phonon polariton can be coupled out from the medium into the free space, if the backside of the sample is cut under a angle which is perpendicular to the propagation direction of the quasi particle [48, 49].

2.4.5 Non-linear Optical Excitation of Phonon Polaritons

Up to now, the excitation of phonon polaritons was described in terms of Raman scattering, where the light field couples via the electronic system directly [4] to the vibrational degree of freedom of the polariton mode. Because a phonon polariton is a coupled mode that consists of an electromagnetic wave $E(\Omega)$ and polar lattice vibration with an amplitude $Q(\Omega)$, an additional coupling mechanism of the light field to the electric field $E(\Omega)$ of the polariton, which is known as difference frequency generation (DFG), is assumed in the following. In this section the capital Greek letter Ω is used instead of ω for a better distinction from the frequencies of visible light.

The both incoming light fields of the excitation laser E(ω_1) and E(ω_1) mix and create a non-linear polarization

$$P^{NL}(\Omega = |\omega_1 - \omega_2|) = \chi_{eff}^{(2)} E(\omega_1) E(\omega_2), \tag{2.26}$$

where $\chi_{eff}^{(2)}$ includes Raman and DFG components, respectively. This polarization creates the electric field associated with a phonon polariton. The second-order tensor $\chi_{eff}^{(2)}$ is the sum of the DFG part χ^2 and the Raman part χ^R. Both of these susceptibilities are electronic in nature. It will exhibit strong dispersion as a function of the frequency Ω. In this work, the excited phonon polaritons are observed using a third laser pulse. Thus, the non-linear optical probe process and the intrinsic structure of the effective susceptibility is discussed in detail in section 2.5.3.

2.5 Time Resolved Observation of Phonon Polaritons

The time-resolved observation of coherent non-equilibrium phonon polariton dynamics inside the medium is achieved by delaying a third laser pulse $\mathbf{k}_3$ with respect to the two pump beams $\mathbf{k}_1$ and $\mathbf{k}_2$, respectively. The time-delayed probe pulse is taken from the same laser and is focused into the sample in order to scatter from the excited polariton wavepackets. Two pump and one probe pulses are incident in the so-called box-car geometry as shown in figure 2.7 (a more detailed description is presented in chapter 3).

2.5.1 Probe of Phonon Polaritons by Stimulated Raman Scattering

In the probe process both Stokes and anti-Stokes scattering of light occur. A phonon polariton can either be annihilated or it can act as a seed wave leading to a decomposition of the incident probe laser photon $\mathbf{k}_3$ into an additional polariton with the same frequency and wavevector and a Stokes scattered phonon $\mathbf{k}_4$. In figure 2.8b this situation is schematically explained. For the Stokes scattering process the incoming photon with the frequency ω_3 is inelastic scattered from the left-propagating polariton $\mathbf{q}_L$ under the stimulated emission of a red shifted photon with frequency ω_4 and an additional polariton with wave vector $\mathbf{q}_L$. Anti-Stokes scattering in this geometry leads to the annihilation of a right-propagating phonon polariton $\mathbf{q}_R$ under the emission of a blue-shifted photon with ω_4. As long as phonon polaritons are inside of the probe volume the scattered light is detectable and is recorded as a function of time-delay and gives the information about the frequency ω_{pp} and the damping γ of phonon polariton. In principle all photons ω_3 present in the probe pulse can Stokes (anti-Stokes) scatter from a left- (right-) propagating phonon polariton and thus contribute to the signal. Most of the times, the energy shifts are much smaller, than the spectral widths of the femtosecond pulses. To resolve these shifts directly narrow bandwidth probe pulses are experimentally implemented in the present work as will be discussed in the following section.

2.5.2 Probe Process with Narrow Band Pulses

Stokes and anti-Stokes frequency shifts cannot directly be detected with temporally short and spectrally broad probe pulses. In the ISRS experiments the frequency shifts induced by Raman scattering are generally smaller than the bandwidths of the incident laser pulses. In this work the bandwidth of the laser pulses is $\Delta\omega_{\frac{1}{e}} = 18$ THz, which is larger than the frequency $\omega_{T,1} = 7.5$ THz of the lowest TO phonon in $LiNbO_3$. Moreover, the Stokes and anti-Stokes diffracted photons are superimposed, which results in a small and almost unresolvable broadening of the detected spectrum. Therefore, a bandpass filter is implemented in the present work in order to narrow the spectrum of the probe beam to $\Delta\lambda = 2$ nm, which in turn should enable to resolve spectral shifts induced by inelastic scattering from phonon polaritons. Figure 2.12 shows the energy and momentum diagrams that apply for this situation. The incoming and scattered light frequencies ω_3 and ω_4 are directly measured. This allows to calculate the angular frequency ω_{pp} and the magnitude of the polariton wave vector q according to

$$\omega_{pp} = |\omega_4 - \omega_3| \tag{2.27}$$
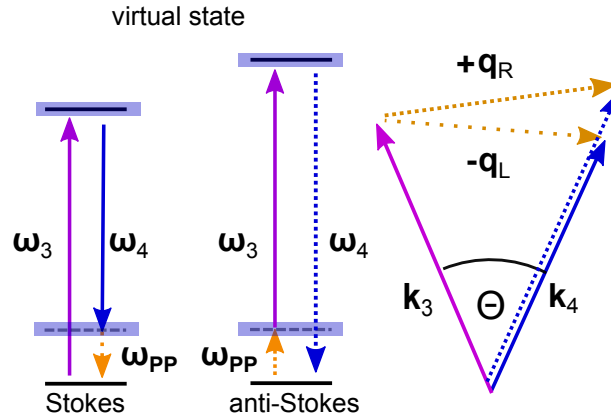
Figure 2.12: Energy level and momentum conservation diagrams considered in the narrow band detection of phonon polariton wavepackets. The incoming probe light with the energy ω_3 is Stokes shifted be the amount $-\omega_{pp}$ or anti-Stokes shifted by the amount $+\omega_{pp}$. It is diffracted into the direction $\mathbf{k}_4$, where the detector is placed.

and

$$q = \frac{n_e}{c_0}\sqrt{\omega_3^2 + \omega_4^2 - 2\omega_3\omega_4\cos(\Theta)} \quad, \tag{2.28}$$

where n_e is the extraordinary refractive index for 800 nm light, c_0 is the speed of light in vacuum, and Θ is the angle between $\mathbf{k}_3$ and $\mathbf{k}_4$ in the medium [1, 43, 44]. In our case this is the same angle as the intersection angle of both pump pulses. As shown in figure 2.12, the frequencies

of the phonon polaritons, which are observed through anti-Stokes and Stokes scattering, are not exactly equal. The arrow of the right-propagating phonon polaritons q_R that causes the anti-Stokes scattering of the incoming probe light is somewhat larger than the arrow of the left-propagating phonon polariton q_L. In the present work, the frequencies of q_R and q_L lie within 3.75% of the central frequency of the excited spectrum of the phonon polaritons. This spectral width is determined by the bandwidth of the used excitation pulses. The generated phonon polaritons have the same relative bandwidth as the used short laser pulses, as can be inferred from equation 2.9. The subsequently impinging narrow bandwidth probe pulses will scatter
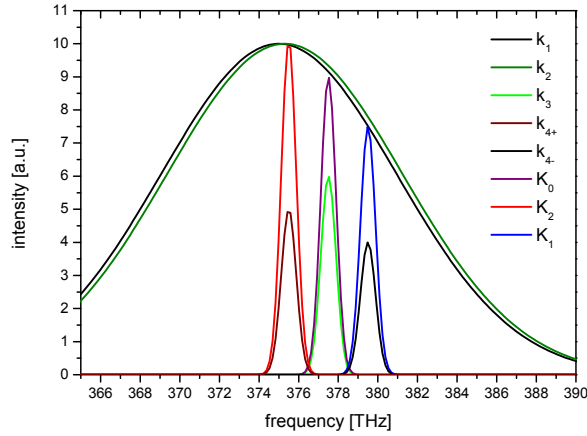
Figure 2.13: Spectra of the broad pump pulses, k_1 and k_2, and the narrow band probe pulse k_3, respectively. The spectra of probe light that undergoes anti-Stokes (k_{4+}) and Stokes scattering (k_{4-}). Spectral components of the broad pump pulses, K_0, K_1, K_2, which will contribute to the generation of such phonon polariton modes, that are subsequently exclusively probed by the narrow bandwidth pulses with the wavevector magnitude k_3.

from a subset of these polariton modes, depending on the central frequencies and bandwidths of the probe pulses. As long as the central frequencies of the probe and pump pulses are not equal, the probed subset of the right- and left-propagating phonon polaritons are not the same. Furthermore, the occupation numbers of these subsets of the phonon polariton spectra are different. Thus, the intensity of probe light that undergoes Stokes and anti-Stokes scattering will be different, too. This is true for the experiments that are described in present work. In the following, the reasons for the different occupation numbers of the right- and left-propagating phonon polaritons is explained.

In figure 2.13 the spectra of spectrally broad pump pulses, k_1 and k_2, and of the narrow bandwidth probe pulses, k_3, are shown. Note, the energy axis is given in frequency and the width of the calculated Gaussian spectra corresponds to the bandwidths of the used laser pulses. Let us now assume the central frequency of the generated phonon polaritonsa and of the probe

light to be 2 THz and 377.5 THz, respectively. During the probe process, the incoming light k_3 undergoes Stokes or anti-Stokes scattering from left- or right-propagating phonon polaritons and are shifted in frequency by -2 THz or +2 THz, respectively. The spectra of the scattered light, k_{4-} and k_{4+}, are shown in figure 2.13. Further, the question remains, which components of the incident pump spectra are involved during the excitation of these phonon polaritons that are subsequently probed by k_3. The spectral components are exactly the same as the spectra of the detected light k_{4-} and k_{4+}. In figure 2.13 these components of the pump pulses, labeled K_0, K_1, K_2, are shown. During the excitation process an incident photon K_2 decomposes into a photon K_0 with the propagation direction k_1 and a right-propagating phonon polariton q_R. Simultaneously, a photon K_0 in the second pump pulse k_2 decomposes into a photon K_1 and a left-propagating phonon polariton q_L. Exactly these created phonon polaritons, q_R and q_L, are probed, as shown in figure 2.12.

The intensities of the Stokes and anti-Stokes lines depend on the occupation numbers of the contributing phonon polaritons, which on their part are proportional to the product of the spectral components $K_0 \cdot K_1$ and $K_0 \cdot K_2$, respectively, which contribute to the creation of these phonon polaritons. Because the product $K_0 \cdot K_2$ is larger than $K_0 \cdot K_1$, the number of excited right-propagating phonon polaritons is higher than the number of left-propagating phonon polaritons, which are subsequently probed by k_3. Thus, for the discussed case here, we expect the detected anti-Stokes line to be more intense.

The experimental verification is presented in section 8.1, where the dispersion relation of phonon polaritons in $LiNbO_3$ is measured with narrow bandwidth pulses. All transient spectra, which were recorded for different intersection angles Θ, exhibit a stronger anti-Stokes than Stokes intensity peaks. Moreover, for the case where the central wavelength of the probe and pump pulses are not equal, the probe process breaks the symmetry of the excitation process in the four-wave mixing experiment and different subsets of the polariton spectra are probed.

2.5.3 Phonon Polariton Detection by a Non-linear Optical Process

Just as the excitation process of polariton wavepackets, the probe process can also be understood as a non-linear optical mixing process. The non-linear interaction of visible light with a phonon polariton mode involves both: the coupling to the electric field via DFG and the coupling to the lattice via virtual electronic Raman transitions. In non-linear optics, a higher-order of the electric susceptibility tensor is used to describe such an interaction of the light field in a medium. Lithium niobate is a typical example for such non-linear crystals. The second-order tensor $\chi_{eff}^{(2)}$ is composed of two parts: the Raman tensor $\mathrm{d}\chi/\mathrm{d}Q = \chi^R$ that describes the coupling of visible light to the phonon mode with amplitude Q, and the second-order non-linear susceptibility

$d\chi/dE = \chi^{(2)}$ that couples visible light to the terahertz field. Both of these susceptibilities are electronic in nature. The total non-linear polarization

$$P^{NL}(\omega_4) = \chi^{(2)}E(\Omega)E(\omega_3) + \chi^R Q(\Omega)E(\omega_3) \tag{2.29}$$

accounts for both contributions. ω_3 denotes the frequency of the probe light. The frequency ω_4 satisfies the energy conservation $\omega_4 = \omega_3 \pm \Omega$. Moreover, the equation of motion

$$\mu(\Omega_{TO}^2 - \Omega^2 - i\Omega\Gamma)Q(\Omega) = e^* E(\Omega) \tag{2.30}$$

describes the relation between the electric field $E(\Omega)$ and the vibrational amplitude $Q(\Omega)$, which describes the motion of a charged oscillator. Here, μ is the reduced mass of the lattice mode, e^* the effective charge of the ionic dipole, and Ω_{TO} the resonance frequency of the TO-mode [50]. Now, by substituting equation 2.30 into 2.32, the displacement coordinate $Q(\Omega)$ can be eliminated and the Raman contribution can be included in the effective non-linear susceptibility d_{eff}, which has the form

$$d_{eff}(\Omega) = \chi^{(2)}\left[1 + C\left(1 - \frac{\Omega^2}{\Omega_{TO}^2} - \frac{i\Omega\Gamma}{\Omega_{TO}^2}\right)^{-1}\right] \quad . \tag{2.31}$$

Here, $C = \chi^R/\chi^{(2)} \cdot e^*\mu^{-1}(\Omega_{TO})^{-2}$ is the Faust-Henry coefficient, which is the ratio of the Raman intensity compared to the electronic contribution. C can be assumed to be constant for a given laser wavelength and medium [45]. From these considerations the probe process can be viewed as a non-linear $\chi^{(2)}$ process, where Raman and DFG apply simultaneously. It should be noted that the same energy and momentum conservation rules apply to both contributing processes.

Moreover, in conventional Raman scattering experiment, the Faust-Henry coefficient C can be in principal be measured [50] by the comparison of the intensities of the spectral lines caused by the scattering of light by the LO and TO phonons. In the case of the selective excitation in the transient grating geometry, which is used during this work, only TO modes and no LO modes are excited. Consequently, the determination of the Faust-Henry coefficient is not possible from these experiments.

Furthermore we can express $E(\Omega)$ by means of $P^{NL}(\Omega)$ assuming the relation $E(\Omega) = P^{NL}(\Omega)/\chi^{(1)}$. The expression 2.26 takes the form

$$P^{NL}(\omega_4) = d_{eff}(\Omega)\frac{\chi_{eff}^{(2)}}{\chi^{(1)}}E(\omega_1)E(\omega_2)E(\omega_3) \quad , \tag{2.32}$$

where $\chi_{eff}^{(2)}$ is taken from equation 2.26. This relation shows that the whole ISRS process, which includes the non-linear excitation, and the subsequent non-linear probe process can formally be described as a $\chi^{(3)}$ process. In this perspective, the propagation effects of the non-collinear

light fields and the polariton fields could be included by assigning a damping to the amplitudes of the fields that depends on the time-delay between pump and probe pulses. However, this formalism does not bring any new substantial insight into the field of non-linear light-matter interaction nor helps understand better the dynamics of light scattering by the vibrational modes of solids. Thus, the description of the whole ISRS process preferably divided into two subsequent second-order non-linear processes, as is done in this work.

2.5.4 Diffraction From a Modulated Refractive Index Grating

In the following a second view of the probe process will be presented. The optical four wave mixing experiment is commonly described in terms of the diffraction of a probe pulse from a transient refractive index modulation caused by the laser induced polarization change of the medium [37]. In order to adapt this concept to the interaction of the phonon polaritons with the probe light the electric field $E(\Omega, q)$ of an excited polariton shall fully describe its nature. This is true for the light-like part of the dispersion relation, where the polariton is associated with the terahertz field. The polarization of the medium shall instantaneously follow the temporal modulation of the electric field $E(\Omega, q)$. The relationship of the polarization P and the electric field is characterized by:

$$P^{LIN}(\Omega, q) = P_0 + \chi^{(1)} E(\Omega, q) \ , \tag{2.33}$$

whereby the higher-order terms, which are responsible for non-linear effects, are not important here. P_0 is the static polarization of the ferroelectric material. We see, that the polarization is modulated by the same frequency Ω and has the same period q as the electric field $E(\Omega, q)$. The electric field $E(\Omega, q)$ thus results in a modulation of the index of refraction of the sample due to the linear electro-optical effect (Pockels effect):

$$n(\Omega, q) = n_e(1 - r_{33} \cdot n_e^2 E(\Omega, q)) \ . \tag{2.34}$$

n_e denotes again the extraordinary refractive index in the absence of an applied field, and r_{33} is the relevant electro-optical tensor element (see Eq.:2.1). The incident probe field illuminates the transient refractive index grating at a certain time-delay after its generation. A portion of the field is elastically diffracted into the direction, that is determined by the Bragg condition $\Delta k = G = q$ and $\omega_{out} - \omega_{in} = 0$, whereby G denotes the reciprocal wavelength of the polariton grating and ω_{out}, ω_{in} denote the frequency of scattered and incoming light. This result seems to be in a strict contradiction to the fact, that the inelastically scattered light from phonon polaritons is expected if a Raman process is assumed. Until now, no propagation effects were considered. Indeed, the diffraction grating is not static, because the polaritons propagate at light-like speeds in the medium. Consequently, one has to treat the problem relativistically. This leads to the

Figure 2.14: Diffraction from the phonon polariton grating in the laboratory frame of reference (dashed vectors) and in the frame of reference of co-propagation with the phonon polariton at relativistic velocities (solid vectors). After [51].

optical Doppler effect, which causes a frequency shift of the diffracted light [51]. For the case of a left propagating phonon polariton, figure 2.14 shows how the incoming and inelastically scattered wavevectors have to be transformed in the frame of reference of co-propagation with the diffraction grating at relativistic speed and then elastic Bragg scattering is fulfilled in the co-propagating frame of reference. The Lorentz transformation leads to a relative frequency shift of incident and scattered probe light but the total phase of the light is invariable under the Lorentz transformation [52]. Thus, the relative phase difference of all colors present in the laser pulse are unaffected by the inelastic scattering from the phonon polaritons.

3 Experimental Setup

The progress in femtosecond pulse generation technology opens new fields in the direct observation of dynamics in molecules and solids. Time domain femtosecond spectroscopy covers a frequency range of up to several terahertz. Scientific endeavors in this field advance into the direction of control and manipulation of light-induced ultrafast processes in matter or on the sample surface [53–58]. For such purposes an extensive characterization and monitoring of ultra-short laser pulses is required.

This chapter deals with the setup for Impulsive Stimulated Raman Scattering (ISRS) that was build as part of this work. After a brief discussion of the ultrafast laser system in section 3.1 and of the main components of the pump probe setup in section 3.2, the interferometric phase-mask-based, degenerate four wave mixing apparatus is discussed in detail in section 3.3. In the following section 3.4, the spatial characterization of the excitation and probe profiles is described and the uncertainty of the selectively exited polariton wave vectors is deduced. Afterwards, the optical spectrometer is introduced and the measurement of the pulse duration via the transient grating frequency resolved optical gating (TG-FROG) is discussed. Finally, the temporal resolution of the experiment is discussed.

3.1 The Ti:Sapphire Laser System

A commercially available Ti:Sapphire ultrafast oscillator (Mantis, Coherent) with Kerr lens modelocking [59–62] generates femtosecond laser pulses with 80 MHz repetition rate and a center wavelength of 790 nm. The range of the spectrum measures from 760 nm to 845 nm, which corresponds to a bandwidth of 85 nm (FWHM) or to a duration of 11 fs for a transform limited pulse. The pulse energy is approximately 5.6 nJ ($\sim$ 450 mW). These pulses are then sent into the regenerative amplifier unit.

The amplifier is a two stage Ti:Sapphire amplifier laser system (Legend Elite Duo, Coherent) [63] and consists of a regenerative amplifier and a single pass booster amplifier. Both units utilize Ti:Sapphire crystals as active media and both are optically pumped with nanosecond-pulses with a central wave length of $\lambda = 527$ nm delivered from a frequency-doubled, Q-switched Nd:YLF laser (Evolution, Elite Duo, Coherent). Each unit is pumped with a power of $\sim$ 20 W. The amplification of the 800 nm seed pulse from the oscillator (< 100 fs) is performed according to
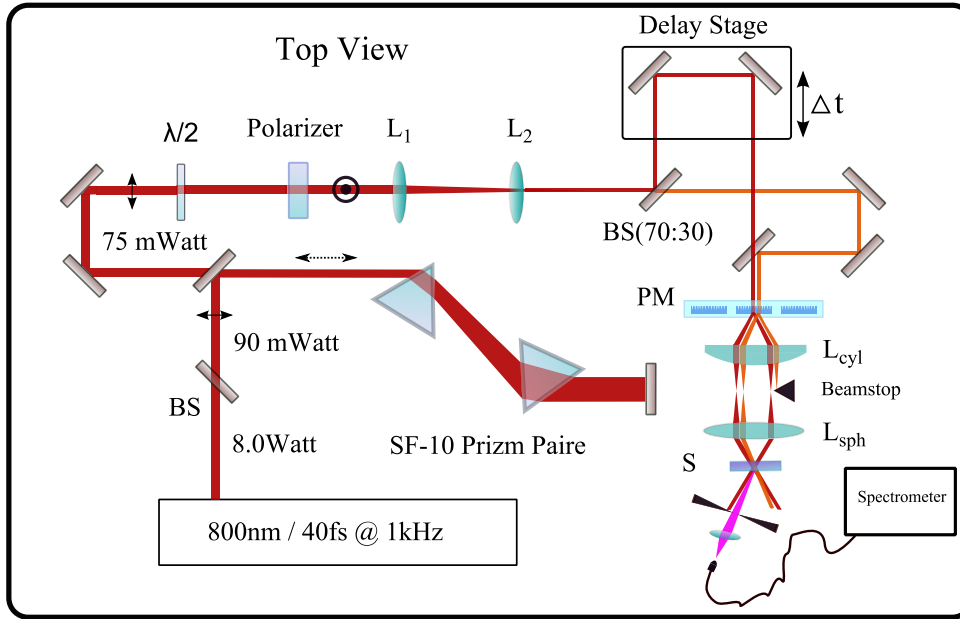
Figure 3.1: Optical setup with typical pulse parameters used in the discussed experiments. The beams are displaced at the phase mask interferometer for clarity. Used abbreviations: BS = beamsplitter, L = lens, PM = phase mask, S = sample.

the principle of chirped pulse amplification [10, 11, 64]: the seed pulses are initially temporally stretched to several picoseconds in a grating stretcher. Thereafter, they are amplified in the active media and afterwards the high power pulses are again temporally compressed in a grating compressor. The compressor adds a negative chirp [10, 11] and essentially reverses the positive chirp previously added in the stretcher. This procedure reduces the peak intensities of the short pulses in the amplifier system and thus prevents the crystals from being damaged. This allows a higher pulse power after the amplification. After the amplifier units, the pulse energy measures about 7 - 8 mJ at a repetition rate of 1 kHz. The femtosecond pulses share a central wavelength of 800 nm and a temporal widths of FWHM = 40 fs which corresponds to a bandwidth of FWHM = 32 nm for Fourier limited pulses.

3.2 Optical Setup

Figure 3.1 shows the optical setup that is used for the ultrafast pump probe spectroscopy [65] experiments. First the pulses with an average power of $\sim$ 90 mW pass a prism compressor made of two SF-10 prisms which add a linear negative chirp to account for the positive material dispersion in the whole laser path [11]. An attenuator is build using a zero-order lambda-half-wave plate and a linear polarizer. Simultaneously, the light polarization is rotated from p polarization to s polarization with respect to the plane of the following mirror. The beam is focused with

a telescope to $r \approx 0.5$ mm radius which ensures that the laser pulses can later pass through the phase mask (PM). Next, a beam splitter (BS) divides the laser beam into two parts. The typical ratio is $R/T = 70/30$. The pump pulse is guided over the delay stage. The pump and probe pulses propagate at slightly different heights. A D-shape mirror (DM) positioned after the mechanical delay is used to align such that the probe pulse propagates parallel to the pump beam. Both beams impinge on the phase mask (PM) with a vertical offset of 1.5 mm. The binary phase mask is fabricated from a transparent material by etching a grating pattern with an optimized etch depth which maximize the diffraction efficiency (up to 70%) of the first-orders for 800 nm light. Thus the phase mask generates two pump and two probe beams as can be seen in figure 3.2.

All beams are imaged by a cylindrical (L_{CYL}) and a spherical lens (L_{SPH}) into the sample creating a interference light grating in the transparent sample. A beam stop (BST) is inserted in order to block one of the probe beams as shown in figure 3.1. On the detection side a spectrometer is used instead of a photodiode [7]. The position of the spectrometer is aligned with the blocked beam which is of course unblocked for this purpose. Different bandpass filters (BP-F) can be inserted into each beam path. This allows us selectively cut out spectral components from these pulsed beams and in turn enables us to manipulate the excitation or the detection regime in the four wave mixing experiment. Moreover, a neutral density filter is inserted into both probe beams in order to control their relative intensity for an optimal heterodyne detection [7, 66] of the signals. An exemplary measurement is discussed in section 5.6.

3.3 In Detail: Phase Mask Interferometer

The very compact and stable phase mask based interferometer [66] was developed at the Massachusetts Institute of Technology (MIT) group of Prof. K. A. Nelson for laser-induced dynamic grating [37] spectroscopy. The key feature is the implementation of a transmission phase mask (PM), which is fabricated by etching a binary grating into a transparent substrate. The transmission grating is optimized to achieve high diffraction efficiency of the impinging light of 800 nm into ± 1 orders. This optical device generates two pump and two probe beams, which are subsequently imaged by two lenses into the transparent sample as shown in figure 3.2. The phase mask pattern is imposed into the sample and the transmission grating geometry determines the geometry of the excitation grating in the sample created by the recombined ultra-short laser pulses. The wave length Λ_{tg} of the transient excitation grating in the material is given by the following equation:

$$\Lambda_{tg} = \frac{\lambda}{2 \cdot sin(\Theta_{air}/2)} = \frac{\Lambda_0}{2} \cdot \frac{f_2}{f_1} \quad , \tag{3.1}$$

with the laser wavelength λ, the intersection angle of the pump beams in air Θ_{air}, and the period
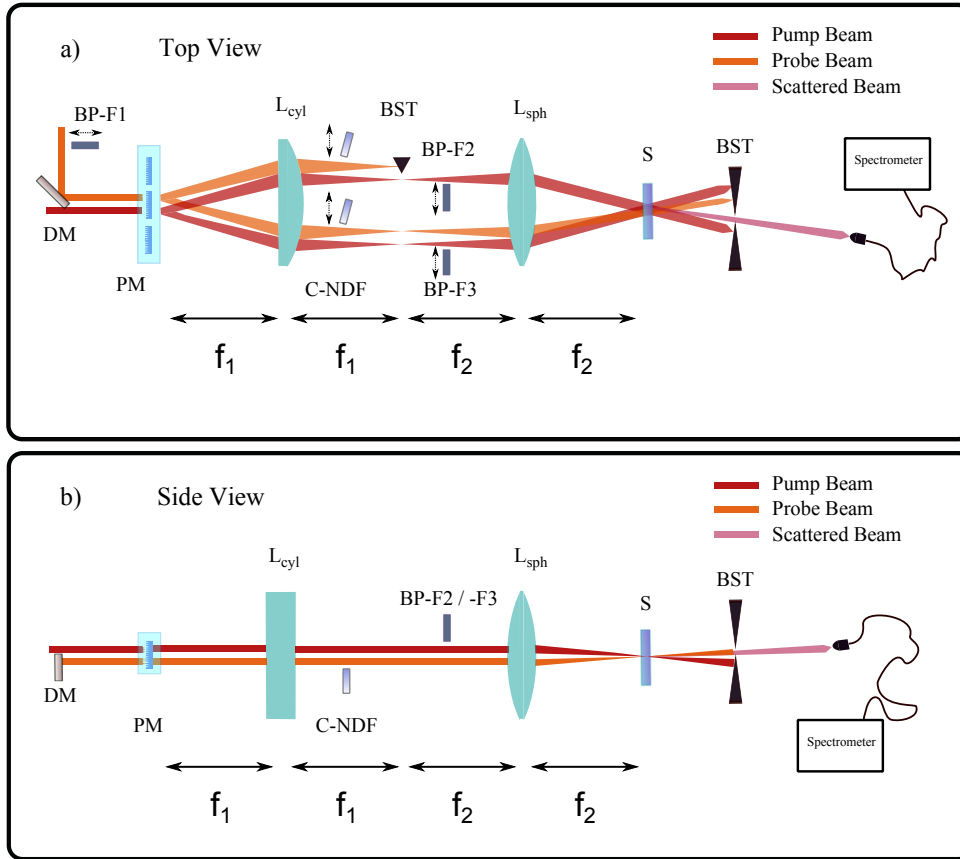
Figure 3.2: Phase mask interferometer setup. The probe beams are displaced in panel a) for clarity. Used abbreviations: BP-F = bandpass filter, BS = beam splitter, BST = beam stop, C-NDF = continuously variable neutral density filter, DM = D-shape mirror, L = lens, PM = phase mask, S = sample. The central wavelength λ_{cen} and FWHM ω of the bandpass filters are: BP-F1 : $\lambda_{cen} = 796$ nm, $\omega = 2$ nm; BP-F2 : $\lambda_{cen} = 800$ nm, $\omega = 10$ nm; BP-F3 : $\lambda_{cen} = 810$ nm, $\omega = 10$ nm. The focal lengths of the used lenses are: $f_1 = 75$ mm and $f_2 = 75 / 100$ mm.

of the phase mask Λ_0. The ratio of the focal lengths M = f_2/f_1 determines the magnification factor of the imaging setup. It is important to note that the right hand side of equation 3.1 is independent of the laser wavelength. Therefore, all colors present in a femtosecond pulse generate the same transient grating period Λ_{tg} which is solely determined by changing the period Λ_0 of the phase mask. The angular dispersion dΘ/dλ of the diffracted light by the transmission phase mask results in a small variation of the angle of incidence of an individual wavelength of the broad pulse spectrum. The deviation is estimated to be less than d$\Theta(\lambda)/\Theta = 0.019$. Consequently, all wavevectors in the laser pulse are assumed to be collinear at the focus of the interferometer. An overview of available grating spacing Λ_0 is given in table 3.1. One important property of the interferometer is its high symmetry. Since the excitation and probe beams are

nr:	1	2	3	4	5	6	7	8	9
Λ_0 [μm]	160	120	80	60	40	30	24	20	17.1
nr:	10	11	12	13	14	15	16	17	18
Λ_0 [μm]	15	13.3	11	10	9.25	8	6.7	5.25	4.3

Table 3.1: The grating spacing Λ_0 of the used phase masks.

split by the same diffraction grating, they appear in the so-called box-car geometry [67] as shown in figure 3.4. In this geometry, the probe beam with the wavelength λ_p always fulfills the Bragg diffraction condition $2 \cdot \Lambda_{tg} = \lambda_p$ in sufficiently thick samples [37]. Moreover, the temporal stability between the two probe pulses is sufficient to perform measurements using a fourth beam,- which in this case acts as a local field [7, 68]. An exemplary experiment is discussed in section 5.6. An additional advantage of the box-car geometry is the spatial separation of the scattered and transmitted light. This yields an almost background-free detection of the signals.

3.4 Characterization of the Laser Pulses

In time-resolved experiments, it is important to know the pulse duration which determines the temporal resolution of the experiment. In addition, the relative phase of the spectral components in the pulse, known also as chirp, are of great importance. Within the scope of the present work it is crucial to be aware of the different wave lengths present in the pulses because they may lead to DFG and impulsively launch a coherent phonon polariton wavepacket. In addition, it is important to know which spectral components contribute to the scattering probe process as it determines which modes are simultaneously excited. Furthermore, the profiles of the laser pulses and the shape of the transient excitation grating is of a particular importance, because this determines the initial shape of the wavepacket of the generated phonon polaritons which is related to the spectrum of the excited wavevectors, especially higher-orders components.

3.4.1 Spatial Characterization of the Excitation and Probe Pulse Profiles

In this section, the characterization measurements of the intensity grating are presented. As discussed in the previous section 3.3, the transient grating is formed by two crossed excitation laser pulses that are split and subsequently recombined in the phase mask based interferometer. The Fourier analysis of the observed intensity grating indicates that the finite size of the excitation profile leads to an uncertainty Δk_{tg} of the wavevector k_{tg} of the transient grating and according to

relation 2.17 this leads to the uncertainty Δq of the corresponding wavevector q – the wavevector of the excited phonon polariton.

The interference fringes are recorded by replacing the sample by a charge coupled device (CCD) camera and a typical picture of the interference fringes are shown in figure 3.3. The two crossed pump beams in this setup create an elliptically shaped excitation spot with the dimension of 800x50 μm FWHM. The power in both pump pulses does not exceed 15 mW at a repetition rate of 1 kHz which corresponds to a fluence of $F_{pump} \approx 12$ mJ/cm^2. The spot size of the probe pulse is usually a bit smaller and of the order of ≈ 700x30 μm which corresponds to a fluence of $F_{probe} \sim 5$ mJ/cm^2. This choice of the pump and probe fluences is determined by the two reasons:

- On the one hand, the generation process is a second-order non-linear optical process. Consequently, if saturation effects are neglected, a maximized pump fluence is preferential to generate sufficiently large field amplitudes of the phonon polaritons, which could be probed in the subsequent light scattering event. On the other hand, the upper limits are set by the undesired non-linear effects in the focusing optic such as the self-phase modulation.

- The scattered probe intensity is proportional to the intensity of the incoming probe light. Thus, the fluence of the probe light should be increased. However, one has to pay attention to not disturb the previously generated polariton wavepacket. No such effects were observed during the performed experiments.

The horizontal cuts through the beam profiles are shown in figures 3.3a and 3.3b for two selected values of Λ_{tg}, corresponding to an intersection angles $\Theta_{air} = 0.51°$ (Fig. 3.3a) and $\Theta_{air} = 1.58°$, respectively. The intensity pattern can be described by a modulation proportional to $(1 - \cos(k_{tg}x))$ multiplied with a Gaussian envelope function in order to account for the shape of the beam profiles. The Fourier transform of the profile allows to determine the spatial modulation period Λ_{tg} and the corresponding reciprocal wave vector $k_{tg} = 2\pi/\Lambda_{tg}$ of the excitation grating which is shown in figures 3.3c and 3.3d. The width of the peak after the Fourier transformation corresponds to the uncertainty Δk_{tg}. The relative uncertainty $\delta k_{tg} = \Delta k_{tg}/k_{tg}$ decreases with increasing k_{tg} due to the fact that for the same spot size the number of the interference fringes increases with increasing k_{tg}. Thus, the spectral components of the written transient grating becomes more and more sharp. In the example shown in figure 3.3, the relative width of the peak is $\delta k_{tg} = 10$ % and $\delta k_{tg} = 2.6$ %, for $k_{tg} = 696$ cm^{-1} and $k_{tg} = 2170$ cm^{-1}, respectively. The reduced strength of the intensity modulation that is visible in figure 3.3b compared to the one shown in 3.3a is caused by the finite resolution of the CCD camera. The simulation of the data that takes the convolution effects into account yields a width of the instrument function of FWHM ≈ 10 μm which is approximately twice the pixel size. The size of one pixel
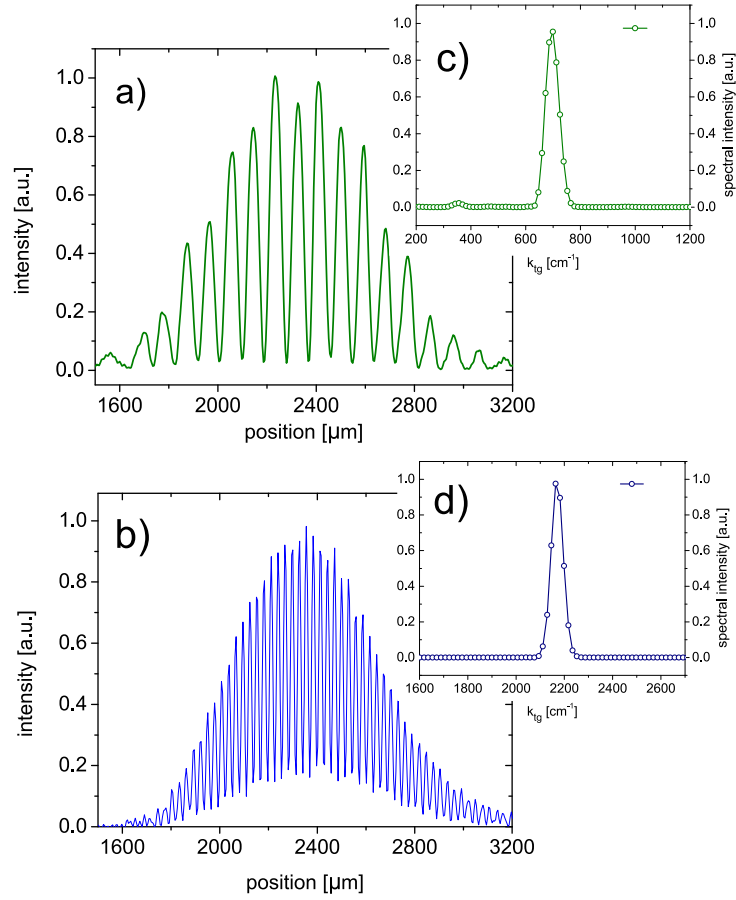
Figure 3.3: Vertical cut of the profile of the intensity profile detected with a CCD camera. The intersection angle have been adjusted to be $\Theta_{air} = 0.51°$ (a) and $\Theta_{air} = 0.51°$ (b), respectively. c) Normalized Fourier spectrum of the intensity shown in a) is centered at 696 cm^{-1}. The width of the peak is FWHM = 56 cm^{-1}. d) Normalized Fourier spectrum of the intensity shown in b) is centered at 2170 cm^{-1}. The width of the peak is FWHM = 56 cm^{-1}.

is 4.65x4.65 μm. The CCD camera was used to determine the wavevector and especially the uncertainty Δq of the excitation grating up to $k_{tg} = 2400$ cm^{-1}. For larger wave vectors it was not possible to resolve the fringe spacing anymore. A camera with a smaller pixel size should overcome this problem. Nevertheless, the use of the CCD camera allows to control and to optimize the overlap conditions of both excitation pulses as well as the relative spatial position of the probe pulse.

3.4.2 Spectrometer

For the analysis of the diffracted probe light a fiber-optic spectrometer model USB4000 from Ocean Optics with a blazed grating and a CCD-array consisting of 3648 pixels is used. Every pixel has the dimension of 8x200 μm. The integration time of the spectrometer can by set
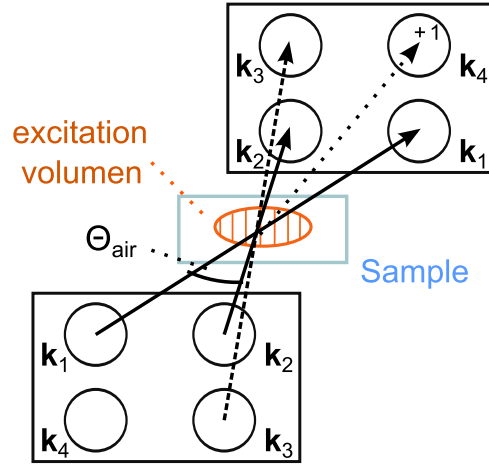
Figure 3.4: Schematic representation of the boxcar arrangement 3.3 for forward four wave mixing experiments: two laser beams $\mathbf{k}_1$ and $\mathbf{k}_2$ intersect in a transparent sample S in order to create a transient spatial modulation of the refractive index of the medium. A delayed third beam $\mathbf{k}_3$ is diffracted from the transient grating into the direction $\mathbf{k}_4$.

between 3.8 ms to 10 s and the signal-to-noise ratio is approximately 300:1. The calibrated spectral range covers the region 650 nm - 1300 nm. In a typical experiment, the region of interest at the wavelength of 800 nm is covered by a single pixel which is illuminated by light with a wavelength spread of $\pm\delta\lambda = 0.2$ nm which can be converted via the time-energy uncertainty to a time uncertainty of $\delta\tau = 4.7$ ps. During this time interval, any scattered light, such as post-pulses, interfere with the scattered light on the diode array. Therefore, it is important to check the pump and probe beams for traces of existing post-pulses, for example using TG-FROG as discussed in section 3.4.3.

3.4.3 Pulse Characterization using TG-FROG

In this thesis, the method of transient grating frequency-resolved optical gating (TG-FROG) [69] is utilized in order to measure the pulse duration and in order to determine and to control [70] its spectral chirp [10, 11]. Moreover, in the generation process of phonon polaritons DFG applies and thus it is important to know which of the spectral components of the incident pulses will simultaneously arrive in the sample and will contribute to the coherent excitation of the phonon polaritons. In the probe process it is advantageous to deliver all colors of the probe pulse simultaneously on the sample and to minimize the effect of phase difference between scattered light fields which are subsequently detected by the homodyne detection scheme, which is discussed in chapter 5.

Here, the characterization measurements of the laser pulses have been performed with the same four wave mixing setup, which has been introduced in the previous section 3.3. For these

measurements, the sample is replaced by a thin BK7 glass plate. As mentioned before (Sec.: 3.3) the two crossed pump pulses $E_1(\omega, t)$ and $E_2(\omega, t)$ form an intensity grating in the medium which leads to a modulation of its refractive index n. From this transient grating a probe pulse $E_3(\omega, t + \tau)$, with varied time-delay τ, is elastically scattered. The electric field of the diffracted pulse

$$E_{sig}^{TG}(t, \tau) \propto \chi^3 E_3(t) E_1(t - \tau) E_2^*(t - \tau) \ , \tag{3.2}$$

is detected. χ^3 is the non-linear third-order susceptibility tensor element of the active medium. This is a material specific constant which relates the three incoming plane waves E_1, E_2, and E_3 to the generated forth wave E_{sig}^{TG}. Since the pulses E_1 and E_2 are identical, these subscripts are dropped. Equation 3.2 simplifies to

$$E_{sig}^{TG}(t, \tau) \propto E_3(t) |E_g(t - \tau)|^2 \ , \tag{3.3}$$

where $|E_g(t - \tau)|^2$ is the so-called gate function. The spectrum of the diffracted pulse is recorded as a function of the delay between the third pulse and the gate pulses. The measured signal intensity $I_{FROG}(\omega, \tau)$ yields the FROG trace as function of the frequency ω and the delay τ:

$$I_{sig}^{TG}(t, \tau) \propto \left| \int_{-\infty}^{\infty} E_3(t) |E_g(t - \tau)|^2 exp(-i\omega t) \mathrm{d}t \right|^2 \ . \tag{3.4}$$

If the measured pulse exhibits a linear chirp (second-order chirp), this is unambiguously determined by the obtained FROG trace. By adjusting the amount of material dispersion added by the second prism in the optical compressor one controls the linear chirp. The pulses where negatively pre-chirped to guarantee the shortest duration at the position of the sample. Thus the generation process of phonon polaritons in non-linear crystals (e.g. $LiNbO_3$ and $LiTaO_3$) is especially impulsive and coherent. The probe pulse has no noticeable chirp either. So, all containing colors are simultaneously scattered. In figure 3.5a typical FROG-trace for a short probe pulse is shown. The spectrally integrated diffracted light versus time-delay is plotted in the figure 3.5b. If one assumes that the profile of the cross-correlated pulses exhibits a Gaussian shape, the relation of the measured width (FWHM) σ_{sig}, the gate pulse width σ_g, and the probe pulse width σ_3 are related by $\sigma_{sig}^2 = \frac{1}{2}\sigma_g^2 + \sigma_3^2$. In the case where the gate and the probe pulses are identical, this relation simplifies to $\sigma_{sig}^2 = \frac{\sigma_g^2}{1.5}$. If the width of the gate pulse is known, the width of the third pulse can be deduced from the cross-correlation data.

In this work three different bandpass filters are used to cut out the specific wave lengths of the incident short and thus spectrally broad pulses. These spectrally filtered pulses are also measured using TG-FROG. In figure 3.5b and c, other FROG-traces are presented. The corresponding spectral integrated intensity versus delay-time (e,f) and the measured spectrum of the pulse (h,i) are shown. The data shown in the second line are obtained for a 10 nm broad, spectrally filtered
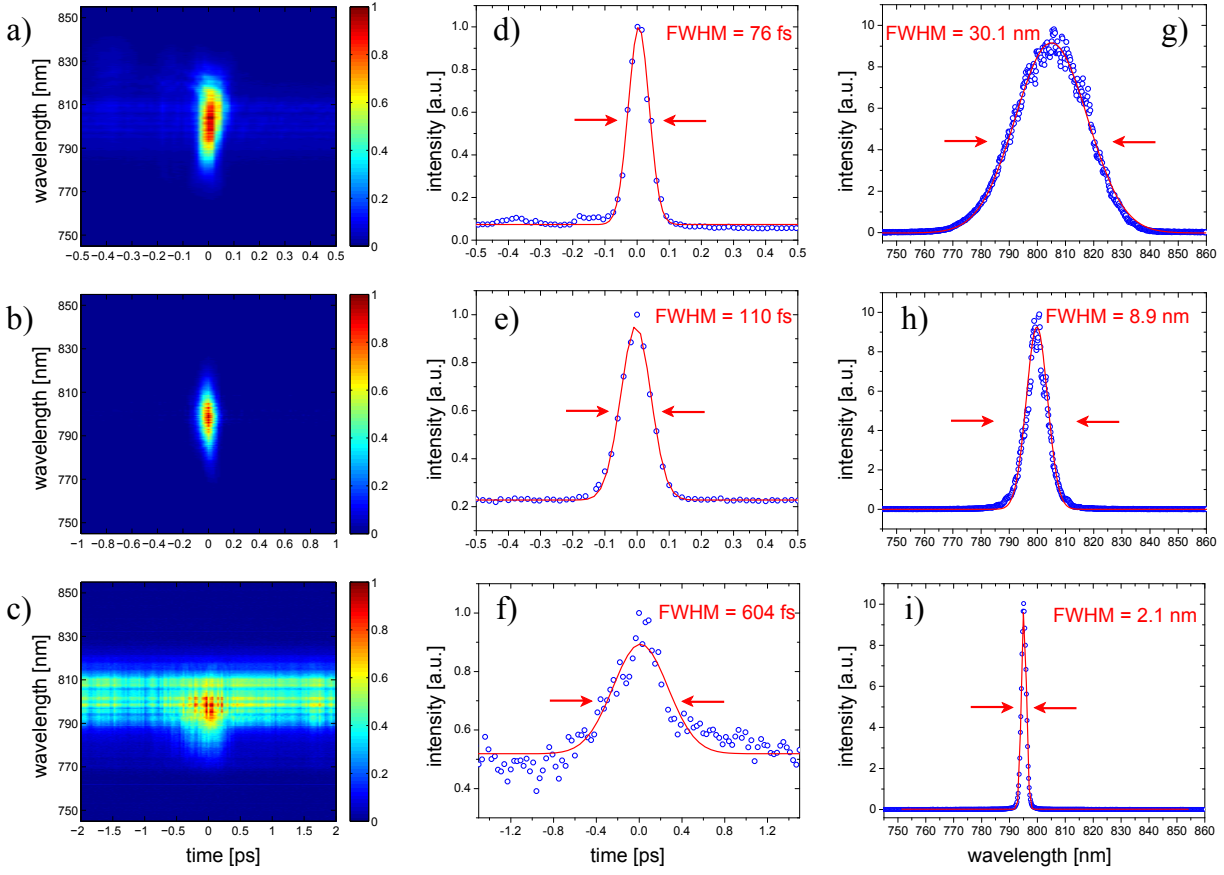
Figure 3.5: TG-FROG traces (first column) for three different probe pulses: (a) a short probe pulse (≈ 64 fs), (b) narrow band probe pulse (≈ 100 fs), and (c) very narrow probe pulse (≈ 610 fs). The corresponding spectrally integrated intensity versus time-delays are shown in the second column by the blue circles and the red line is a fit to the data points with a Gaussian function. In the third column, the spectra of the cross-correlated pulses which are used in this work for the observation of phonon polaritons are displayed.

pulse in the third line, a narrow band probe pulse is shown. For a spectral width of 9 nm or 2 nm, the data yield a pulse duration of FWHM = 100 fs or FWHM = 602 fs, respectively. Another important information obtained from the TG-Frog measurement is the signal-to-background ratio [71]. This depends on the fluence of each of the three mixed beams, on the sample quality (chemical and physical purity and the surface roughness), and on the precise alignment of the boxcar geometry, especially the displacement and divergence of the beams. This influences the amount of the parasitically scattered light which falls onto the detector slit. From the analysis of the TG-FROG data in figure 3.5 a signal-to-background ratio of 100:2 is derived for an unfiltered probe pulse, 100:22 for a 9 nm spectrally broad pulse, and 100:50 for the 2 nm broad pulse, respectively. A short synopsis of the pulse characteristics is given in table 3.2.

central wavelength λ_c	800 nm
bandwidths $\delta\lambda$	30 nm
pulse duration τ	64 fs
pump spot area A_{pump}	800x50 μm
probe spot area A_{probe}	700x30 μm
pump pulse fluence F_{pump}	12 mJ/cm^2
probe pulse fluence F_{probe}	5 mJ/cm^2
repetition rate	1 kHz

Table 3.2: Laser pulse parameters in the femtosecond pump probe experiment as obtained by the TG-FROG experiments.

3.4.4 Temporal Resolution

Now the temporal resolution of the pump-probe experiments can be determined. All measured responses are broadened, that is, convoluted in time with a Gaussian function with a width equal to FWHM = 64 fs which corresponds to a frequency of $f = 15.6$ THz. The amplitude, S, of
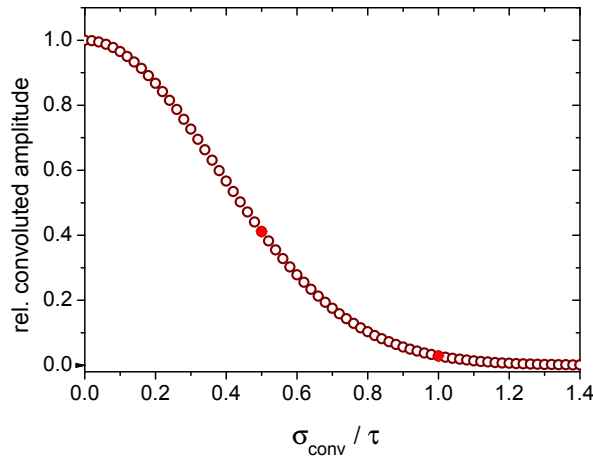
Figure 3.6: Relative amplitude of a cosine function after the convolution with a Gaussian function. The x-axis gives the ratio of the period of the cosine function τ and the width of the Gaussian function FWHM = σ_{conv}. Two prominent points at the ratio values of 0.5 and 1 are indicated in red color.

the convoluted signal depends on the ratio between the original signal period, τ, and the width, σ_{conv}, of the convolution function. In figure 3.6, the amplitude S is displayed as a function of

the ratio σ_{conv}/τ. Already at a ratio of 0.5, the signal decreases to 40% (marked by the red symbol in Fig.: 3.6) and at the condition $\sigma = \tau$, the signal decreases to 2% of the maximum value, respectively.

4 Frequency-Resolved Probe of Impulsively-Excited Phonon Polaritons

The first observation of phonon polaritons were made in the frequency domain using forward Raman scattering in 1965 in GaP [1]. Since then, phonon polaritons have been observed in various systems, e.g., ZnO [72], LiNbO$_3$ [73], BaTiO$_3$ [74], and LiTaO$_3$ [75]. The coherent polariton dynamics were also studied by stimulated Stokes scattering, also known as stimulated Raman gain, in LiNbO$_3$ [41, 76]. A bit more than a decade of year later, in the mid-1980s, the progress in femtosecond laser technology [77, 78] enabled the study of the polariton dynamics in the time domain [24, 46, 47, 79–83].

The inelastic light scattering from optical vibrational modes [84, 85] or phonon polariton modes in the frequency domain is described by Raman scattering [86, 87]. The observed relative frequency shifts of the scattered light $\Delta\omega$ is directly related to the frequency $\Omega_{vib} = \Delta\omega$ of the quasi-particle under investigation. Thus, in the frequency domain the conducted experiments directly reveal the wavevector $\Delta k = q$ and the frequency of the excited mode Ω_{vib} [1].

In the time domain the observation of coherent dynamics of the optical phonon modes is conducted in the pump probe scheme. The dynamics of phonons are observed through the modulation of scattered light intensity that results from a modulation of the refractive index by the propagating phonon polaritons. The modulation frequency ν_{mod} corresponds to the frequency of the mode $2\pi \cdot \nu_{mod} = \Omega_{vib}$. It is generally assumed that the optical probing of the propagating phonon polaritons occurs via a Raman interaction [39, 40]. A direct proof would be a shift of the frequency of the probe pulse [38]. However, since ultra-short pulses are required to obtain a high temporal resolution ($\Delta\omega_{pulse} >> \Omega_{vib}$), the frequency shift is obscured by the large bandwidth of the probe pulse itself. The direct experimental proof of the inelastic light shift in the fs-time domain spectroscopy of the optical vibrational modes was not reported yet (except of my own publication [88]).

In this chapter, the use of narrow bandwidth probe pulses resolves the inelastic light scattering from phonon polaritons in LiNbO$_3$ that reveals the Raman scattering process. The discussion which involves as well the excitation process is found in section 4.1. Next, the same experiment is repeated with short probe pulses and the data are analyzed under the consideration of a Raman process in section 4.2. Hereafter, both experimental schemes are compared in section 4.3. In

section 4.4 the energy and frequency selectivity of the excitation and probe process is discussed. The spectrum of the excited phonon polaritons is calculated for the case of the excitation in the transient grating geometry. Hereafter, the effects of the spectral broadening due to the finite lifetime of the generated phonon polaritons and finite size of the excitation spot are examined. The accuracy of the determination of the wavevector q and the frequency ω_{pp} of the observed phonon polaritons is estimated for the cases of the detection using narrow or broad bandwidth probe pulses.

4.1 Decoding of Raman Scattering Process: an Observation with Narrow Bandwidth Pulses

The experimental setup which is used for ISRS study of the phonon polaritons in LiNbO$_3$ was discussed in chapter 3 and is shown in figures 3.1 and 3.2. The two crossed and short ($\sim$ 64 fs) laser pulses $\mathbf{k}_1$ and $\mathbf{k}_2$ create a transient grating in the sample, from which two counter propagating phonon polaritons are impulsively excited. The crossing angle Θ_{air} of the pump pulses is set for selective excitation of the phonon polaritons with a wavevector of $q = 2300$ cm^{-1}. A probe pulse $\mathbf{k}_3$ arrives variably delayed at the same spot on the sample parallel to $\mathbf{k}_1$. A bandpass filter is placed into the path of the probe beam before the d-shape mirror and the transparent diffraction grating, as depicted in figure 3.2. This allows us to narrow its bandwidth to $\Delta\lambda =2$ nm which corresponds to a duration of 600 fs and which is longer than the oscillation period of the phonon polariton $\tau_{pp} = 1/\nu_{pp}$. The spectrum is shown in figure 4.1b. As the probe photons overlap in space and time with coherently launched polaritons they undergo inelastic Raman scattering and the probe pulse diffracts into the direction $\mathbf{k}_4$. The scattered light is than resolved by a spectrometer.

The transient spectral ISRS trace is shown in figure 4.1a. Two separated intensity lines for time-delays $\tau > 0$ which correspond to the Stokes scattering (red-shifted) of the probe light from the right-propagating polariton and the anti-Stokes scattering (blue-shifted) of the probe light from the left-propagating polariton are visible. For times relatively close to the time-delay zero, an additional scattered intensity in-between of the two transient Raman lines is observed. It is not shifted in frequency and is caused by the electronic part of the third-order nonlinearity when all three laser pulses coincide.

The analysis of the data is done by making a cut through the contour plot for later time-delays where the contribution of the electronic third-order nonlinearity is negligible. The obtained spectrum is shown together with the incident probe spectrum in figure 4.1b. The spectra are corrected for the background. The Raman frequency shift of $\Delta\nu = 2.02$ (2.08) THz directly yields the frequency ν_{pp} of the left- (and right-) propagating polariton. Hence the underlying stimulated
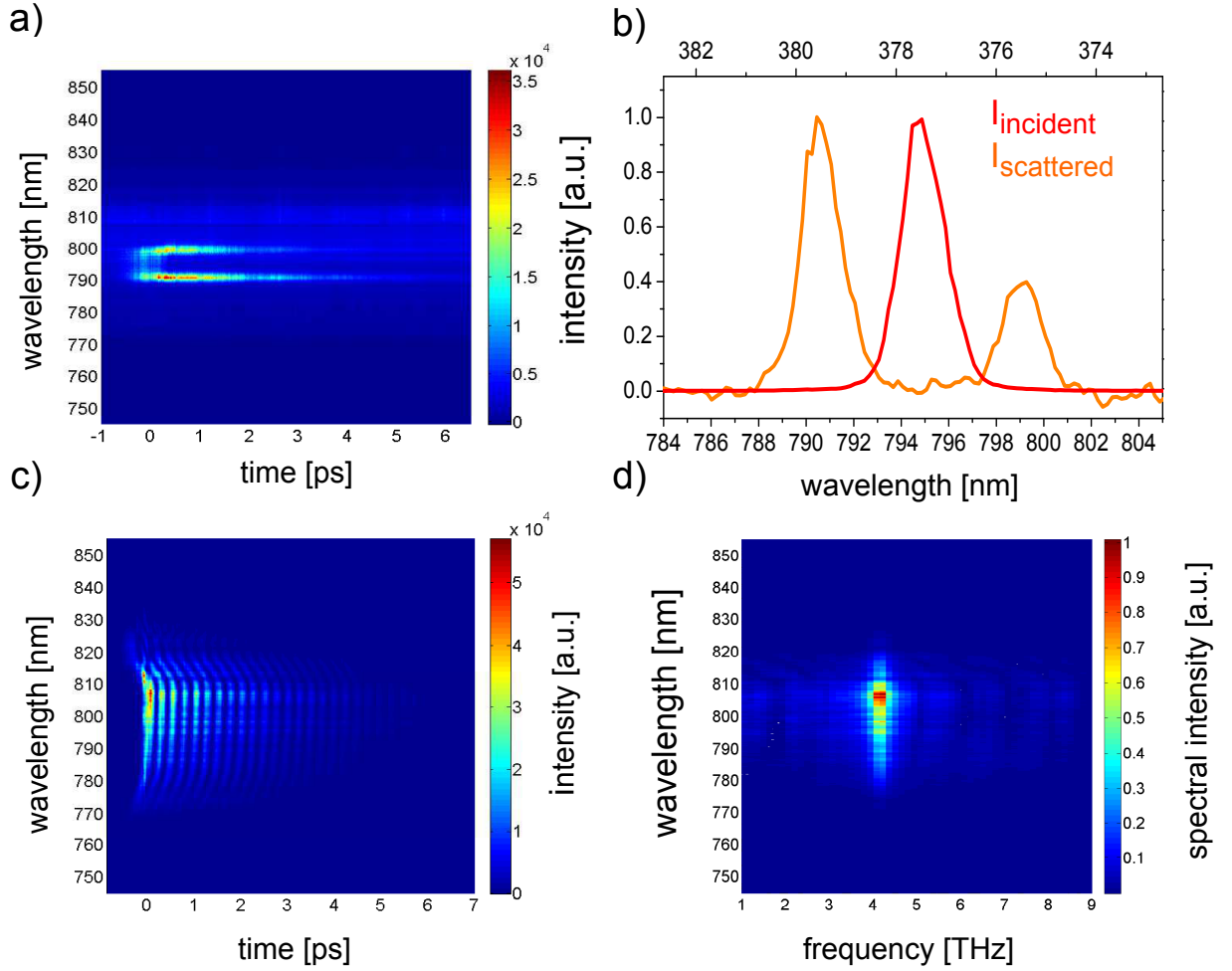
Figure 4.1: Frequency resolved transient ISRS data from LiNbO$_3$ for the selected wavevector $q = 2300$ cm^{-1}. The excitation and probe region overlap. The pump pulses are temporally short and spectrally broad. a) The probe pulses are spectrally narrow with a bandwidth of 2 nm. Distinct transient Stokes (red-shifted) and anti-Stokes (blue-shifted) intensity lines appear as the probe overlaps with the excited counter-propagating phonon polaritons. b) The incident and scattered probe spectrum. The frequency shifts amount to 2.0 THz (anti-Stokes) and 2.1 THz (Stokes). The scattered spectrum is obtained for delay-times around 2.5 ps. c) The same as in a) but the probe pulses are spectrally broad and temporally short. d) Fourier transform of the transient intensity shown in c) indicates a single frequency for all probe wave lengths. The signal oscillates at twice the frequency of the excited phonon polariton mode $2\nu_{pp} = 4.1$ THz.

Raman scattering process is now confirmed and the excitation process can be considered as a stimulated Raman process, too. The whole ISRS experiment includes the Stokes scattering in the

excitation step and subsequent a Stokes and anti-Stokes scattering in the probe step. The energy and momentum conservation diagrams are depicted in figure 2.8. The Stokes and anti-Stokes scattered light fields will interfere on the diode array of the spectrometer, if the probe pulses have a significant bandwidth. This leads to the homodyne detection scheme in the experiment, as will be discussed in chapter 5.

4.2 Measurement of the Damping Rate and Frequency of Phonon Polaritons: Observation with Short Probe Pulses
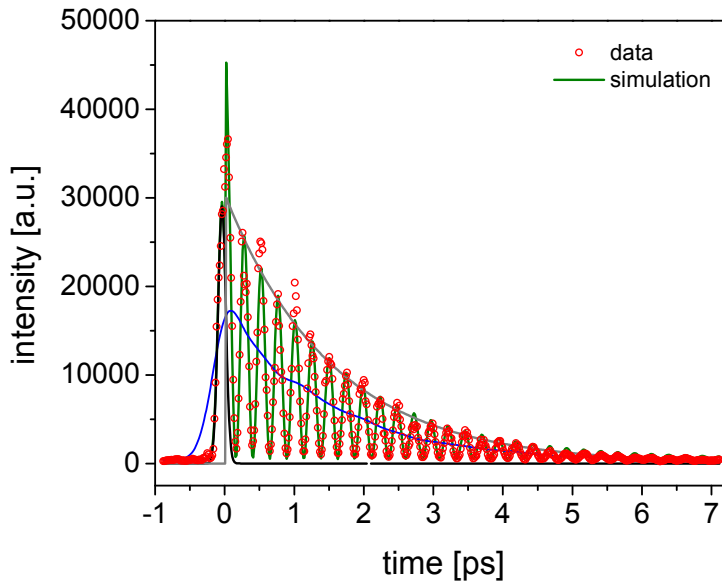

Figure 4.2: Spectrally integrated transient ISRS data (red circles) from figure 4.1a with an integration region between 798-804 nm is shown by the red circles. The intensity as function of time-delay is well described using equation 5.9 (green line). The black line shows the Gaussian function that was used to describe the electronic signal due to third-order nonlinearity of the crystal. An exponential decay multiplied with a step function, Φ, is displayed in gray. The blue line is a convolution of the signal with a Gaussian function with a temporal width of FWHM = 610 fs.

The same experiment as reported in the previous section 4.1 is repeated leaving all conditions the same, but no bandpass filter is inserted into the path of the probe beam. Thus the pump and probe pulses are temporally short ($\sim$ 64 fs) and spectrally broad. The transient frequency-resolved intensity is shown in figure 4.1c. The intensity maximum at the time-delay of $\tau = 0$ is caused by the instantaneous third-order electronic susceptibility, $\chi^{(3)}$, of the medium. The polariton response follows at the later time-delays $\tau > 0$. It exhibits a periodic modulation as function of the time-delay. The Fourier transform of the transient intensity shown in figure 4.1d

indicates the frequency $2\nu = 4.1$ THz for all wavelengths of the scattered probe light. Factor 2 comes from the sum of the Stokes and anti-Stokes shifted frequencies due to their superposition on the detector as deduced from the narrow bandwidth measurement in the previous section 4.1. A mathematical derivation is presented in chapter 5.

For further analysis of the data it is appropriate to select a small wavelength range where the oscillation amplitude is large. Otherwise the integration over a large range of the wavelengths will add up the intensities of the light without account for the different phases of the colors given in the spectrum. Thus the resulting oscillation amplitude will be washed out. An example for a small integration spectral range is shown in figure 4.2 as the red circles. The experimental data can be described by the function

$$S_\tau = I_0 + I_{el}e^{-\left(\frac{4ln2(\tau_0-\tau)^2}{\sigma^2}\right)} + I_\pm \sin^2(\omega_{pp}\tau - \varphi_0)e^{-2\gamma\tau} \cdot \Phi(\tau_0 - \tau) \ , \tag{4.1}$$

where I_0 denotes a constant background, the second term is a Gaussian function that describes the purely electronic $\chi^{(3)}$ sample response, and the last term accounts for the interference of the light fields scattered from the left- and right-propagating polaritons as given by the equation 5.9. The result of a fit to the data is shown as a green line in figure 4.2. It turns out, that the signal is modulated with twice the fundamental polariton frequency $2\nu_{pp}$ and decays with 2γ. $\Phi(\tau_0 - \tau)$ is a step function which ensures the immediate appearance of the scattered probe light due to the instantaneous generation of the phonon polaritons. The Fourier transform of the transient intensity and the simulation of the integrated intensity reveal the same result: a frequency $\nu_{pp} = 2.05$ THz and a damping rate $\gamma = 0.16$ THz of the phonon polariton with the wavevector magnitude of $q = 2300$ cm^{-1}.

The outcomes of this section are:

- the transient scattered intensity can be fit to the model of a damped harmonic oscillator as is assigned in equation 4.1. This means that the oscillation amplitude–which is associated with the polariton mode–is small and remains in the harmonic part of the vibrational potential.

- the frequency ν_{pp} and the damping γ_{pp} of the phonon polaritons are simultaneously observable in a ISRS experiment with short probe pulses

The analysis of the transient intensity has to consider interference effects of all incident light fields, that leads to the homodyne detection scheme. The mathematical treatment is presented in chapter 5.

4.3 Comparison of Narrow Bandwidth and Short Probe Pulse Experiment

The observation of impulsively excited polaritons is conducted with narrow bandwidth pulses and temporally short pulses. To compare both methods a further analysis of the obtained transient ISRS traces is made, which are shown in figures 4.1a and 4.1c. First, the transient spectra are spectrally integrated in the same wavelength region from 787 nm to 803 nm. The integrated intensities are plotted as a function of time in figure 4.3a as a black and red line, respectively.
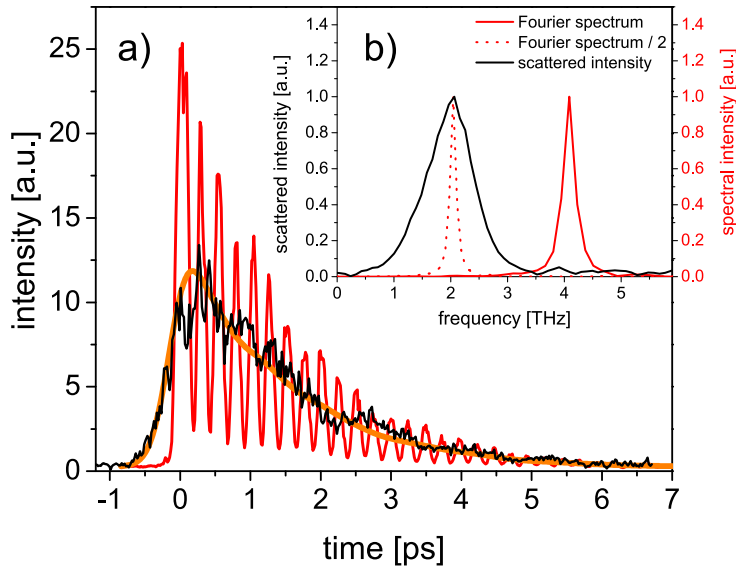

Figure 4.3: Transient ISRS data from LiNbO$_3$ for the wavevector magnitude $q = 2300$ cm^{-1}. a) Red line: the transient intensity is obtained with temporally short probe pulses and spectrally integrated a for further analysis. The oscillation frequency is twice the frequency of the phonon polariton $\nu = 2\nu_{pp}$. Thick black line: spectrally integrated transient intensity obtained with probe pulses of 2 nm bandwidth (610 fs). Orange line: convolution of the red line with a Gaussian function with a temporal width of FWHM = 610 fs. b) Red solid line: normalized power spectrum as obtained after the Fourier transform of the transient ISRS intensity (red line in a)). Red dashed line: The same spectrum but scaled with a factor of two. Black line: anti-Stokes spectrum detected on the spectrometer obtained by the narrow band probe pulses. The frequency is shifted relative to the incident probe spectrum.

Further, the signal obtained from the short probe pulse experiment is convoluted with a Gaussian function of a temporal width of FWHM = 610 fs and scaled. The result is shown by the orange line in the same figure. A nice agreement is visible between the black and orange line. They exhibit very similar increase and decrease behavior, because in both cases the envelope of the intensity indicates the effective overlap of the probe volume and the propagating phonon polaritons. The overlap conditions are assumed to be the same. Moreover, both intensities decay

with twice the polariton decay rate as predicted by equations 5.9 and 5.13 mainly due to the dephasing effect.

Figure 4.3b shows the normalized power spectrum as a red solid line which was obtained from the Fourier analysis of the data depicted by the red line in figure 4.3a. The same power spectrum scaled by a factor of two is shown by the red dashed line. It peaks at 2.05 THz which is the polariton frequency ν_{pp}. The spectrum that corresponds to the anti-Stokes peak of the Raman shifted narrow bandwidth pulse is plotted as a black line, too. It indicates a frequency $\nu_{pp} = 2.05$ THz of the polariton. Both experimental schemes yield the same frequency ν_{pp} of the excited polariton mode.

In the following, the limitations of both experimental schemes, namely the observation of impulsively excited phonon polaritons using either a narrow bandwidth and temporally long or a broad bandwidth and temporally short probe pulse, are compared. This is done with respect to the probe of excited phonon polaritons with different wavevectors q as is the case in the measurement of the dispersion relation of the phonon polaritons, which is the topic of chapter 8. In this part, I distinguish three different regions of the dispersion relation of the phonon polaritons in LiNbO$_3$ that are defined by the characteristics of the used probe pulses: first, a regime where the frequency of phonon polaritons ν_{pp} is smaller than the bandwidth of the narrow bandwidth probe pulses $\Delta\nu_{narrow} < \nu_{pp}$, a regime where the polariton frequency is almost equal or larger than half of the bandwidth of the short probe pulses, $0.5 \cdot \Delta\nu_{broad} \lesssim \nu_{pp}$, and last an intermediate regime. The use of both experimental schemes is not equally well applicable to all these three regions:

Low frequencies region ($\nu_{pp} < 1$ THz)

Here, the Raman shifts induced by the scattering from phonon polaritons are comparable with the spectral width of the narrow bandwidth probe beam (FWHM $= 2$ nm $\,\widehat{=}\, 0.95$ THz), the Stokes- and anti-Stokes-shifted light fields of a narrow bandwidth probe pulse will be not clearly separated in frequency and will interfere in the spectrum. Thus, it will be difficult to determine the position of Stokes- and anti-Stokes lines. The experiment with short probe pulses will have a very good temporal resolution of the phonon polariton oscillation with relatively low frequency. Thus, for low polariton frequencies the short probe pulses will yield more accurate results in determination of polariton frequency ν_{pp}.

Intermediate frequency region (1 THz $< \nu_{pp} < 7$ THz)

The main dispersion region of the lowest phonon polariton branch in LiNbO$_3$ lies in this frequency range. Here, both experimental schemes are equally accurate in the determination of the polariton frequency.

High frequencies region ($\nu_{pp} \gtrsim$ 7 THz)

For frequencies larger than 7 THz, the duration of the short pulses ($\sim$ 65 fs) is comparable to half of the oscillation period $\tau_{pp} = 1/2\nu_{pp}$ of the phonon polaritons. According to Nyquist–Shannon sampling theorem, faster oscillations will not be fully resolved by such a probe pulse. Assuming $\nu = 7.56$ THz, which is the frequency of the lowest TO phonon, the corresponding period is $\tau_{pp} = 66$ fs. This is exactly the duration of the short pulses. In contrast, the relatively large frequencies of phonon polaritons lead to well-separated Stokes and anti-Stokes lines in the observation of phonon polaritons with narrow bandwidth pulses.

Moreover, the observation of phonon polaritons that belong to the dispersion branch approaching the fourth TO-mode in LiNbO$_3$ can solely be performed with narrow bandwidth pulses, as will be further discussed in chapter 8. The frequency of these phonon polaritons amounts to $\nu_{pp} \sim 18$ THz, which is still within the bandwidth of the excitation pulses $\Delta\omega_{1/e} = 18$ THz. In this case, these phonon polaritons can still be generated by spectrally broad and temporally short pulses. But the time-resolution of the short pulses is not sufficient to resolve the oscillation with such high frequencies. Whereas the probe with narrow bandwidth pulses do not suffer from the issue of temporal resolution. Thus, the main advantage of the pump-probe scheme with temporally short pump pulses and spectrally narrow bandwidth probe pulses is the increased frequency range, in which the stimulated phonon polaritons can be observed.

4.4 Selectivity of the Excitation and Probe Process of the Phonon Polariton Modes in the TG-Experiment

As discussed in sections 4.1 and 4.2, we observe selectively excited phonon polaritons in two different ways, namely using either narrow bandwidth or temporally short probe pulses. In both cases, probe light simultaneously undergoes Raman scattering from left- and right-propagating phonon polaritons. This explains the observed transient behavior of the detected spectra, which are shown in figures 4.1a and 4.1c, respectively. Both data sets were already analyzed and compared in section 4.3 and the corresponding spectral analysis and Fourier transform are depicted in figures 4.1b and 4.1d, respectively. Both experimental schemes yield the same frequency ν_{pp} of the excited polariton modes.

In the following, a detailed discussion of the mode selectivity in the excitation process and the selectivity and sensitivity of the probe process for both experimental schemes is presented. The discussion is based on two different measurements: the first one detects phonon polaritons with a wavevector of $q = 2300$ cm^{-1}. The corresponding spectrally narrow bandwidth measurement and the Fourier transform of the transient spectrum detected with spectrally broad bandwidth and temporally short pulses are shown in figure 4.4c. The second measurement observes phonon

polaritons with a wavevector of $q = 19000$ cm^{-1}. The spectrum of scattered narrow bandwidth probe pulses and the Fourier transform of the transient intensity recorded with temporally short pulses is shown in figure 4.4b. These two measurements are examined to highlight the possible differences that occur during the excitation and detection of phonon polariton wavepackets with different wavevectors q. The way of proceeding is as follows: first, the spectrum of the excited phonon polaritons is calculated for the case of the wavevector-selective excitation in the transient grating geometry. Then, the effect of the finite size of the pump beams on the width of the excited polariton spectrum is considered. This is followed by the calculation of the spectral broadening of the phonon polariton modes due to their frequency-dependent finite lifetime. Hereafter, the accuracy of the determination of the wavevector q and the frequency ω_{pp} of the detected phonon polaritons is discussed for the case of the detection using narrow and broad bandwidth probe pulses. These factors are important for the correct interpretation of the measurement of the dispersion relation of phonon polaritons, which will be presented later in chapter 8. Various different contributions that can cause the spectral broadening and the obtained frequency and wavevector values for the two discussed measurements are listed in the tables 4.1 and 4.2, respectively.

Calculation of the spectral bandwidth of excited phonon polariton modes

The bandwidth $\Delta\omega_{pp}$ of the spectrum of the phonon polariton modes is given by the bandwidth of the excitation pulses $\Delta\omega_{pump}$. In the excitation process, the energy conservation $\omega_1 - \omega_2 = \omega_{pp}$ and momentum conservation $\vec{k}_1 - \vec{k}_2 = \vec{q}$ rules apply for the case of three interacting particles. This results in the selectivity of the excited modes in the experiment. The wavevector of phonon polaritons is given by

$$q^2 = k_1^2 + k_2^2 - 2k_1 k_2 \cos(\Theta) \quad . \tag{4.2}$$

Considering the case $k_1 > k_2$ and $\omega_2 = \omega_1 - \omega_{pp}$, equation 4.2 can be rewritten as

$$\omega_{pp}^2 = \frac{c_{THz}^2(\omega_{pp})}{c_{800}^2}(\omega_1^2 + (\omega_1 - \omega_{pp})^2 - 2\omega_1(\omega_1 - \omega_{pp})\cos(\Theta)) \quad . \tag{4.3}$$

This equation describes the frequency ω_{pp} of the phonon polariton as a function of the frequency of the visible light, ω_1, and a constant intersection angle of the two pump pulses, Θ. Note, all the colors in the pulses impinge on the sample under the same angle. Equation 4.3 can be solved for ω_1 in order to use the result for further modeling. In order to calculate the spectrum of phonon polaritons, I_{pp}, one has to assume the spectral shape of light intensities of the pump pulses, $I_1(\omega_1)$ and $I_2(\omega_2)$. For a more simple discussion, I will assume a Gaussian shape for both pulses. Now, the spectrum of the phonon polaritons is described by

$$I_{pp}(\omega_{pp}) = I_1(\omega_1)I_2(\omega_2) = I_1(\omega_1)I_2(\omega_1 - \omega_{pp}) \quad , \tag{4.4}$$
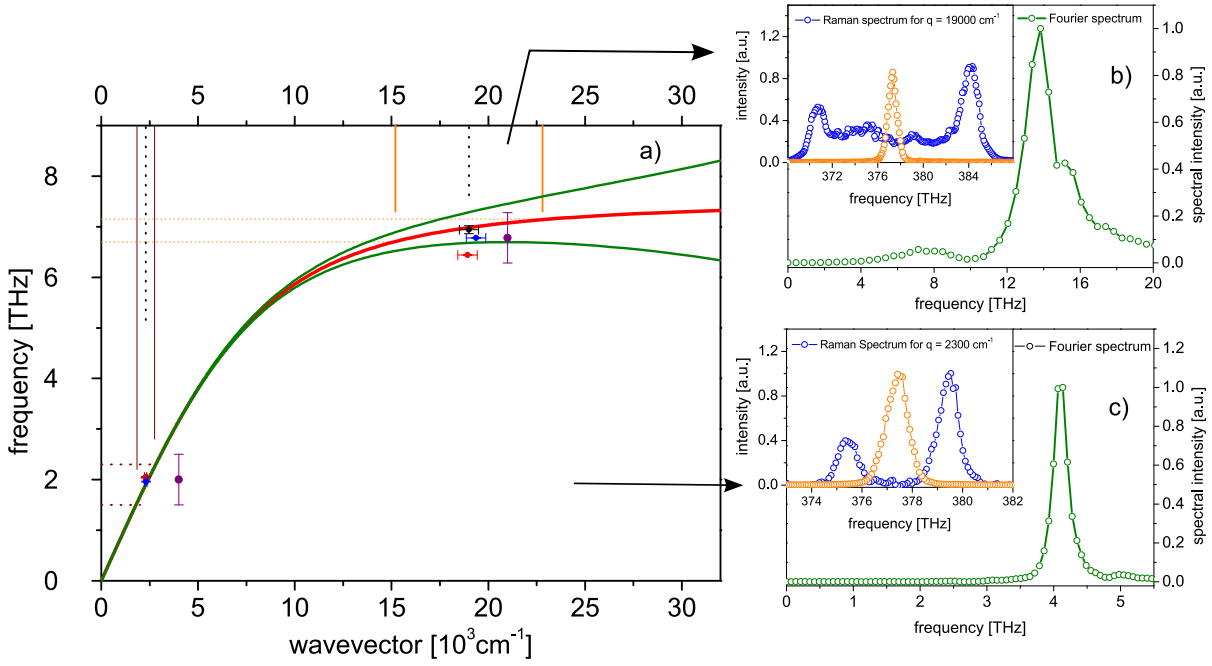
Figure 4.4: a) Red line: Calculated dispersion relation of phonon polaritons using parameters that are optimized during the fitting analysis as described in chapter 8. The parameters are listed in third column in table 8.1. Green lines indicate the effect of the spectral broadening caused by the finite lifetime of the phonon polaritons. The data that are measured with temporally short probe (with narrow bandwidth probe) pulses are shown by the black dots (red and blue dots). The errorbars are given in table 4.2. Purple dots are used to illustrate the bandwidths of the narrow probe pulses (FWHM = 0.95 THz), where these data points are displaced along the q-axis. Orange and brown lines indicate the two regimes that are discussed in the text. The relative bandwidths of the excited wavevectors is exaggerated in the figure and amounts to $\delta q = 0.2$. b) Power spectrum obtained with the Fourier analysis of the transient spectrum detected with broad bandwidth pulses in the case of excited phonon polaritons with wavevector $q = 19000$ cm^{-1}. Inset in b): Raman spectrum (blue dots) detected using narrow bandwidth pulses that are scattered from the phonon polaritons with the same wavevector magnitude. The spectrum of the incoming narrow bandwidth pulse is shown by the orange dots. c) The same as b) but for $q = 2300$ cm^{-1}. Inset in c): the same as in the inset in b) but for $q = 2300$ cm^{-1}.

where $\omega_2 = \omega_1 - \omega_{pp}$ and ω_1 is given by equation 4.3. The calculated spectrum is shown in figure 4.5 as black line for an intersection angle of both pump pulses of $\Theta = 0.69°$, which corresponds to the angle that was set in the experiment presented in figure 4.4c where a phonon polariton with the wavevector $q = 2300$ cm^{-1} was observed. In this calculation, the frequency-dependent refractive index in the terahertz region, $n_{THz}(\omega_{pp}) = \sqrt{\epsilon(\omega_{pp})}$, is used and the dielectric function is given by equation 2.3. The spectrum exhibits a width of $\Delta \nu = 0.055$ THz. Further, the same calculation of the spectrum of the excited phonon polariton modes is done for an intersection

angle of $\Theta = 6.3°$, which results in a polariton wavevector of $q = 19000 \text{ cm}^{-1}$. This case applies for the measurement shown in figure 4.4b. The result of this calculation is shown as purple line in figure 4.5. The width of this spectrum is $\Delta \nu = 0.028$ THz, which is half the width of the calculated spectra of the phonon polaritons with a central frequency of 2.1 THz. This behavior can be explained in the following way: in the experiment, the central frequency of the laser pulses $c_0/\lambda_c = \nu_c$ and the intersection angle Θ determines the central wavevector q_c and frequency $\omega_{pp,c}$ of the excited phonon polaritons according to equation 4.3. This is indicated by the black doted lines in figure 4.4a for the two discussed cases. Due to the finite bandwidth of the laser pulses the wavevector of the phonon polaritons exhibits a bandwidth too. In the linear region of the dispersion relation, the relative bandwidth of the excitation pulses ($\delta \nu = 0.0375$) is equal to the relative bandwidth of the polariton wavevector $\delta q = \delta \nu$. The region of allowed polariton wavevectors is marked by the orange and brown solid lines for an exaggerated relative bandwidth of $\delta q = 0.2$, respectively. The corresponding allowed frequencies of the phonon polaritons are inferred from the projection of the segment of the x-axis on the modeled dispersion curve, as indicated by the dashed orange and brown lines in figure 4.4a. One immediately realizes that, the range of the excited frequencies of the phonon polaritons for large wavevectors and frequencies is smaller than for the phonon polaritons excited at small wavevectors and frequencies. This is due to the increase of the frequency-dependent refractive index with increasing frequencies, which leads to a smaller slope of the dispersion curve at high frequency.

The finite size effect of the excitation spot

The number of interference fringes within the region of the pump spot defines the sharpnes of the excited polariton modes. Thus, the spectral bandwidth of the excited polariton modes depends on the finite size of the pump spot. As previously reported in section 3.4.1, the resulting width of the defined wavevector is $\Delta q \sim 60 \text{ cm}^{-1}$. To account for this finite-size effect, one has to convolve the calculated phonon polariton spectrum with the function of the Fourier transform of the interference pattern that–in this work–is assumed to be a Gaussian function. First, I estimate under which circumstances the bandwidth of the wavevector Δq will lead to a larger broadening $\delta \nu_{fin} = \delta q$ of the frequency in the linear region of the dispersion relation than the bandwidth of the spectrum $\delta \nu_{pp}$ of the excited phonon polaritons. For wavevectors $q < \Delta q/0.026 = 2300 \text{ cm}^{-1}$ the broadening of the polariton spectrum is mostly determined by the finite-size effect. Now, for the two examples that are discussed in this section, the broadening due to the finite size of the excitation pulses is calculated to be $\Delta \nu_{fin} = \Delta q/q \cdot \nu_{pp} = 5.3 \cdot 10^{-2}$ THz for $q = 2300 \text{ cm}^{-1}$ and $\Delta \nu_{fin} = 2.15 \cdot 10^{-2}$ THz for $q = 19000 \text{ cm}^{-1}$. At the same time, the spectral widths of the excited polariton modes, which are shown as black and purple lines in figure 4.5, amount to $\Delta \nu_{pp} = 5.5 \cdot 10^{-2}$ THz and $\Delta \nu_{pp} = 2.8 \cdot 10^{-2}$ THz, respectively. Evidently,
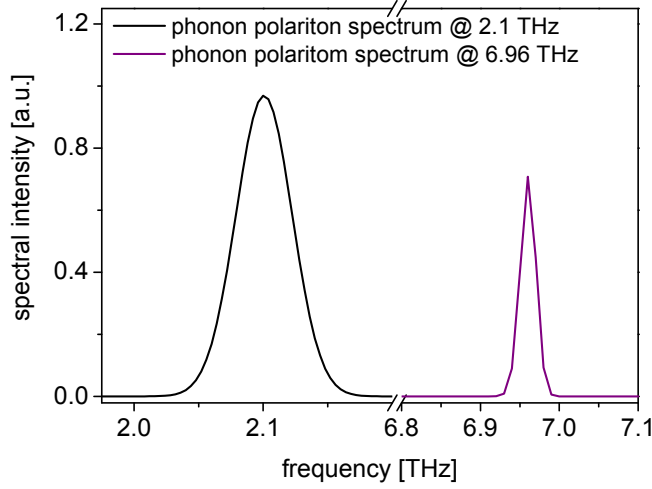
Figure 4.5: Calculated spectrum of excited phonon polaritons for the intersection angle of both pump pulses $\Theta = 0.69°$ and $\Theta = 6.3°$ are shown by the black and purple lines. The calculation uses equations 4.4 and 4.3 and a frequency-dependent index of refraction. The spectral width of the spectrum amounts to $\Delta\nu = 0.055$ THz ($\delta\nu = 0.026$) and $\Delta\nu = 0.028$ THz ($\delta\nu = 0.004$). The peaks are centered at 2.1 THz and 6.96 THz. Further parameters used in the calculation are: $n_{800} = 2.163$, $2\pi/\lambda_c = 375$ THz, and $\Delta\nu_{pump} = 14$ THz.

the enhanced narrowing of the polariton spectrum with higher frequencies requires to take into account the broadening caused by the finite size of the excitation grating. Further, the convolution of two Gaussian functions with the widths σ_1 and σ_2 yields again a Gaussian function with the new width $\sigma_3^2 = \sigma_1^2 + \sigma_2^2$. This results in the spectral widths of the generated polariton modes $\Delta\nu_{pp} = 7.9 \cdot 10^{-2}$ THz and $\Delta\nu_{pp} = 3 \cdot 10^{-2}$ THz for the case of $q = 2300$ cm^{-1} and $q = 19000$ cm^{-1}, respectively, which correlates to the expectations. Moreover, a larger pump spot reduces the finite size effect. For a given ratio M of focal lengths of the lenses that are used to write the grating pattern into the sample, the size of the pump spot can easily be changed using two lenses with longer focal lengths. The disadvantage is a decreased fluence of the pump beams.

Spectral broadening due to the finite lifetime of excited phonon polaritons

Phonon polaritons exhibit a frequency-dependent damping, which increases toward the frequency of the TO-phonon modes, where the imaginary part of the phonon polariton wavevector, $\text{Im}(q)$, increases too. This results in a finite lifetime of the excited phonon polaritons and causes a spectral broadening of the probe light. In figure 4.4a, the calculated influence of the spectral broadening on the dispersion relation is indicated by the green solid lines. The imaginary part of the wavevector $\text{Im}(q)$ is related to the damping rate of phonon polaritons $\gamma_{pp} = \omega_{pp} \cdot \text{Im}(q)/\text{Re}(q)$

according to equation 9.3, which will be later derived in chapter 9. The broadening becomes significant for larger phonon polarition frequencies. Actually, the Stokes and anti-Stokes lines, which are shown as blue dots in the inset of figure 4.4b, are about two times broader than the incident narrow bandwidth pulse (~ 0.95 THz). The Stokes and anti-Stokes lines of light that undergoes Raman scattering from phonon polaritons with the wavevector $q = 2300$ cm^{-1} are shown by the blue dots in the inset of figure 4.4c and do not show any signatures of a spectral broadening, which is in agreement with the model calculation. The calculated spectral broadening of the excited phonon polaritons with the frequencies, which are discussed in this section, are listed in table 4.1. For the wavevector $q = 19000$ cm^{-1} the expected contribution due to the finite lifetime is one order of magnitude larger, than the other contributions.

		$q = 2300$ cm^{-1}	$q = 19000$ cm^{-1}
$\delta\nu$	[THz]	0.055	0.028
$\delta\nu_{fin}$	[THz]	0.053	0.0215
$\sqrt{(\delta\nu)^2 + (\delta\nu_{fin})^2}$	[THz]	0.076	0.035
$\delta\nu_{\gamma_{pp}}$	[THz]	0.0	0.3

Table 4.1: Different contributions to the broadening of the frequency of the excited phonon polaritons in the transient grating experiment, as discussed in this section: $\delta\nu$ - broadening due to the bandwidth of the excitation pulses, $\delta\nu_{fin}$ - broadening due to the finite size of the excitation region, $\delta\nu_{\gamma_{pp}}$ - broadening due to the finite lifetime of excited phonon polaritons.

Determination of the frequency of generated phonon polaritons in an experiment using temporally short probe pulses

After the discussion of the excitation process, now the focus lies on the measurement of the frequency ω_{pp} of the generated phonon polaritons. The measurement of ω_{pp} using broad bandwidth probe pulses yields the sum of the frequencies of right- and left-propagating phonon polaritons. In principle, the hole spectrum of generated excited phonon polaritons is simultaneously probed. The measured data compose a spectral trace as shown in figure 4.1c. The data can be Fourier transformed for each individual wavelength. This analysis provides an oscillation frequency for each optical wavelength. The result of the data evaluation is depicted in figures 4.6a and 4.6b, respectively. The frequencies scatter around the mean value $\nu_{pp} = 4.095$ THz (13.88 THz) with a standard deviation $\sigma = 0.007$ THz (0.15 THz) for excited phonon polaritons with $q = 2300$ cm^{-1} (19000 cm^{-1}). The larger scattering of the data for $\nu_{pp} = 13.88$ THz can be explained by the existence of an additional peak in the Fourier spectrum, which is centered at $\nu = 15.3$ THz and
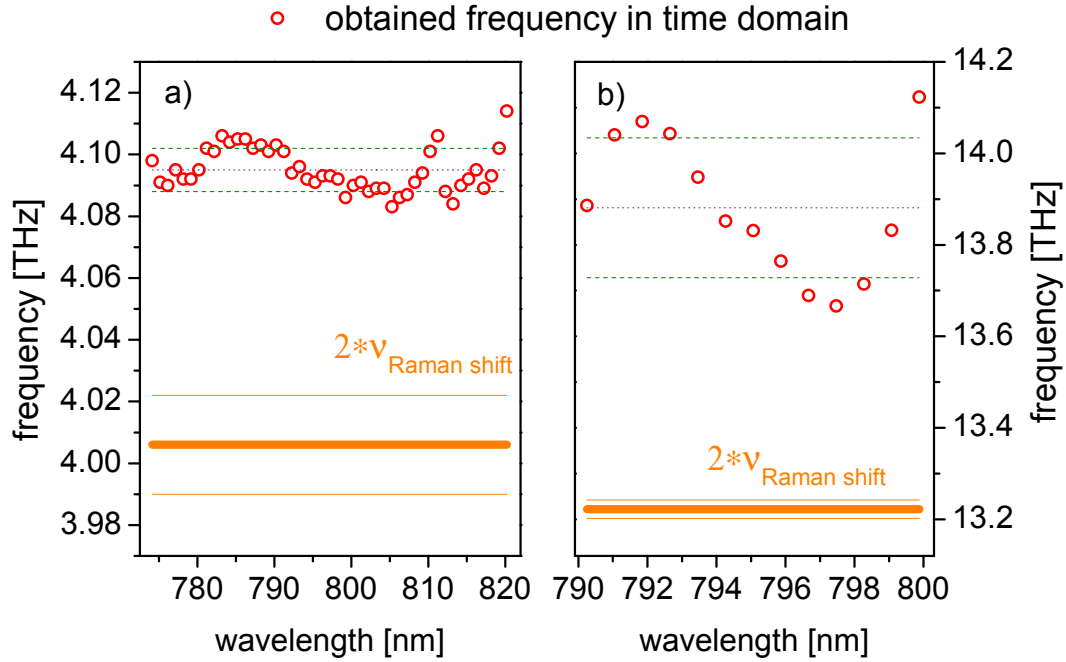
Figure 4.6: Obtained frequency of probed phonon polaritons as function of the carrier wavelength of the probe light. a) (b) One of the evaluated Fourier spectra is shown in figure 4.1c (4.1b). The average frequency $\nu_{pp} = 4.095$ THz (13.88 THz) and the standard deviation $\sigma = 0.007$ THz (0.15 THz) are indicated by the violet and green lines, respectively. Orange dashed line indicates the frequency which corresponds to twice the average frequency shift of Raman scattered narrow bandwidth probe light that is shown in figure 4.1c or 4.1b.

subsequently influences the shape of the main peak. The nature of this peak can be explained considering the summation of two frequencies, namely the frequency of the phonon polariton that belongs to the lower dispersion branch, $\nu_{pp} = 6.95$ THz, and a phonon polariton that belongs to the second branch of the dispersion relation with a frequency $\nu_{pp} = 8.25$ THz. For more details see section 7.2. Further, the region where the transient intensity exhibits oscillations is in the case of $\nu_{pp} = 13.88$ THz five times smaller, than in the case of small frequencies. This result quantitatively proofs the predicted narrowing of the spectrum of generated phonon polaritons.

Determination of the frequency of the generated phonon polaritons in an experiment using narrow bandwidth probe pulses

The narrow bandwidth spectrum (FWHM ~ 1 THz) is only a small subset of the spectrum of the excitation pulses, which amounts to FWHM ~ 14 THz. Thus, only thous phonon polaritons are observed, which were previously generated by the mixing of probe light with

exactly the same wavelengths as subsequently contained in the narrow bandwidth probe pulses, as previously discussed in section 2.5.2. The Stokes (-) and anti-Stokes (+) shifted light probes the corresponding left- and right-propagating polariton modes. As shown in figure 2.13 in section 2.5.2, the frequency shift of Stokes and anti-Stokes scattered light is not exactly the same, because somewhat different spectral components of the excited phonon polariton modes are probed. The measured scattered spectra are shown in the inset of figure 4.4c for the case of $q = 2300$ cm^{-1}. The observed frequencies are those of the light that undergoes Stokes scattering ($\nu = 375.434 \pm 0.008$ THZ), anti-Stokes scattering ($\nu = 379.444 \pm 0.008$ THz), and that of the incoming light ($\nu_{in} = 377.403 \pm 0.002$ THz). The uncertainty of the measured frequencies is very low because the center of the peaks is well-determined. In the discussed case one obtains $\Delta\nu = 0.008$ THz. The Stokes and anti-Stokes frequency shifts amount to $\nu_{pp,-} = 1.96 \pm 0.008$ THz and $\nu_{pp,+} = 2.04 \pm 0.008$ THz, respectively.

The inset in figure 4.4c depicts the spectrum of light that undergoes Raman scattering from phonon polaritons with $q = 19000$ cm^{-1}. The intensity peaks are centered at $\nu = 384.08 \pm 0.01$ THz and $\nu = 370.86 \pm 0.01$ THz. The center frequency of the incoming probe light is determined to $\nu = 377.3 \pm 0.002$ THz, hence, the determined phonon polariton frequencies amount to $\nu_{pp,-} = 6.78 \pm 0.01$ THz and $\nu_{pp,+} = 6.44 \pm 0.01$ THz, respectively.

In figures 4.6a and 4.6b the average values of the phonon polariton frequency multiplied by two are shown. The factor of two is included here to compare with the oscillation frequency obtained in the time domain measurement, which in this case consists of the sum of the frequencies of the right- and left-propagating phonon polariton. For small frequencies ($\nu_{pp} \sim 2$ THz), the position of the Fourier peak is determined with higher accuracy as the measured average Stokes and anti-Stokes frequency shifts, which are multiplied by a factor of two. As indicated by the orange and green lines in figure 4.6a the difference in the accuracies of the determination of the phonon polariton frequency amounts in this case to two. Certainly, for larger frequencies ($\nu_{pp} \sim 6.9$ THz), the observed frequency shift in the experiment with narrow bandwidth probe pulses yields a more precise determination of the frequency (see figure 4.6b). In this case, the precision is seven times higher in the experiment with narrow band pulses. This outcome clarifies the limited time-resolution of short probe pulses in the time domain experiment, as discussed in section 4.3.

Furthermore, the determined standard deviation or the confidence interval in the fit analysis of the Raman lines implies a higher precision in the determination of the observed frequencies of phonon polaritons. But the scattered narrow bandwidth pulses–if one disregards any broadening effects–show that all wavelengths simultaneously scatter from the excited phonon polaritons. The spectrum of the phonon polaritons possesses a large enough bandwidth to interact with all photons within the bandwidth of the incident narrow probe pulse (FWHM = 0.95 THz) where the same energy and momentum rules as in the initial generation process apply. This means

that each wavelength in the scattered probe spectrum corresponds to a specific probed mode of the generated phonon polariton spectrum. If one plots the bandwidth of the probe pulse into the figures 4.6a and 4.6b, both experimental schemes yield phonon polariton frequencies that lie within these limits.

Measurement of the wavevector of the transient grating

The determination of k_{tg} for smaller values than 2400 cm^{-1} is done with a CCD camera as explained in section 3.4.1. For the larger wavevectors the camera is not able to resolve the interference pattern of the two crossed pump beams properly. In this case, the intersection angle Θ has to be measured directly. During this work, this is done by measuring the distance of the two parallel pump beams before the last focusing lens. The accuracy of the measurement amounts to $\Delta l = 0.5$ mm. Hereafter, the angle is then calculated using the measured value of l and from the known focal length ($f = 75$ mm) of the last focusing lens. The distance amounts for the case of $q = 2300$ cm^{-1} and $q = 19000$ cm^{-1} to $l = 2$ mm or $l = 18$ mm, respectively. This corresponds to an angle $\Theta = 0.69 \pm 0.17$ ° and $\Theta = 6.3 \pm 0.17$ °. Thus, the wavevector of the transient grating is for the two discussed cases $k_{tg} = 2094 \pm 480$ cm^{-1} and $k_{tg} = 18800 \pm 480$ cm^{-1}.

wavevector	frequency
$q = 2295 \pm 60$ cm^{-1}	$\nu_{pp} = 2.05 \pm 0.004$ THz
$q = 19000 \pm 500$ cm^{-1}	$\nu_{pp} = 6.94 \pm 0.08$ THz
$q_+ = 2284 \pm 60$ cm^{-1}	$\nu_{pp,+} = 2.04 \pm 0.008$ THz
$q_- = 2308 \pm 60$ cm^{-1}	$\nu_{pp,-} = 1.96 \pm 0.008$ THz
$q_+ = 18930 \pm 500$ cm^{-1}	$\nu_{pp,+} = 6.44 \pm 0.01$ THz
$q_- = 19370 \pm 500$ cm^{-1}	$\nu_{pp,-} = 6.78 \pm 0.01$ THz

Table 4.2: Obtained wavevectors and frequencies of the selectively excited phonon polaritons using temporally short or narrow bandwidth probe pulses, respectively.

Determination of the wavevector of the excited phonon polaritons

First, I discuss the experiment with temporally short probe pulses. Once the wavevector of the transient grating k_{tg} and the frequency of the observed phonon polaritons ν_{pp} is determined, the polariton wavevector q is calculated using equation 2.10 and the data point with the coordinates (q, ν_{pp}) is subsequently defined. Table 4.2 lists the obtained wavevectors and frequencies for the two exemplary cases in this section.

Next, in the experiment with narrow bandwidth pulses, the frequency of right- or left-propagating phonon polaritons are determined from the relative positions of the anti-Stokes or Stokes intensities, respectively. The wavevector is calculated with equation 2.28 and two coordinate pairs, namely $(q_+, \nu_{pp,+})$ and $(q_-, \nu_{pp,-})$, are obtained. Like in the case of the experiment with temporally short probe pulses, the uncertainty in the determination of the polariton wavevector is mainly caused by the measurement of the angle between the incoming and scattered probe light. During this work, no noticeable deviations of the direction of the incoming and scattered narrow bandwidth pulses compared to the temporally short probe pulses is observed. Thus, the same considerations, as in the previously discussed case, applies for the uncertainty of the observed wavevector of the excited phonon polaritons. The values of determined wavevector and frequency pairs are listed in the lower half of table 4.2.

In figure 4.4 the experimentally obtained data points and the corresponding errorbars are plotted together with data points that indicate the bandwidth of the narrow probe pulses. We see that all data points in the region of 2 THz lie on the model dispersion curve. In the frequency region around 6.8 THz, two of the data points lie within the calculated spectral broadening of the phonon polariton modes. However, the red point, which is determined from the measured frequency shift of light that undergoes Stokes scattering from the left-propagating phonon polariton and is "red-shifted", lies somewhat outside of this frequency region. Nevertheless, the deviation from the dispersion curve (red line) is smaller than the half bandwidth of the narrow probe pulses (violet errorbars). This shows the good agreement between the measurements and the calculated dispersion curve.

5 Description of Homodyne and Frequency-Resolved Detection of Light

In the previous chapter 4 the implementation of narrow bandwidth pulses enables the decoding of the underlying Raman processes in the scattering from probed phonon polaritons. The use of short pump pulses in the applied transient grating geometry results in a simultaneous excitation of the left- and right-propagating phonon polaritons. The subsequent scattering of the probe pulse leads to generation of Stokes and anti-Stokes components of the probe light field, which are superimposed on the detector. In this work a spectrometer is used to resolve the frequency of the light. In this chapter a mathematical treatment of the field components in the scattering and detection process is presented. This leads to an unambiguous interpretation of the dynamics of the measured transient intensity, which is influenced by the relative amplitudes of the Stokes, anti-Stokes and Rayleigh components of the detected light fields. The outline of this chapter is as follows: in section 5.1 the phase shift of the probe light during the scattering from phonon polaritons is derived. The next sections deal with special cases of the conditions under which the phonon polaritons are detected in the experiments: in particular the case of a negligible elastic Rayleigh contribution (5.2), a displaced probe region with respect to the excitation region (5.3), a detection with spectrally narrow probe pulse (5.4), and an increased elastic-scattered field contribution (5.5) are discussed. In section 5.6 the discussion of the additionally irradiated reference light field, the so-called local oscillator, is presented.

5.1 Phase Shift by the Scattering from Phonon Polaritons

The induced phase shifts of the probe light during the scattering from the phonon polaritons are considered in the following. Let us first assume, that all light fields are plane waves of the form $E = E_0 \exp(\mathrm{i}\omega t - \mathrm{i}\mathbf{k}\mathbf{r} + \mathrm{i}\phi_{0,\omega})$, where ω is the frequency of the laser light, $\mathbf{k}$ is the wave vector, E_0 is the amplitude and $\phi_{0,\omega}$ is the phase of the incoming light field. The relative phase of the spectral components $\Delta\phi_{i,j} = \phi_{0,\omega_i} - \phi_{0,\omega_j}$ is constant. Therefore, the phase $\phi_{0,\omega}$ factor is dropped. After the scattering process, the light field E_4 that is diffracted into the $\mathbf{k}_4$ direction is recorded with a spectrometer. Within the scope of this work the following three contributions to the scattered field E_4 are analyzed: E_+ stems from the anti-Stokes scattered light from the

right-propagating phonon polariton, E_- from the Stokes scattered light from the left-propagating phonon polariton and the elastically scattered field E_{el} is generated by the sample (e.g. from inhomogeneities, impurities or the surface). Since the spectrometer spectrally resolves only the detected light field, each pixel coherently adds up these three contributions:

$$E_4 = E_+ + E_- + E_{el} \ .$$
(5.1)

This is shown in figure 5.1 for one single and arbitrarily detected light frequency ω_4. The energy conservation rules relate the frequency ω_4 and the three incoming frequency components. The frequency $\omega_{3,el}$ of the elastically scattered field E_{el} remains unchanged. The field E_- with the initial frequency ω_{3-} is Stokes scattered from a phonon polariton with frequency ω_{pp} and the field E_+ with the frequency ω_{3+} is given by the anti-Stokes scattered process. Thus the following identity holds:

$$\omega_{3\pm} \pm \omega_{pp} = \omega_4 \text{ and } \omega_{3,el} = \omega_4 \ .$$
(5.2)

Obviously, only light fields with the exact same frequency ω_4 and wavevector magnitude k_4 can interfere on a single pixel of the spectrometer. It is important to note, that the frequency of the incoming light for all three contributions is different. Up to now, we discussed only the energy conservation during the scattering process and no dependence of the signal on the time-delay τ was considered. Now we investigate the propagation of phonon polaritons more thoroughly. The wave fronts of the polaritons propagate with velocity v_{pp}, which is almost equal to the speed of light in the medium, into the direction $\mathbf{q}_{R/L}$. When the pump pulse is delayed with respect to the probe pulse by the time τ the wave fronts advance in this time interval by $|r_\pm| = v_{pp}\tau = \omega_{pp}/q_{pp}\tau$ [88] into the directions of the polariton propagation $\mathbf{q}_{R/L}$. The scattering on a phonon polariton or impurities affects the incoming light field phases by adding a scattering phase $\phi_{4\pm}(\tau)$. The Stokes (-) and anti-Stokes (+) scattered field detected on a pixel of the spectrometer take the form

$$E_- = -iE_{-,0} \cdot e^{-\gamma\tau} \cdot e^{i[(\omega_{3-}-\omega_{pp})t+\phi_{4-}(\tau)]} = -iE_{-,0} \cdot e^{-\gamma\tau} \cdot e^{i(\omega_4 t+\phi_{4-}(\tau))}$$
(5.3)

$$E_+ = +iE_{+,0} \cdot e^{-\gamma\tau} \cdot e^{i[(\omega_{3+}+\omega_{pp})t+\phi_{4+}(\tau)]} = +iE_{+,0} \cdot e^{-\gamma\tau} \cdot e^{i(\omega_4 t+\phi_{4+}(\tau))}$$
(5.4)

$$E_{el} = E_{el,0} \cdot e^{i\omega_4 t}.$$
(5.5)

Here, $E_{+,0}$ and $E_{-,0}$ are the electric field amplitudes of the diffracted light which are connected to the incoming light amplitude E_0 via the scattering efficiency $\eta_\pm = E_{\pm,0}^2/E_0^2$. The factor $e^{-\gamma\tau}$
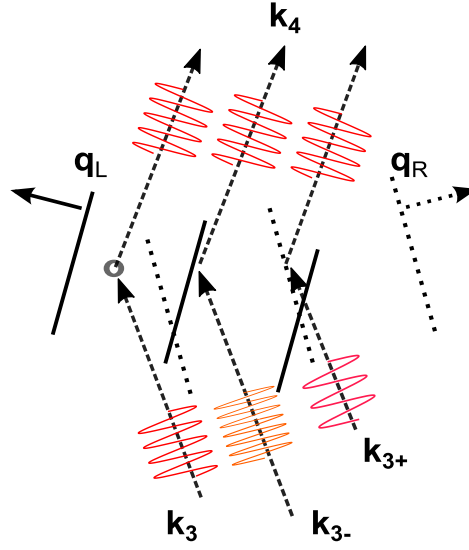
Figure 5.1: Visualization of three components of the light fields that contribute to the signal intensity on a single pixel of the spectrometer which detects the light along a fixed direction of $\mathbf{k}_4$. Incoming wave vectors along $\mathbf{k}_3$ have different magnitudes (wavelengths) $|\mathbf{k}_{3-}|$, $|\mathbf{k}_{3+}|$, and $|\mathbf{k}_3|$, respectively. In this case the light fields are scattered from a left-propagating polariton, a right-propagating polariton and from an impurity in the sample (open circle).

accounts for the damping of the phonon polaritons and the prefactor $\pm i$ determines the phase shift in Stokes and anti-Stokes scattering events [89]. $E_{el,0}$ is the amplitude of the elastically scattered light pointing into the direction $\mathbf{k}_4$. Due to the propagation of the phonon polaritons with respect to the probe pulse the phase of the scattered light evolves as

$$\phi_{4\pm}(\tau) = (\mathbf{r}_\pm \cdot \mathbf{k}_{3\pm} - \mathbf{r}_\pm \cdot \mathbf{k}_4) = \pm\omega_{pp}\tau \ , \tag{5.6}$$

where the right side of the equation is true because of the wavevector matching $(\mathbf{k}_4 - \mathbf{k}_{3+}) = \mathbf{q}_R$, $-(\mathbf{k}_4 - \mathbf{k}_{3-}) = \mathbf{q}_L$ and the phase velocity $v_{pp} = \omega_{pp}/q_{pp}$ of the polariton. The phase $\phi_{3,el}$ of the elastically scattered light is unaffected by τ. Now all three contributing light fields that contribute to the detected intensity I_{sig} are derived. In general, one pixel of the spectrometer detects

$$I_{sig} = |E_+ + E_- + E_{el}|^2 \ . \tag{5.7}$$

In the following, several special cases of the homodyne detection in the transient grating experiment which have been performed during this thesis are separately discussed.

5.2 Negligible Elastic Contribution

This is the case where all three beams perfectly overlap in the sample and the phonon polaritons are efficiently generated. Hence the inelastically scattered probe field is much larger than the elastic contribution, $E_{el} << E_{\pm}$. The intensity $I_{sig}^{(1)}$ is solely determined by the interference of the Stokes and anti-Stokes scattered light fields:

$$I_{sig}^{(1)} = |E_+ + E_-|^2 = E_{\pm 0}^2(2 + |e^{i\phi_{4+}(\tau)} - e^{i\phi_{4-}(\tau)}|^2) \cdot e^{-2\gamma\tau} \cdot |e^{i(\omega_4 t)}|^2 \quad . \tag{5.8}$$

In this situation, the detected intensity decays with twice the damping rate of the phonon polariton. The term, which oscillates with the detected light frequency ω_4, is a pure phase factor and the intensity measurement is independent of this contribution. A simple trigonometric transformation shows that the middle term gives rise to the oscillation of the signal with twice the polariton frequency:

$$I_{sig}^{(1)} = 2I_{\pm,0}(1 - \cos(2\omega_{pp}\tau)) \cdot e^{-2\gamma\tau} = 4I_{\pm,0}\sin^2(\omega_{pp}\tau) \cdot e^{-2\gamma\tau} \quad . \tag{5.9}$$

A typical measurement is presented in figure 5.2a. The data are well described using the expression for $I_{sig}^{(1)}$ from equation 5.9. The result of a calculation is shown by the (red line) in the same figure. The Fourier transform of the intensity (Fig. 5.2c, green line) shows a single peak, which appears at twice the phonon polariton frequency $\nu = 2\omega_{pp}/2\pi$.

5.3 Displaced Probe Region

If the probe pulse samples a region of the sample that can only be reached by one phonon polariton–let us assume for the following discussion that it is the left-propagating polariton–one may neglect the field E_+ which originates from the right-propagating polariton. For a larger wave vector the strong polariton damping leads to a rapid decrease of E_- and the amplitude of the Stokes scattered field becomes comparable to the elastically scattered light field amplitude: $E_- \approx E_{el}$. Thus, the detected intensity is dominated by the interference of the elastically and inelastically scattered fields. This is expressed by

$$I_{sig}^{(2)} = |E_- + E_{el}|^2 = |E_{-0}e^{-\gamma\tau + i\phi_{4-}(\tau) - i\pi/2} - E_{el,0}|^2 \cdot |e^{i(\omega_4 t)}|^2 \tag{5.10}$$

where again the phase factor $\omega_4 t$ is averaged out in the intensity measurement. The weak signal oscillates at the fundamental frequency ω_{pp} around an intensity level given by the elastically scattered light field $E_{el,0}$ and the inelastic scattering term which is damped with the rate 2γ:

$$I_{sig}^{(2)} = E_{el,0}^2 + E_{-0}^2 e^{-2\gamma\tau} + 2E_{el,0}E_{-0}e^{-\gamma\tau} \cdot \cos(-\omega_{pp}\tau - \pi/2) \tag{5.11}$$

$$I_{sig}^{(2)} = I_{el,0} + I_{-0}e^{-2\gamma\tau} - 2E_{el,0}E_{-0}e^{-\gamma\tau} \cdot \sin(\omega_{pp}\tau) \tag{5.12}$$

Unlike in the previously discussed case, the oscillation amplitude decays with the damping rate γ of the polariton. The relative intensities of the E_{el} and $E_{\pm}$ determine the oscillation amplitude. Several examples are closely discussed in section 6.1. It should be noted that the observed transient intensity which is explicitly shown in figure 6.1 is not properly described be the derived equation 5.12, because it do not consider any propagation effects or the effect of the exact overlap of the probe volume and the polariton wavepacket. To do so, additional terms have to be considered that describes the envelopes of the interacting fields. An approach can be found in reference [7].

5.4 Narrow Band Probe Pulses

For narrow band probe pulses the situation is different. The probe spectrum is so narrow that for all, except the smallest wave vector polaritons, the inelastically scattered probe pulses do either overlap with each other nor with the elastically scattered light. The intensity of the elastic scattered light E_{el} is hence much smaller and may be neglected. Moreover, the probe pulse is too long to be able to resolve the beating of the transient field. Since the two inelastic signal contributions E_+ and E_- are detected by separate pixels of the spectrometer, they do not give rise to interference features. Thus, the detector pixel monitors the intensity

$$I_{sig,\pm}^{(3)} = E_{\pm,0}^2 e^{-2\gamma\tau} |e^{i\omega_4 t}|^2 \cdot |e^{i\phi_{4\pm}}|^2 = I_{\pm0}e^{-2\gamma\tau}. \tag{5.13}$$

As can easily be seen, the intensity decays with twice the damping rate γ. An exemplary measurement is shown in figure 4.1 as the black solid line. The data that are observed with narrow bandwidth pulses with a temporal width of FWHM = 610 fs are compared to the convoluted data (orange line) obtained with short probe pulses (FWHM = 64 fs). Both data sets exhibit a decay with twice the phonon polariton damping rate, 2γ, according to equation 5.13 and 5.9, respectively. This is confirmed by the Fourier analysis, which is shown by the red solid line in figure 4.1b.

5.5 Increased Elastic Field Contribution

This is a more unusual experimental condition. All three beams perfectly overlap in the sample, however, the polaritons are either inefficiently generated or the sample shows an increase of the elastically scattering contribution of the probe field E_{el} that is for example caused by sample impurities or other defects. A significant elastic scattering holds for samples with a simultaneously

excited thermal grating as was previously reported [80, 90]. Here, the elastic contribution is assumed to have the same field magnitude as the field diffracted by the phonon polaritons, $E_{el} \approx E_{\pm}$. Then equation 5.7 has to be evaluated completely (the full calculation is presented in appendix A.1), which leads to the result

$$I_{sig}^{(4)} = I_{el,0} + (I_{+,0} + I_{-,0})e^{-2\gamma\tau} + 2I_{\pm}e^{-2\gamma\tau}\cos(2\omega_{pp}\tau + \pi) + 2(I_{el,-} + I_{el,+})e^{-\gamma\tau}\cos(\omega_{pp}\tau + \pi/2).$$
(5.14)

The signal consists of a constant background contribution $I_{el,0}$, non-oscillating terms $I_{+,0}$ and $I_{-,0}$, which decay with 2γ, a term that oscillates with twice the polariton frequency and a decay of the amplitude of 2γ, and the third term oscillating at the fundamental polariton frequency ω_{pp} with the damping rate γ. For the case $I_{+,0} \approx I_{-,0}$ equation 5.14 simplifies to

$$I_{sig}^{(4)} = I_{el,0} - 4I_{el,\pm}e^{-\gamma\tau}\sin(\omega_{pp}\tau) + 4 \cdot I_{\pm}e^{-2\gamma\tau}\sin^2(\omega_{pp}\tau) \ .$$
(5.15)

The behavior of the transient intensity $I_{sig}^{(4)}$ is characterized by the "superposition" of sine and sine-squared functions. In the following, an exemplary measurement is presented, where the condition of increased elastic field contribution was deliberately prepared. In figure 5.2a the transient intensity trace, which was obtained from counter propagating phonon polaritons with the wavevector magnitude $q = 790$ cm^{-1} , is shown by the green line. The pump and probe regions overlap as sketched in figure 5.2d. The measured data are integrated over the wave-lengths range between 794 nm and 795 nm. The integration is done for a better statistics. The intensity ratio of the pump and probe beams is $I_{pump}/I_{probe} = 7/3$. In this case the contribution to the signal from the elastically scattered light due to the inhomogeneities is negligible. The simulation (red line) according to equation 5.9 fits very well to the data. The Fourier transform is depicted in figure 5.2c. The power spectrum (green line) indicates a single frequency of $\nu = 1.66$ THz corresponding to twice the polariton frequency $2 \cdot \nu_{pp} = 2 \cdot 0.83$ THz.

Now, the intensity of the pump and probe beams is inverted and the ratio amounts to $I_{pump}/I_{probe} = 3/7$. The transient ISRS intensity shown by the blue line in figure 5.2b shows a pronounced beating, which is caused by the "superposition" of sine and sine-squared functions in equation 5.15. The Fourier spectrum (blue line in figure 5.2c) indicates two distinct frequencies. Again, one frequency is centered at $\nu = 1.66$ THz. Note, this peak has exactly the same width (FWHM=0.07 THz) as previously one (green line). The second frequency amounts to 0.83 THZ, which is half of the first value.

The calculation of transient intensity in figure 5.2b is performed using equation 5.14 that accounts for the elastically scattered light field. The magenta line shows the result of the fitting to the data points. The agreement between the measurement and the fit is very good. The experiment, where the pump and probe beam intensities were exchanged, can be explained in
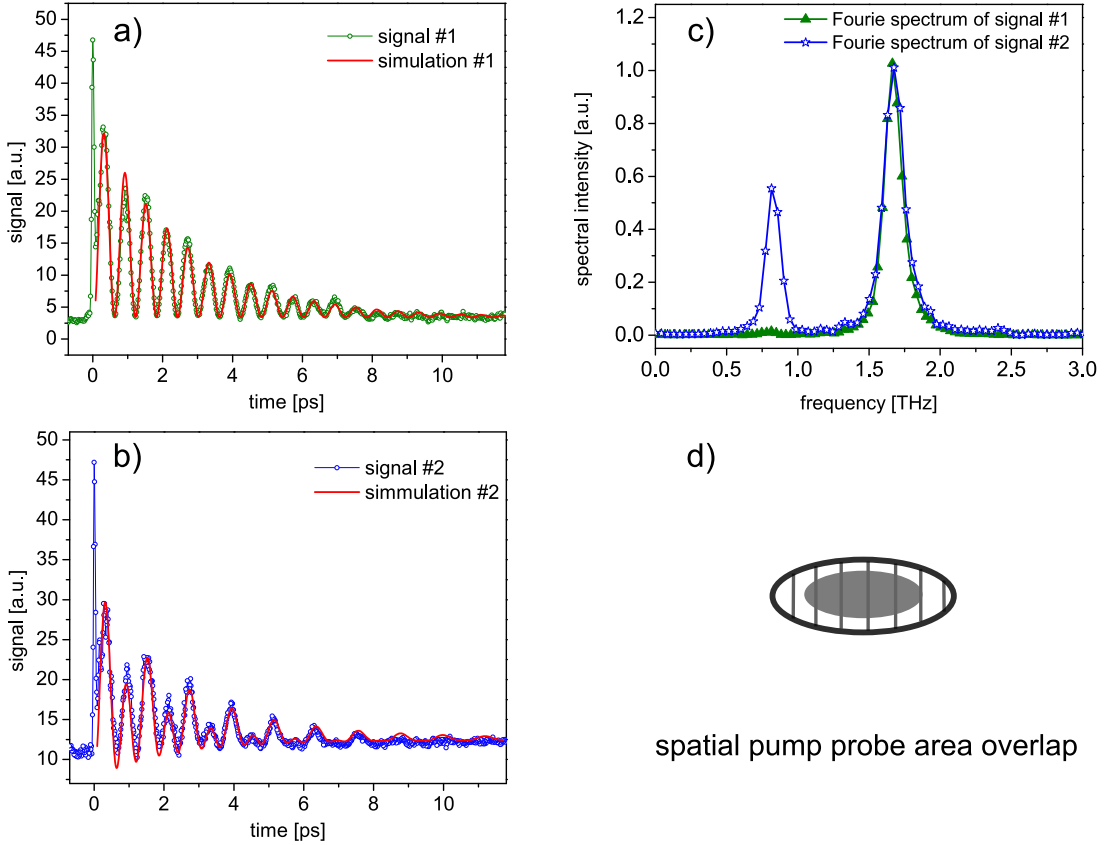
Figure 5.2: Transient intensity diffracted from the phonon polaritons with a wavevector magnitude of $q = 790 \ \text{cm}^{-1}$ measured with short probe pulses. The data are integrated over the wave-length range between 794 nm and 795 nm. a) Intensity ratio of the pump and probe beams is $I_{pump}/I_{probe} = 14/3$. The signal (green line) is simulated (red line) using equation 5.9. b) The role of the pump and probe beam is switched and the intensity ratio of the pump and probe beams is now $I_{pump}/I_{probe} = 6/7$. The intensity (blue line) is simulated (magenta line) according to equation 5.14. c) Fourier spectrum of the data displayed in a) and b). d) Sketch of the pump and probe overlap region.

the following way: the excitation efficiency of the polaritons is reduced because the intensity of the pump beams is diminished by a factor of 2.3. This leads to a respective decrease of the Raman scattered light. Simultaneously, the elastically scattered light is increased due to the higher intensity (by the same factor 2.3) of the probe light impinging on the sample. All three contributions, the Stokes field, the anti-Stokes field, and the elastically scattered field are mixed. Thus, the signal shows a single and the double frequency ν_{pp} and $2\nu_{pp}$, respectively. This treatment fully agrees with the mathematical description given by equation 5.14. One additional measurement where one has to consider the increased elastic field contribution is shown in figure 5.3a. Two counter propagating phonon polaritons with a wave vector magnitude of $q = 1730 \ \text{cm}^{-1}$ are impulsively excited. The probe beam perfectly overlaps with the excitation
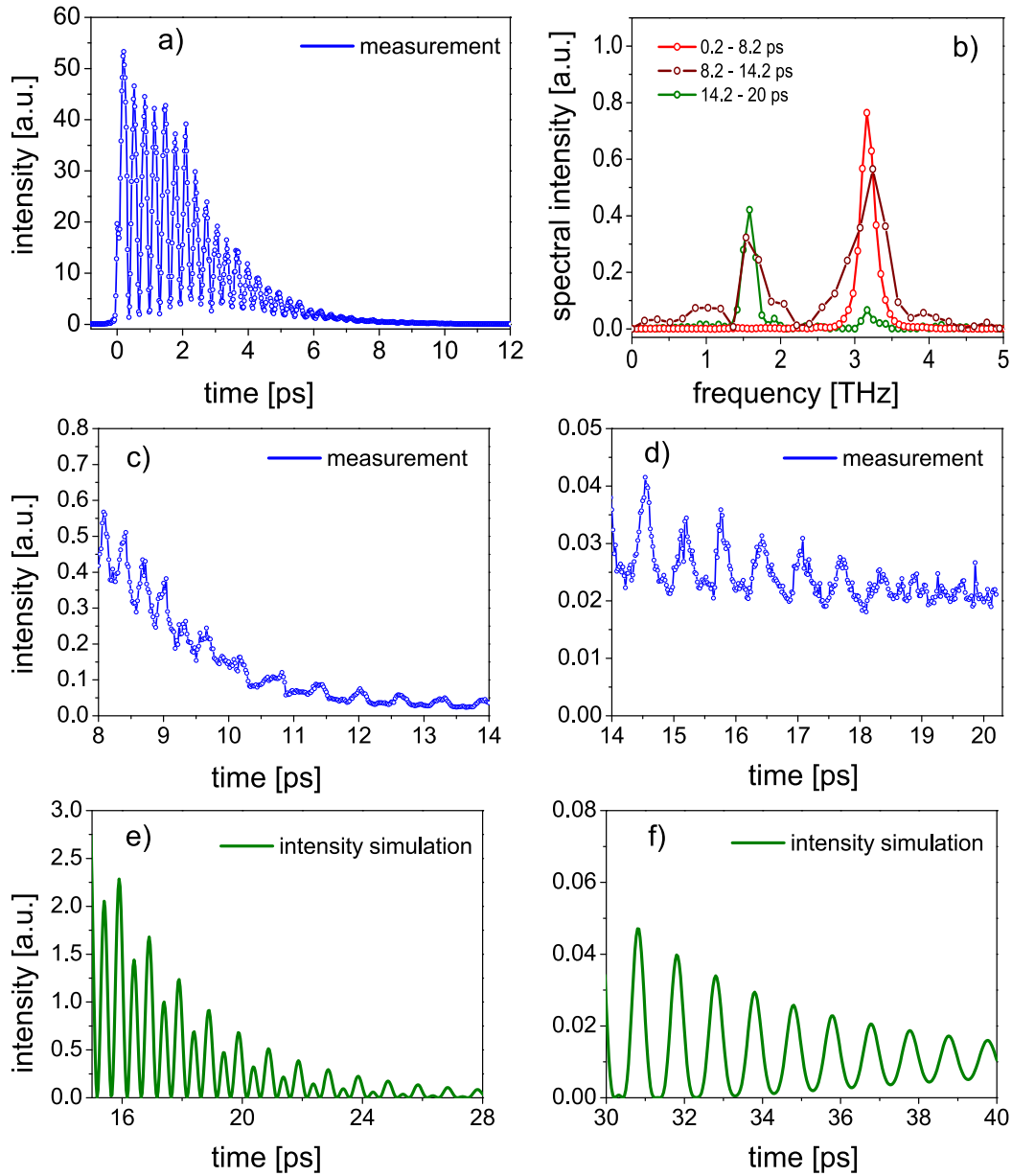
Figure 5.3: Transient intensity diffracted from the phonon polaritons with a wave vector magnitude of $q = 1730$ cm^{-1}. The measurements are performed with short probe pulses (~ 64 fs) and a perfect pump probe overlap. The data are integrated over the wavelength range between 798 nm and 802 nm. a), c) and d) show different time-windows of the same measurement. b) Corresponding Fourier spectrum of the three time-windows that exhibit a single frequency $\nu = 3.16$ THz for the early times shown in a), two frequencies $\nu = 3.16$ THz and $\nu = 1.58$ THz for the transition regime shown in c), and a pronounced single peak at $\nu = 1.58$ THz for long times shown by d). e) and f) Simulation of the diffracted intensity where three contributing fields are considered: Stokes scattered E_-, anti-Stokes scattered E_+, and the elastic field E_{el}. The ratio of the field magnitudes is set to $E_- = E_+ = E_{el}/100$.

area in the sample. Its intensity amounts to 3/7 of the pump beam. The transient intensity is monitored for up to 20 ps after the excitation. As shown in figure 5.3a the intensity oscillates for the first 8 ps with twice the frequency of the phonon polaritons, that is $\nu = 2\nu_{pp} = 3.16$ THz as is analyzed by the FFT, which is depicted in figure 5.3b by the red line. This is in agreement with equation 5.9.

Further, the scattered intensity decays due to propagation and damping effects of two counter propagating phonon polaritons. For large time-delays, this leads to the condition where the initially amplitude of the inelastically scattered light becomes of the order of elastic field amplitude E_{el}. The data in figure 5.3d are recorded for time-delays larger than 14 ps. They exhibit an oscillation with a single frequency $\nu_{pp} = 1.58$ THz. The green line in figure 5.3b shows the FFT analysis of this time-window. In this case equation 5.14 that includes the contribution of elastically scattered light has to be applied to appropriately describe the data.

In the intermediate time-range the transition from one regime to the next occurs. This is shown in figure 5.3c and the corresponding Fourier transform of this time-window is plotted in figure 5.3b by the brown line. Two peaks centered at $\nu_{pp} = 1.58$ THz and $\nu = 3.16$ THz appears in the Fourier spectrum, which clearly indicate the occurrence of the fundamental and double frequency ν_{pp} of probed phonon polaritons.

A simulation of the transient signal is depicted in figures 5.3d and 5.3e. The intensity given by equation 5.7 is calculated under the assumption that three fields incident on the same pixel of the monochromator: Stokes scattered E_-, anti-Stokes scattered E_+, and the elastic field contribution E_{el}. The ratio of the field magnitudes is set to $E_- = E_+ = E_{el}/100$. Indeed, one first observes an oscillation of the intensity I_{sig} with twice the frequency (not shown here), which is followed by the intermediate regime (see figure 5.3d), where the transition occurs. For later times that are shown in figure 5.3e I_{sig} oscillates with the fundamental frequency. In reality, the analysis of the transient diffracted intensity with a Fourier transform usually reveals a frequency spectrum with a pronounced peak at twice the phonon polariton frequency $2\nu_{pp}$ and an additional peak at the single frequency ν_{pp}, which is barely recognizable.

5.6 Homodyne Detection with a Local Oscillator Field

In figure 5.4 a situation is visualized where a second probe pulse $\mathbf{k}_4$ simultaneously illuminates the sample. This is transmitted and subsequently detected by the spectrometer together with the Raman scattered light fields from the phonon polaritons. This additional field acts as a so-called local oscillator. The intensity on a single pixel of the spectrometer is similar to the one given by
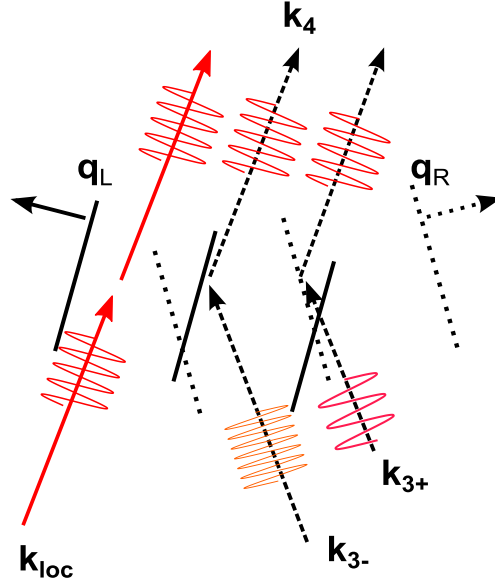
Figure 5.4: Visualization of the homodyne detection using a local oscillator field incident that points into the $\mathbf{k}_{loc} = \mathbf{k}_4$ direction. Three components of the light fields, which contribute to the measured signal on a certain pixel of the spectrometer that detects the light along the fixed direction of $\mathbf{k}_4$ are shown: the light fields are scattered from both, the left-propagating and the right-propagating polariton. The local oscillator field is transmitted through the sample.

equation 5.16, except that the local oscillator field E_{loc} substitutes the elastically scattered field E_{el}. The modified equation 5.16 then reads:

$$I_{sig}^{(6)} = |E_+ + E_- + E_{loc}|^2 \tag{5.16}$$

with $E_{loc} = E_{loc,0} \cdot e^{i\omega_4 t}$. The evaluation of this equation gives the following expression for the detected intensity:

$$I_{sig}^{(6)} = (I_{+0}+I_{-0})e^{-2\gamma\tau}+I_{loc,0}+2I_{\pm0}\sin^2(\omega_{pp}\tau)\cdot e^{-2\gamma\tau}+2(E_{+0}E_{loc,0}+E_{-0}E_{loc,0})\cos(\omega_{pp}\tau+\pi/2)e^{-\gamma\tau} \ . \tag{5.17}$$

This is the same formula as already obtained for case of an increased elastic field contribution in section 5.5, equation 5.14. In the present case, the amplitude E_{loc} of the local oscillator field can be adjusted. Generally, the field E_{loc} is much higher than Raman scattered fields $E_{\pm0}$ and thus the expression 5.17 can be simplified to

$$I_{sig}^{(6)} = I_{loc,0} + 2E_{\pm0}E_{loc,0}\cos(\omega_{pp}\tau)e^{-\gamma\tau}, \tag{5.18}$$

under the assumption, that the Stokes and anti-Stokes scattered fields are of the same amplitude $E_{\pm0} = E_{+0} = E_{-0}$. The observed transient intensity $I_{sig}^{(6)}$ is modulated with the single polariton
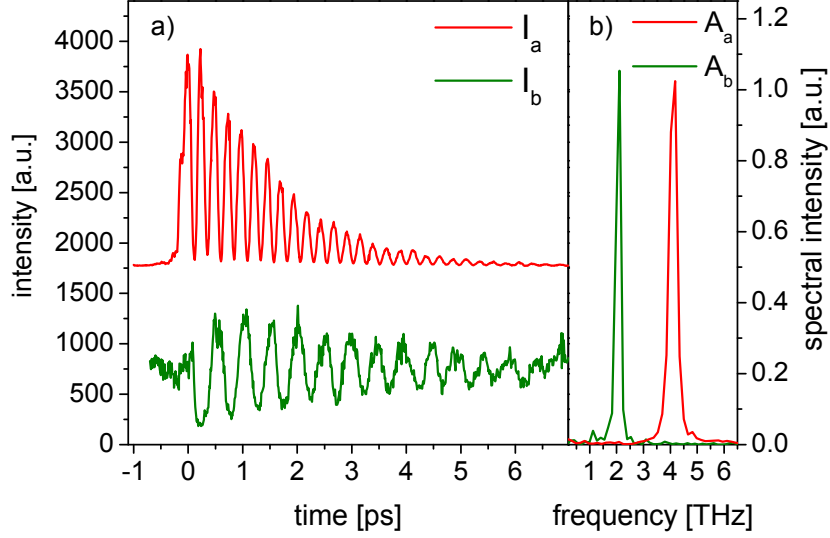
Figure 5.5: Transient homodyne detection of probe light diffracted from the phonon polaritons with the use of a local oscillator field. The wavevector of the phonon polaritons is set to $q = 2300$ cm^{-1}. The probe pulses are temporally short (~ 64 fs). a) Integrated ISRS intensity without (red line) and with (green line) the local oscillator field $I_{loc,0}$ simultaneously impinging on the spectrometer. b) Fourier analysis of the transient intensity determines the oscillation frequency to 4.1 THz (red line) and 2.05 THz (green line) as predicted by equation 5.9 and 5.18, respectively.

frequency ω_{pp} and oscillates around the constant amplitude $I_{loc,0}$. Its damping rate is γ. An example is shown by the green line in the left panel of figure 5.5. The transient intensity oscillates around the value of the intensity of the local oscillator $I_{loc,0}$. The Fourier analysis is shown by the green line in the right panel of the same figure. It indicates a single phonon polariton frequency $\nu_{pp} = 2.05$ THz, which is expected from the dispersion relation for the polariton wavevector $q = 2300$ cm^{-1}. The damping rate amounts to 0.055 THz. The measurement is compared to the data (red line in the left panel) which are recorded in the usual manner of an ISRS experiment, without the local oscillator field. The transient intensity oscillates with twice the polariton frequency $2\nu_{pp} = 4.1$, as is evident from the Fourier analysis shown in the right panel of the figure 5.5. In this case, the damping rate amounts to 0.1 THz. Both confirm the prediction of the equation 5.18.

6 Propagation of Phonon Polariton Wavepackets

For small frequency values the phonon polaritons are light-like, exhibit small damping and propagate with light like speeds through the medium. Several groups report the detection of coherent phonon polariton wavepackets after they propagated a distance of up to several centimeters in the sample [91]. Sophisticated experiments demonstrate the wave-character of the phonon polaritons: the propagation of polaritons in patterned materials [92], the interference and diffraction effects in classical diffraction geometries [93], reflection [94,95] and partial transmission at the side surface of the sample [96], and guidance behavior in thin slab samples [97]. The low-frequency properties of phonon polaritons enable the development of compact, integrated THz spectroscopy cells with optical input and output pulses and no THz propagation in air [53,92,98].

The focus of this chapter lies on the propagating polariton wavepackets which are examined using a slightly displaced probe region with respect to the excitation spot. The advantages of temporally short and narrow bandwidth probe pulses are discussed in section 6.1 and 6.2, respectively. The experiment with short probe pulses reveals that the oscillation of the transient intensity only appears if the Raman scattered light is superimposed with the elastically scattered light field from the sample. The experiment with narrow bandwidth probe pulses unambiguously clarifies that the probe beam is Stokes and anti-Stokes scattered from the same polariton wavepacket simultaneously. Moreover, the position of the detector allows selecting the propagation direction of the examined polaritons.

6.1 Observation with temporally short Pulses

The pump pulses were aligned in order to excite phonon polaritons with a relatively small wavevector magnitude of q = 1050 cm^{-1} and hence with a small damping. The low damping ensures that the phonon polaritons exhibit a large propagation distance until it finally reaches the displaced observation volume. The size of the excitation spot is 70x800 μm^2. Figures 6.1b and 6.1c show the spectrally integrated transient intensities for two exemplary cases of displaced probe regions. The corresponding Fourier transforms are shown in figures 6.1e and 6.1f. In comparison, figure 6.1a shows the spectrally integrated transient ISRS data where the pump

and probe pulses spatially overlap. The scattered intensity $I(\tau)$ oscillates at $2\omega_{pp} = 2.2$ THz and is damped with 2γ. $I(\tau)$ consists here of a superposition of the Stokes and anti-Stokes light scattered from both counter-propagating polaritons as discussed in section 5.2. The contribution of the elastically scattered light from the sample is negligible. The ratio of the signal maxima and the background is determined to $I_{max}/I_{el} \approx 400$. The signal decays essentially due to the intrinsic damping of phonon polaritons in the medium.
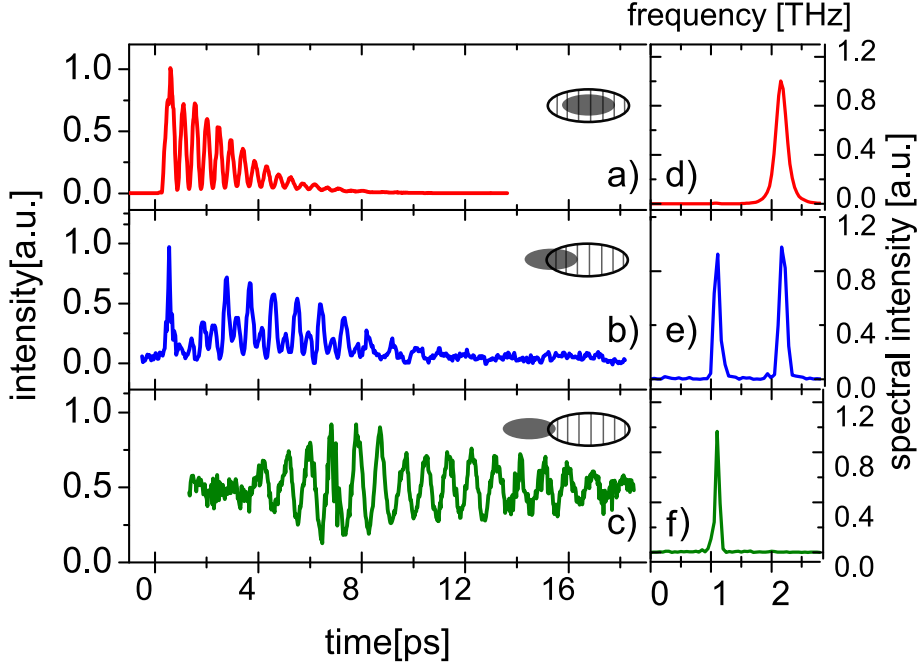

Figure 6.1: Spectrally integrated transient ISRS signals from $LiNbO_3$ obtained with short probe pulses. The excited wavevector magnitude of the phonon polariton is $q = 1050$ cm^{-1}: a) using the standard boxcar configuration where the probe beam perfectly spatially overlaps with the pump beam, b) with a 350 μm to the left side of the excitation area displaced probe spot, and c) using a 750 μm to the left side of the excitation spot displaced probe spot. (d-f) The corresponding Fourier transformations of the transient ISRS intensities a-c.

Now the probe area is displaced by 750 μm to the left and is essentially separated from the excitation region (see figure 6.1c). The scattered intensity $I(\tau)$ is modulated at the fundamental polariton frequency $\omega_{pp} = 1.1$ THz and decays with the damping rate γ. Obviously, only the left-propagating polariton wave packet enters the observation region. Now the inelastically scattered light is superimposed with the elastically scattered light from defects and impurities in the sample. The ratio of the intensity maximum and the background for $\tau < 0$ is $I_{max}/I_{el} \approx 2$. The transient intensity can be well described by equation 5.12.

In the intermediate regime shown in figure 6.1b where the probe is only displaced by 350 μm from the excitation center, the intensity level is still low with $I_{max}/I_{el} = 2.5$. Both frequencies

ω_{pp} and $2\omega_{pp}$ are observed. This is attributed to the left-propagating phonon polariton moving through the observation spot whereas the right-propagating polariton leaves this region. Note again, the leading peak in the ISRS trace that is shown in figure 6.1b is due to the pure electronic, third-order nonlinearity of the sample. The observation of the phonon polaritons with a displaced probe region is sensitive to the envelope of the polariton wave packet. In figure 6.1b and especially in figure 6.1c one can clearly see the slow rise and drop of the intensity as the polariton is passing through the probe volume. The simulation of such signals has to account for the time-dependent overlap of the probe beam with the polariton wave packets [7].

6.2 Identification of the Propagation Direction: Observation with Narrow Band Pulses

In order to unambiguously identify the propagation direction of the phonon polaritons, the discussed experiment in previous section 6.1 is repeated using spectrally narrowed probe pulses. The probe beam is spatially displaced to the left by 500 μm, as schematically indicated in subfigure 6.2a. For a low damping of the phonon polariton and hence a longer propagation length, a smaller wavevector magnitude of $q = 700$ cm^{-1} is chosen. In addition, the probed region is minimized using a knife-edge which blocks the portion of the probe pulse that overlaps with the pump region. In this experiment, only the left-propagating polariton q_L is probed. In figure 6.2b, the vector diagram applicable for this measurement is shown. The probe pulse enters along $\mathbf{k}_{3,in}$ and the detector is placed in the $\mathbf{k}_{4,out}$ direction.

Only the Stokes scattering accompanied by the creation of an additional polariton $\mathbf{q}_L$ is allowed, as evidenced from the contour plot 6.2e. In fact, the plots in figure 6.2g show that immediately after pumping at $\tau \approx 3$ ps there still are small contributions of an anti-Stokes scattering from the right-propagating polariton $\mathbf{q}_R$ (black line). However, the spectrum for $\tau > 3$ ps exclusively shows Stokes scattering from the left-propagating polariton $\mathbf{q}_L$.

The time-dependence of the Stokes (red) and anti-Stokes (blue) intensities depicted in figure 6.2d shows a sharp rise at $\tau = 0$ ps of both signals. The time resolution is given by the probe pulse duration. The blue signal associated with the right-propagating polariton, $\mathbf{q}_R$, immediately fades out due to the direction of the propagation. In contrast, the red signal keeps rising as the polariton $\mathbf{q}_L$ moves more and more into the probe region. Finally it decays due to the damping.

To verify that Stokes and anti-Stokes scattering can clearly distinguish between q_R and q_L, the roles of $\mathbf{k}_3$ and $\mathbf{k}_4$ are exchanged as sketched in figure 6.2c. Now, only $\mathbf{k}_{4,in}$ impinges on the same position of the sample. The spectrometer is now placed in the $\mathbf{k}_{3,out}$ direction. In this case only anti-Stokes scattering due to the annihilation of a left-propagating polariton $\mathbf{q}_L$ is detected. The transient spectrum in figure 6.2f clearly confirms this.
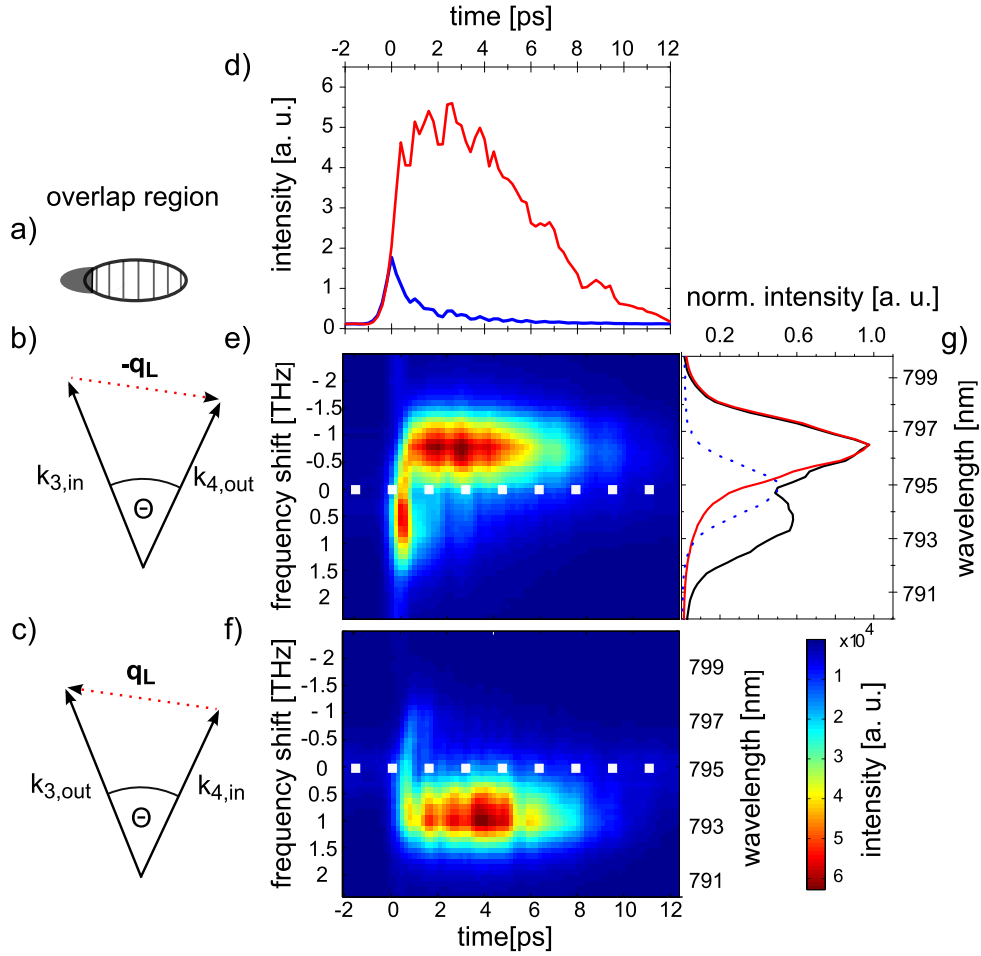
Figure 6.2: Detection of the left-propagating phonon polariton with the wavevector magnitude $q = 700$ cm^{-1}. a) The probe spot is displaced by 500 μm and is spatially cut in order to prevent the overlap of the pump and probe areas. b) Wavevector diagram for the case of Stokes scattering from $\mathbf{q}_L$ when $\mathbf{k}_{3,in}$ is the incoming probe light and the spectrometer detects the light along $\mathbf{k}_{4,out}$. c) Wavevector diagram for the anti-Stokes scattering with incoming light along $\mathbf{k}_{4,in}$ and detection along $\mathbf{k}_{3,out}$. e,f) Transient Stokes (anti-Stokes) intensity indicates the creation (annihilation) of the left-(right-) propagating phonon polariton. d) Transients of the intensities corresponding to the Stokes (red line) and anti-Stokes (blue line) scattered light. The transients are determined from the data set shown in e) by integrating over the wavelengths around $\lambda = 797$ nm and $\lambda = 793$ nm, respectively. g) Light spectrum around $\tau = 0$ ps (black line) and for later times (3.8 ps - 7.8 ps) (red line). The blue dotted line is the spectrum of the incident probe pulse.

7 Energy-Selective Excitation of Phonon Polaritons

Up to now, the selectivity in the excitation of the polariton modes was restricted by the conservation of momentum $|\Delta\mathbf{k}| = q_{R/L}$. The intersection angle Θ of the two pump pulses in the transient grating geometry determines which mode is excited. The conservation of energy $\omega_{pp} = |\omega_1 - \omega_2|$ was less restrictive. This relation requires the two mixed frequencies ω_1 and ω_1 to lie within the spectrum of the broad pump pulses. In our case the width amounts to FWHM $\approx$ 13 THz. Moreover, if the pulse duration of the exciting laser is shorter than the oscillation period of the driven lattice mode, $\tau_{pulse} < \tau_{vib}$, the excitation is called impulsive. Because both pump pulses are spectrally identical, two equal counter propagating phonon polaritons with a well-defined wavevector magnitude and frequency were simultaneously generated. However, if both pulses do not have the same spectrum and if for example the frequency ω_1 is always larger than ω_2, then only phonon polaritons that fulfill the condition $\omega_{pp} = \omega_1 - \omega_2$ will be generated. Now, in addition to the wavevector selectivity $|\Delta\mathbf{k}| = q_{R/L}$ the frequency of the excited phonon polariton mode can be selected through variation of the energies ω_1 and ω_2.

In this chapter, the spectra of both pump pulses, $\mathbf{k}_1$ and $\mathbf{k}_2$, are modified in order to generate polaritons which propagate with a well-defined energy into only one direction, as is explained in section 7.1. In section 7.2 an experiment is discussed where modes that have the same wavevector but a different energy are selectively enhanced.

7.1 Selective Preparation of a Phonon Polariton Wavepacket Component

In this section phonon polaritons with the direction q_R are selectively prepared. To highlight the difference to the wavevector-selective excitation with two spectrally identical pump pulses, which leads to generation of two counter propagating phonon polaritons, first a brief recall of the experiment with short laser pulses and narrow bandwidth probe pulses follows: the incident pump pulses $\mathbf{k}_1$ and $\mathbf{k}_2$ have an identical spectrum, which is shown in figure 7.1b by the black solid line. In this example, a wavevector of the phonon polariton $q = 17450$ cm^{-1} is excited, whereby the right- and left-propagating phonon polariton is equally likely generated by the

Stokes scattering process, as depicted in figure 7.1a. A probe pulse with a bandwidth of 2 nm is incident along the $\mathbf{k}_3$ direction. The pump and probe volumes coincide (see the schematic inset of figure 7.1b). The probe light undergoes Stokes scattering from the right-propagating polariton and anti-Stokes scattering from the left-propagating polariton. The diffracted light is detected along $\mathbf{k}_4$, as explained in the wavevector diagram in figure 7.1d.

Figure 7.1e is the spectrally resolved intensity trace. For time-delays around 0.5 ps, the transient spectrum is extracted for further analysis (green line in Fig.7.1f). Stokes and anti-Stokes lines quantify a frequency shift of $\Delta\omega = \omega_{pp} = 6.7$ (6.6) THz which indicates the creation and annihilation of $\mathbf{q}_L$ and $\mathbf{q}_R$.

Next, the spectrum of the pump laser pulses, $\mathbf{k}_1$ and $\mathbf{k}_2$, is modified by inserting appropriate bandpass filters into each pump beam path separately (see Fig. 3.2). The spectra of $\mathbf{k}_1$ and $\mathbf{k}_2$ are now centered at 795 nm and 810 nm as shown in figure 7.1b by the blue and red lines, respectively. This corresponds to a frequency separation of $\Delta\omega = 6.5 \pm 2.5$ THz which matches the frequency of the previously excited phonon polariton. Note, in this experiment, the angle between the pump beams is kept unchanged.

Again, one expects the creation of phonon polaritons via the Stokes scattering process. Because $|\mathbf{k}_2| < |\mathbf{k}_1|$, only the right-propagating phonon polariton can be excited as depicted in the wavevector diagram 7.1c. Note, that the bandwidths of the excitation pulses (≈ 4 THz) are smaller than the frequency $\omega_{pp} = 6.7 \pm 0.2$ THz of the phonon polariton. Thus, the excitation process is no longer impulsive. It is a stimulated Raman scattering process.

It should be noted that all conditions of the probe pulse remain as previously explained. Figure 7.1g depicts the wavevector diagram which applies for this case. The frequency-resolved intensity trace (Fig.: 7.1h) clearly indicates that only Stokes scattered probe light from the right-propagating polariton q_R is detected. For time-delays around 0.5 ps, the detected spectrum is shown in Fig. 7.1f. After rescaling the intensity, both Stokes intensities can be compared. It is evident that the Stokes peaks (green and brown lines) coincide in their peak positions and their shapes. This suggests that the same phonon polariton modes are excited either by the laser pulse with the full and broad spectrum or by selective spectrally narrowed pulses. Furthermore, it is obvious that one can selectively excite a phonon polariton with a well-defined propagation direction and wavevector magnitude just by controlling the incident spectral components of the excitation pulses and the intersection angle.

Next, the relative amplitudes of the electric fields of the excited phonon polaritons and the efficiency of the generation processes of the phonon polaritons are estimated. In figure 7.2 the spectrally integrated transient anti-Stokes intensity of light which undergoes Raman scattering from right propagating phonon polariton is shown. In the case of I_1, the polariton is excited using broad bandwidth pulses (FWHM$\sim$ 30 nm) and in the case of I_2 spectrally narrow pump
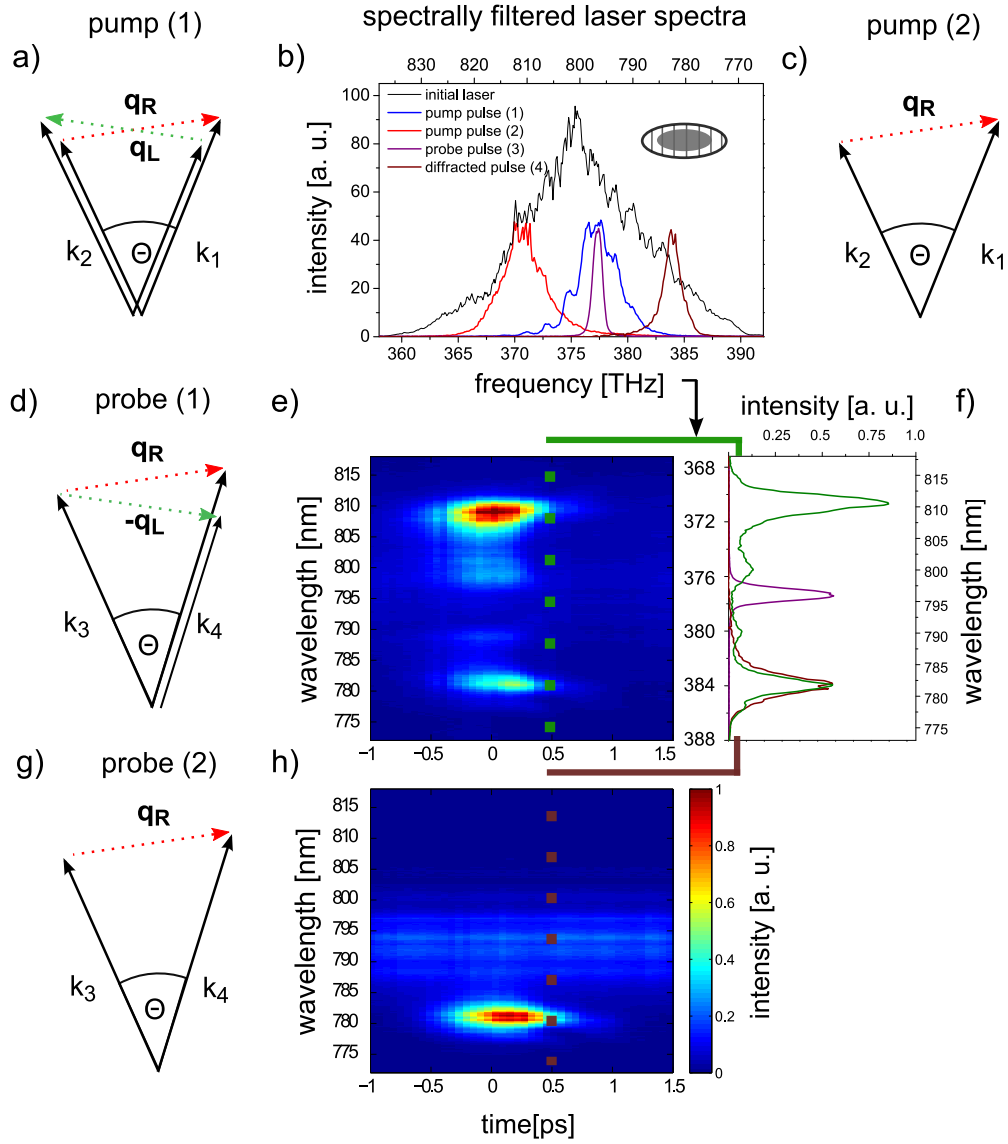
Figure 7.1: Selective preparation of right-propagating phonon polariton (PP) with $q = 17450$ cm^{-1}. a) Wavevector diagram for the excitation of the left- and right-propagating PP by stimulated Stokes scattering. b) Spectra of incident laser pulses prepared by the inserted bandpass filters: initial pump laser pulse(s) (black), pump pulse centered at 795 nm (blue), seed pulse centered at 810 nm (red), probe pulse at 795 nm (purple), and the diffracted probe pulse (brown) appears at 781 nm. Inset: The overlap of pump (dark grating) and probe (gray area). c) Wavevector diagram for the excitation of only right-propagating PP by stimulated Stokes scattering. d) and g) Wavevector diagram for the probe of generated PPs. e) Transient Stokes and anti-Stokes intensity indicating the creation and annihilation of left- and right-propagating PPs. h) The transient anti-Stokes intensity indicates the exclusive preparation of right-propagating PP. f) Light spectra at $\tau = 0.5$ ps as obtained from (e) and (h). Spectra of the incident probe pulse is shown by the violet line.
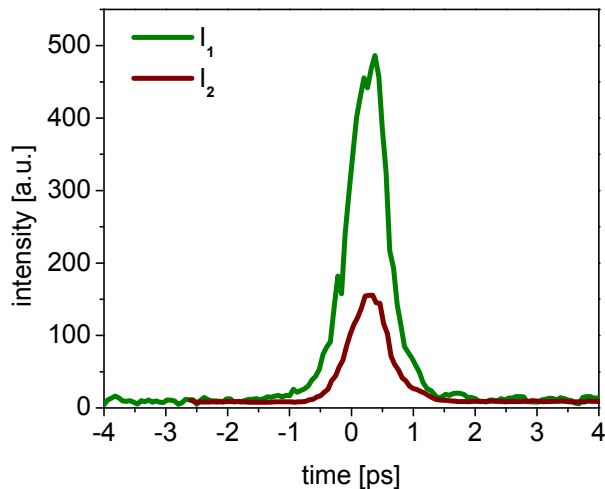
Figure 7.2: Spectrally integrated anti-Stokes intensity as function of the time-delay as obtained from the measurements shown in figures 7.1e (I_1–excitation with full bandwidth pulses) and 7.1h (I_2–excitation with narrow bandwidth pulses). The integration is performed between 777 nm and 784 nm in both cases. The ratio of the peak intensities amounts to 1:3.

pulses (FWHM∼ 10 nm) are used for the selective excitation of the right propagating polariton. In both experiments the probe pulse intensity was the same. The ratio of the peak intensities amounts to 1:3.

We can estimate the relative field amplitude E_{pp} of the polariton under the assumption that the diffracted intensities I_1 and I_2 are proportional to the square of the polariton field amplitude $E_{pp,1(2)}^2 \sim I_{1(2)}$. For the case of narrow bandwidth excitation, the intensity ratio, $I_2/I_1 = 1/3$, reveals a relative field amplitude of 57%. Alternatively, the relative generation efficiency η_{gen} can be estimated from the spectral content of the broad and narrow bandwidth pulses, too. The bandwidth of the spectra is 30 nm and 10 nm, respectively. The bandpass filters cut out a Gaussian spectral profile with a transmission efficiency of 90% of the initial intensity. Thus, the additive intensity of the narrow pulses is reduced to 43%. This reduction of the spectra of the excitation pulses will lead to a reduced efficiency in the excitation process of phonon polaritons. Because the polariton field amplitude E_{pp} is proportional to the product of the pump fields $E_{pp} \sim E_1 E_2 \approx I_{pump}$, the generated polariton field using pulses with a bandwidth of 10 nm will be reduced to 43%, too. Obviously, this value is lower than the one obtained from the experiment here (57%). The difference of the estimated values is due to fact, that not all spectral components of the initial broad bandwidth pulses contribute equally to the generation process of phonon polaritons. Indeed, the narrow bandwidth pulses are selected for an effective excitation of the phonon polaritons with a frequency of $\omega_{pp} = 6.7$ THz.

7.2 Selective Excitation of higher Phonon Polariton Modes

Here, I discuss experiments where two bandpass filters are used to cut out two different spectral components of the pump pulses. Because both pump pulses are derived from the same laser and both spectra almost do not overlap, the duration of the pump pulses is not shorter than the oscillation period of the driven vibration. The excitation is now non-impulsive, but still a stimulated Raman process. The spectra of the pump laser pulses $\mathbf{k}_1$ and $\mathbf{k}_2$ with their center wavelength of 795 nm and 810 nm, which corresponds to $\Delta\omega = 6.5 \pm 2.5$ THz, are shown in figure 7.1b by the blue and red lines, respectively. Here $\mathbf{k}_1 > \mathbf{k}_2$, therefore only the right-propagating phonon polaritons q_R in $LiNbO_3$ are excited as is depicted in figure 7.1c. Further, the narrow bandwidth probe pulses are used to detect the generated phonon polaritons. The pump and probe regions overlap. The probe pulses are incident and scatter along the $\mathbf{k}_3$ and $\mathbf{k}_4$ direction, respectively. The spectrometer detects only the pulses in the $\mathbf{k}_4$ direction. The conservation of momentum, which applies in this case, is shown in figure 7.1g.

Different normalized anti-Stokes spectra are displayed in figure 7.3. The intersection point with the right y-axis corresponds to the wavevector magnitude, q, of the probed phonon polariton from the lowest dispersion branch. The purple open circles indicate the peak position of the spectrum, as obtained from the fitting analysis. The data confirm the theoretical dispersion relation that is also plotted as a grey dashed line in the same figure. In the spectra for the wavevector magnitude $q = 3920$ cm^{-1} (green line), 6280 cm^{-1} (red line) and 8360 cm^{-1} (cyan line) an additional peak at $\omega_{pp} = 8.1$ THz is observed. These polariton states are allowed in this frequency and wavevector region as predicted by the dielectric function of $LiNbO_3$ introduced in section 2.2.3. The measured frequency of 8.1 THz corresponds to the frequency of the second TO mode in $LiNbO_3$, which has a frequency of 8.25 THz (275 cm^{-1}). For the first time, this mode is detected here using the ISRS method. Even the implementation of the so-called heterodyne detection scheme [7, 66] using a local oscillator field failed to detect this mode, because of its relatively small oscillator strength. The square of the ratio of the oscillator strengths of the first and second TO mode, $(S_2/S_1)^2 \approx (16)^2$, approximates the relative amplitudes of the scattered intensities from the phonon polaritons of the first and second branch of their dispersion relation. The square in the expression is due to the fact, that the coupling to the light field is considered twice: first in the excitation and subsequently in the probe process. In a common ISRS experiments with short probe pulses the scattered intensity from the second mode will be covered under the detected intensity scattered from the first mode because of the large difference in the oscillator strength of the two modes.

The probe with narrow bandwidth pulses observes phonon polaritons that belong to the second branch of the dispersion relation of the polaritons in $LiNbO_3$, because of the two following reasons: the scattered photons from the polariton modes which belong to the first and second
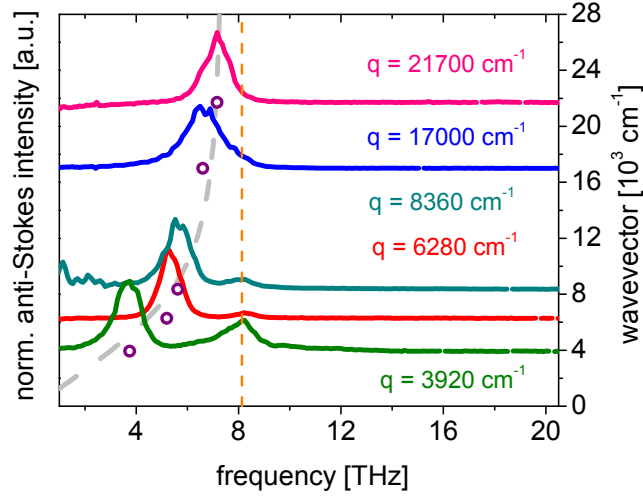
Figure 7.3: Transient normalized anti-Stokes spectra of narrow-band probe pulses scattered from the phonon polaritons in LiNbO$_3$ for different wavevectors, q. The position of the intensity peak is indicated by the purple open circles. Theoretical dispersion curve (gray dashed line). Three spectra exhibit an additional peak around 8.1 THz.

branch are separated in their energy and are detected by different pixels of the spectrometer. Further, by setting the difference frequency of the exciting laser pulses to $\Delta\omega = 6.5$ THz and the wavevector of the polariton to $\Delta k = q = 3920$ cm^{-1} the energy and momentum of the second mode are better matched than the ones of the first mode, as it is visible from the green line in figure 7.3. The frequency of the lower mode amounts in this case to 4 THz, which is obviously smaller than the difference frequency $\Delta\omega = 6.5$ THz.

For larger wavevector such as $q = 21700$ cm^{-1}, no additional peak is observable (blue line in figure 7.3), because now the selected energy $\Delta\omega = 6.5$ THz is resonant with polariton mode of the lower polariton branch, which covers the signal of the second mode. Note, the anti-Stokes spectra are normalized to the peak intensity of the lower lying mode, for a better visualization of the ration of the intensities of the first and second peak. Thus, the intensity of the second mode seems to disappear. Obviously, for higher selected wavevectors the signal of the first mode becomes such intense, that the second mode can not be observed anymore. The complementing measurements for smaller wavevectors could not be conducted because the insertion of the bandpass filters was not possible without disturbing the other laser beams. In conclusion, by setting the difference frequency of the exciting laser pulses to $\Delta\omega = 6.5$ THz and the wavevector of the polariton to $\Delta k = q = 3920$ cm^{-1} it could by demonstrated that the mode at $\omega_{pp} = 8.1$ THz is selectively enhanced, as shown in figure 7.3 as a green line. Simultaneously, the mode of the lower branch of the dispersion relation of phonon polaritons is suppressed, although it couples much stronger to the light field, according to the ratio of the oscillator strengths [27].

8 Measurement of the Dispersion Relation of Phonon Polaritons

The dispersion relation of phonon polaritons in LiNbO$_3$ was measured by different light scattering methods such as forward Raman scattering [73], stimulated Raman gain [41, 42], ISRS [7, 46, 79], and partially by terahertz time domain spectroscopy [99, 100] where the accessible frequency range amounts to only a few terahertz. The experimental results from the previously cited publications where interpreted in the framework of the common harmonic oscillator model of the dielectric function. The dispersion relation is subsequently calculated from the relation $c^2q^2/\omega^2 = \epsilon(\omega)$. Most of the experimental findings confirm this model [7, 41, 42, 46, 79, 99–101].

However, it is important to highlight the fact that in most of the cases the experiments are conducted in the so-called polariton regime. This range is in the vicinity of the avoiding crossing point that is determined by the simultaneous equality of the wavevectors $k_{light} = k_{TO-phonon}$ and the energies $\omega_{light} = \omega_{TO-phonon}$. In this regime, the terahertz light couples to the polar lattice mode and the newly originating coupled mode is the so-called phonon polariton [102]. If one excites wavevectors with relatively large magnitudes, the previously discussed model that describes the polariton dispersion relation seems to break down. The reported data from a forward Raman scattering experiment [73] indicates such a case.

This chapter is structured as follows: section 8.1 presents the observation of the lower branch of the dispersion relation of the phonon polaritons which is measured with narrow bandwidth probe pulses for extended wavevector magnitudes. In this section, the observation of phonon polaritons, which belong to the forth phonon mode in LiNbO$_3$ at 18.4 THz, and which are exclusively measured with narrow bandwidth probe pulses, is discussed, too. Next, the extended data of the polariton dispersion relation are presented in section 8.2. Then the analytical expression of the dispersion relation is introduced in detail and some limiting cases are discussed in section 8.3. Hereafter, the index of refraction for the terahertz region is determined from the data. Next, section 8.4 compares the calculated and measured dispersion relations. The limits of the model of the harmonic oscillator are pointed out in section 8.5. The dispersion relation is fitted using a fit function and the resulting parameters are analyzed in section 8.6. The physical meaning of the determined parameters and the whole procedure is scrutinized. In the next section 8.7 the response function of the Raman scattering experiment is introduced according to the derivation

of Barker and Loudon [6] and a reduced damping factor Γ in the dielectric function is accordingly introduced. The recalculation of the dispersion relation with a reduced damping constant Γ is finally compared to the measured data.

8.1 Mapping the Dispersion Relation of Phonon Polaritons with Narrow Band Pulses

In this section the dispersion relation of phonon polaritons in LiNbO$_3$ is mapped out with narrow bandwidth probe pulses. The wavevector of phonon polaritons is selected by tuning the crossing angle, Θ, of the temporally short (~ 64 fs) and spectrally broad pump pulses. Impulsively excited counter-propagating polariton wavepackets are then probed by a delayed laser pulse which undergoes stimulated Stokes and anti-Stokes scattering. The transient spectrum is detected using a spectrometer. Because the spectrum of the probe pulses is extremely narrow (~ 2 nm), the frequency of the generated phonon polariton and the light shift of the scattered light are directly observable.

In figure 8.1a, the spectra of the pump (red) and probe (pink) pulses are shown. Several normalized intensity spectra of the diffracted probe light are shown in figure 8.1b. Stokes and anti-Stokes peaks indicate the creation of left-propagating and annihilation of right-propagating phonon polaritons. The frequency shift of the probe light is a direct measure of the frequency of the quasi particle, $\omega_{pp,\frac{L}{R}} = \Delta\omega_\pm$. The wavevector magnitude, q, of the probed phonon polariton is indicated by the intersection point of the each spectrum with the y-axis and red dots indicate the coordinates of each (q, ω_{pp}) pairs. The measurement exhibits an excellent agreement with the theoretical dispersion curve that is drawn as blue line in the same figure.

Because both pump pulses $\mathbf{k}_1$ and $\mathbf{k}_2$ have the same spectrum and the excitation process is symmetric, the same polariton modes of the frequency ω_{pp} for right- and left-propagating phonon polaritons are generated. As discussed in detail in section 4.4 the narrow bandwidth probe pulses are sensitive to a subset of these excited spectra. This is experimentally proved by the Stokes (red dots) and anti-Stokes (blue dots) frequency shifts which are plotted together in figure 8.1c. Within the error bar, we observe a very good agreement of the Raman frequency shifts and the theoretical dispersion shown by the gray line.

Narrow bandwidth probe pulses allow us to map out the dispersion relation toward larger wavevectors compared to the common ISRS studies using only spectrally broad and temporally short probe pulses. Even much larger magnitudes of the polariton wavevectors can be studied by simply increasing the intersection angle Θ of the pump pulses. In principle, the temporal resolution of the narrow bandwidth probe pulse does not limit the observed polariton frequencies. Instead, the limitation is given by the excitation pulse duration. One exemplary measurement
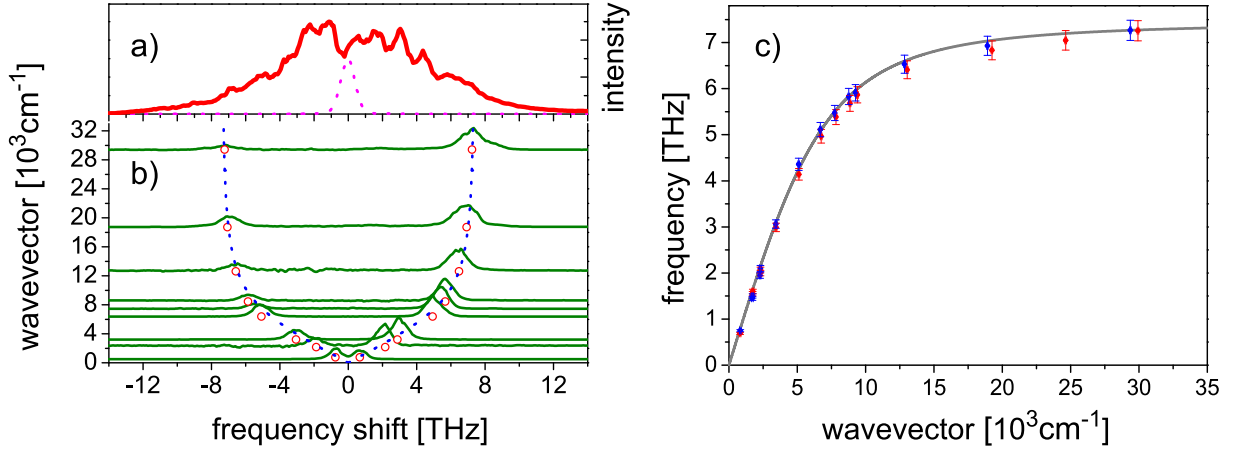
Figure 8.1: Measured dispersion relation of phonon polaritons in LiNbO$_3$. a) Spectra of the used pump (red) and probe pulses (pink). b) Spectra of the scattered narrow bandwidth probe pulses (dark green lines) for various polariton wavevectors q show that the excited counter-propagating phonon polaritons are present in the probe volume. The intersection point with the y-axis of each spectrum indicates the wavevector magnitude, q, of the probed phonon polaritons and the spectral position of the intensity peak versus the polariton wavevector magnitude is indicated by the red open circles. For comparison, the calculated dispersion relation of phonon polaritons in LiNbO$_3$ is plotted by the blue dotted line. c) The same data as in b) but the Stokes (blue circles) and anti-Stokes (red circles) frequency shifts versus wavevector of the phonon polariton, q are plotted together. The calculated dispersion relation is shown by the gray line.

that confirms this statement is shown in figure 8.2. The spectrum of the Raman scattered light from the impulsively excited phonon polaritons with the wavevector of $q = 29500$ cm^{-1} is shown by the red open circles and the incident narrow spectrum with a bandwidth of FWHM = 2 nm (~ 1 THZ) is depicted by the green open circles. Note, the x-axis indicates the frequency shift of the scattered light relative to the incident one. We observe four different intensity peaks, which correspond to the Stokes and anti-Stokes scattering of light from the phonon polaritons with the frequency of $\omega_{pp} = 7.3$ THz and from the additional phonon polaritons with the frequency of $\omega_{pp} = 18.4$ THz. The polaritons with the higher frequency belong to the branch of the dispersion relation which approaches the forth TO phonon mode in LiNbO$_3$. These polaritons are exclusively detected by probe pulses with a narrow bandwidth. Obviously, the bandwidths of the excitation pulses is sufficient to generate phonon polaritons with the frequency of $\omega_{pp} = 18.4$ THz. Indeed, the spectral width of the excitation pulses amounts to ~ 17 THz, if the width is assumed for $1/e$ of the spectrum. Thus, there is still a small amount of spectral components in the broad bandwidth pulse, that can mix and coherently excite phonon polaritons.

Using short pump and probe pulses with narrow bandwidths allows to observe higher polariton branches and subsequently allows to confirm the dispersion relation of phonon polaritons in

real samples where several TO phonon are involved. In the following sections, the discussion is extended and focuses on the case of LiNbO$_3$ where four TO phonon modes are present.
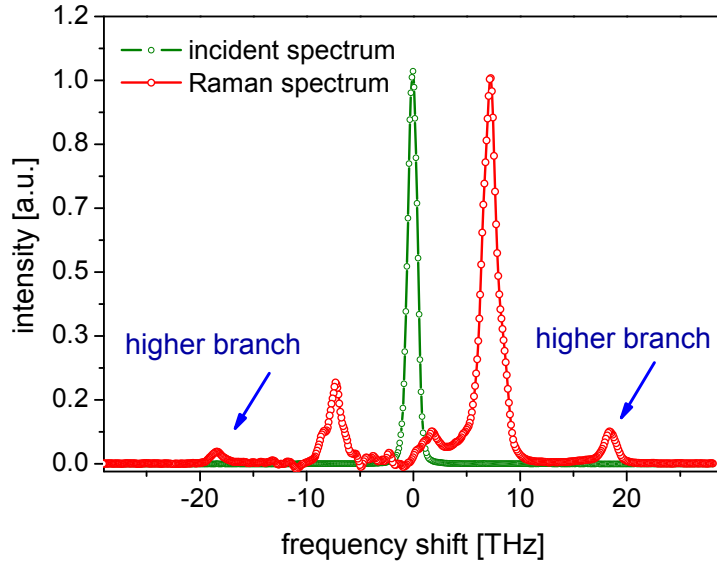

Figure 8.2: Transient spectrum of Raman scattered light from the impulsively excited phonon polaritons in LiNbO$_3$ with a wavevector of $q = 29500$ cm^{-1} (red open circles). The spectrum of the incident probe pulses is shown by the green open circles. The intensity peaks at ± 7.3 THz indicate anti-Stokes and Stokes scattered light from the phonon polaritons. These phonon polaritons belong to the lower branch of the dispersion relation. The intensity peaks at ± 18.4 THz indicate anti-Stokes and Stokes scattered light from phonon polariton which belong to the upper branch of the dispersion relation, which approaches the TO phonon mode with the frequency $\omega_{TO,4} = 18.9$ THz.

8.2 Extended Dispersion Relation of Phonon Polaritons

The frequency $\omega_{pp}(q)$ of the phonon polariton is deduced from both, the narrow band probe pulse and the short probe pulse experiments. All measured points of the polariton dispersion in LiNbO$_3$ are plotted in figure 8.3 as dark-blue circles. All frequencies which are higher than the frequency $\omega_{T,1}$ of the first TO phonon are solely measured with narrow band pulses. Additionally, the frequencies around $\omega_{pp} = 8.1$ THz are measured by exciting exclusively the right propagating polaritons as explained in section 7.2.

The data points obviously indicate three different regions of the dispersion relation: the lower polariton branch which asymptotically approaches the frequency of the first TO phonon mode in LiNbO$_3$ at $\omega_{T,1} = 7.55$ THz, polariton frequencies which lie immediate to the second

phonon mode $\omega_{T,2} = 8.2$ THz, and frequencies which belong to the upper polariton branch that asymptotically approaches the fourth TO phonon mode with the frequency $\omega_{T,4} = 18.9$ THz. Note, no signature of the third phonon mode with the frequency $\omega_{T,3} = 10$ THz is observed in these experiments, because this mode is relatively weak.
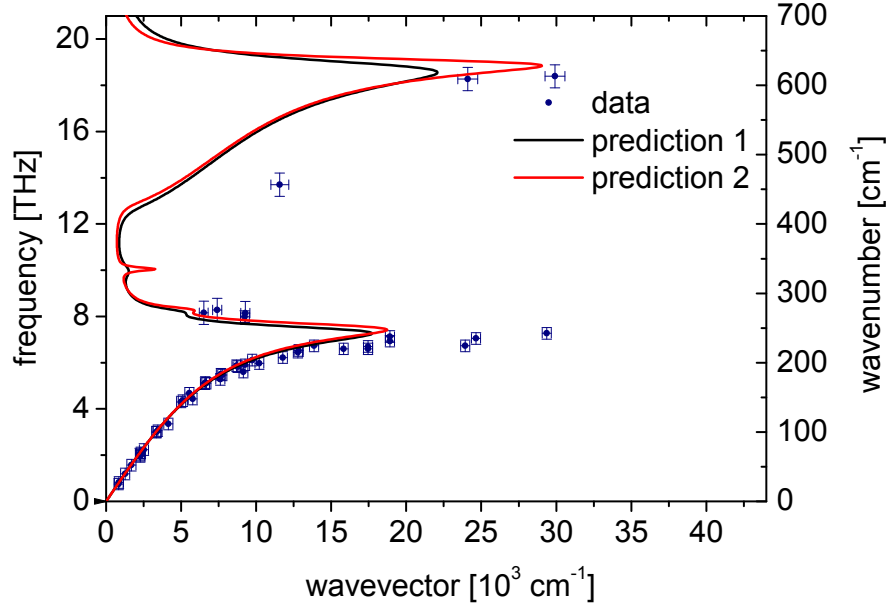

Figure 8.3: Measured and theoretical dispersion relation of phonon polaritons in $LiNbO_3$. The data obtained with temporally short and narrow bandwidth probe pulses are shown together by the blue dots. The black and the red lines show the predicted dispersion relation according to equation 8.1 with parameters taken from an infrared reflectivity measurements [27] (black line) or from the conventional Raman measurements [28] (red line). Table 8.1 lists the used parameters.

8.3 Model of the Perturbated Dielectric Function

The measured data can be compared to the theoretically predicted dispersion relation of the phonon polaritons.[1] According to the equations 2.3 and 2.4, the real part of the polariton wavevector has the form

$$\mathrm{Re}\left[q(\omega_{pp})\right] = \left(\frac{\omega_{pp}}{c_0}\right)\mathrm{Re}\left[\left(\epsilon_\infty + \sum_{i=1}^{4}\frac{S_i\omega_{T,i}^2}{\omega_{T,i}^2 - \omega_{pp}^2 - i\Gamma_i\omega_{pp}}\right)^{0.5}\right] \ , \tag{8.1}$$

---

[1]Because of the relatively large thickness of the sample (~ 0.5 mm), waveguide effects are not important in this work.

where S_i is the oscillator strength of the i-th TO mode, $\omega_{T,i}$ is its resonance frequency, Γ_i is the damping constant of the i-th TO mode, and c_0 is the light velocity in vacuum. ϵ_∞ is the high-frequency contribution to the dielectric constant. It accounts for the contribution of higher-lying phonon modes outside of the measurement range [73] and for all purely electronic interband transitions [27].

Next, a simplified expression for the real part of the polariton wavevector is introduced. In the case where only the lower polariton branch is considered the contribution of all other modes can be expressed by an effective dielectric constant ϵ_{eff}. Equation 8.1 simplifies to

$$\mathrm{Re}\left[q(\omega_{pp})\right] = \left(\frac{\omega_{pp}}{c_0}\right)\mathrm{Re}\left[\left(\epsilon_\infty + \epsilon_{eff} + \frac{S_1\omega_{TO,1}^2}{\omega_{TO,1}^2 - \omega_{pp}^2 - i\Gamma_1\omega_{pp}}\right)^{0.5}\right]. \tag{8.2}$$

This expression was used in the works by Wiederrecht [79] and Crimmins [7] where the predictions were consistent with the obtained data. The linear part of the polariton dispersion relation is determined by the low-frequency dielectric constant, ϵ_0, which consequently determines the velocity, $c_{THz} = c_0/\sqrt{\epsilon_0}$, of terahertz light in LiNbO$_3$. It can be obtained from equation 8.1 or 8.2, if the frequency ω approaches zero:

$$\lim_{\omega\to 0}\epsilon(\omega) = \epsilon_0 = \epsilon_\infty + \sum_{i=1}^{4} S_i. \tag{8.3}$$

By fitting a linear slope to the data shown in figure 8.3 which were measured at low frequencies, the low-frequency dielectric constant is determined to $\epsilon_0 = 27.35$. This corresponds to a refractive index $n_{THz} = 5.23$. A reference value of ϵ_0 is inferred for example from a measurement using terahertz time domain spectroscopy. Kojima determined $\epsilon_0 = 27.6$ [99] which agrees well with the obtained value in this work.

8.4 Calculation of the Dispersion Curve

Now, let us proceed with the calculation of the dispersion relation using equation 8.1. The parameters from reference [27] which were obtained with an infrared reflectivity measurement are listed in the first column of table 8.1. The predicted low-frequency dielectric constant ($\epsilon_0 = 24.4$) is 9% smaller than the one determined in this work. Note, in the publication of Barker and Loudon [27] there is a confusing disagreement concerning the value of the dielectric constant ϵ_0: on the one hand, the sum over all noted oscillator strengths S_i and ϵ_∞ gives $\epsilon_0 = 24.4$ as written in table four of reference [27]. On the other hand, the authors discuss in their paper a value of $\epsilon_0 = 26.0$ which is closer to the value determined in this work.

The black line in figure 8.3 shows the function obtained from the calculation using equation 8.1 with the parameters listed in the first column of table 8.1. In the lower branch of the dispersion,

the model (prediction 1) suggests the appearance of points only up to $q = 16500$ cm^{-1}. The second mode is extremely weak in this model and in the fourth branch the curve does not exceed $q = 24000$ cm^{-1}.

i	υ (cm^{-1})	γ (cm^{-1})	S	υ (cm^{-1})	γ (cm^{-1})	υ (cm^{-1})	γ (cm^{-1})	S
1	252	21	16.0	252.9	19.9	249.7	3.28	19.65
2	276	14	1.0	277.1	11.1	276.8	5.8	2.81
3	333	25	0.16	335.5	5.8	335.2	40	0.3
4	634	34	2.55	633.9	20.0	634.2	30	5.0
	ϵ_∞	= 4.6					ϵ_∞	= 3.97

Table 8.1: Room-temperature central frequency υ, line width γ, and absorption strength, S, of the four TO phonons in LiNbO$_3$ which are polarized parallel to the c-axis. First column: parameters are obtained from an infrared reflectivity measurement in Ref. [27], second column: parameters are obtained by an fit-analysis of the Raman scattering data from Ref. [28] (as previously discussed in section 2.2.2), third column: parameters determined by the optimization of the simulation to the measured data shown in figure 8.5 by the green line.

The same calculation using equation 8.1 and inserting the parameters taken from the analysis of a conventional Raman spectrum (see section 2.2.2) from reference [28] is depicted by the red line in figure 8.3. The parameters extracted from the Raman spectrum are given in the second column of table 8.1. In contrast to the dispersion curve that was derived using infra-red reflectivity data, the new dispersion curve with included Raman scattering data exhibits a clear feature at the second TO phonon frequency of 8.13 THz. However, the lower dispersion branch describes the data not as well as the previous model for wavevectors larger than 9000 cm^{-1}. The fourth branch extends to much larger wavevector magnitudes because of the smaller damping constant Γ_4 in this case.

It is important to note that the parameters, which are used for the calculation of the dispersion relation, were extracted either from Raman scattering or from infrared reflectivity measurement. One can argue, if these parameters are applicable to the description of the dispersion of phonon polaritons. The result from Raman scattering provides a peak width which corresponds to an average life time of thermal phonons. This is the time between two scattering events of the phonon with the thermal phononic bath and defects in the crystal [32]. However, the measured wavevectors of the phonons are typically on the order of $k \approx 3 \cdot 10^5$ cm^{-1} which is much larger than the wavevector of phonon polaritons $q \approx 8000$ cm^{-1} in LiNbO$_3$. It is known that the

damping of the phonons exhibits a dependence on the wavevector magnitude [32], which is correlated to the spatial distance of defects and impurities. Once the wavelength of a phonon is comparable to the distance between the scattering centers, the observed damping increases. However, no reports of this behavior of the damping in stochiometric and congruent lithium niobate sample are known. Thus, the damping can be taken from the data obtained with conventional Raman scattering.

Next, I will focus on infrared reflectivity measurement and review the subsequent data analysis. The measured quantity in the reflectivity measurement is the frequency-dependent light intensity $R(\omega)$ reflected from the sample of interest. R is called reflectivity or sometimes reflectance and is related to the complex index of refraction $N = n + i\kappa$ via the Fresnel formula for reflection at normal incidence [103]

$$\sqrt{R} = r = (n + i\kappa - 1)/(n + i\kappa + 1) = |r|e^{i\phi} \ , \tag{8.4}$$

where $|r|$ is the amplitude of the E-field of the reflected light, ϕ is the phase, and n, κ are the index of refraction and the extinction coefficient, respectively. In an infrared reflectivity experiment the relative intensity of the reflected light is measured and thus the phase ϕ remains initially unknown. In order to obtain the phase ϕ Kramers-Kronig transformation is applied to the measured values of R. This allows to relate the phase $\phi(\omega)$ and the measured amplitude $|r|$ according to [104]

$$\phi(\omega_0) = \frac{2\omega_i}{\pi} \int_0^\infty \frac{\ln|r(\omega)|}{\omega^2 - \omega_i^2} \ \mathrm{d}\omega \ . \tag{8.5}$$

This integral is usually solved numerically and appropriate extrapolation formula have to be used for the low and high-frequency limits. As soon the phase $\phi(\omega)$ is calculated, the complex index of refraction $N(\omega)$ can be determined from the Fresnel formula given in equation 8.4 and afterwards the imaginary part of the dielectric function $\epsilon_i(\omega) = 2n(\omega)\kappa(\omega)$. Hereafter, the calculated curve $\epsilon_i(\omega)$ is analyzed to obtain the central frequency ω_i, the strength S_i, and the damping Γ_i of the contributing phonon modes. The oscillator strength S_i of the i-th mode is conveniently determined from the area under the $\epsilon_i(\omega)$ curve [103] by the relation

$$S_i = \frac{1}{\pi^2\omega_i} \int n\kappa \ \mathrm{d}\omega \ . \tag{8.6}$$

According to Thomas and Hopfield the accuracy of this procedure for estimating S_i is about 10-20% [105]. The requirement is that the resonances are sufficiently far apart so that the mutual interaction of the modes is negligible [104]. In order to obtain the frequency ω_i and the damping constant Γ_i, a classical oscillator model has to be fitted to the $\epsilon_i(\omega)$ curve [27, 106]. In this case, the damping constant Γ is related to the width of spectral peak and thus it is equal to the value which is used for the calculation of the polariton dispersion relation.

One question remains open: The analysis of the infrared reflectivity data does not take into account any interaction of the irradiated light with the phonon polariton modes. It only considers the interaction with discrete and purely optical phonon resonances and thus may not accurately describe the measurement. The reflectivity data from $LiNbO_3$ obtained by Barker and Loudon [27] do not show evidence for such a discrepancy. But the reflectivity measurement of $LiTaO_3$ exhibits a pronounced disagreement between the measured data point and calculated curve as reported in reference [107]. This may be a signature for the limitations of this analysis.
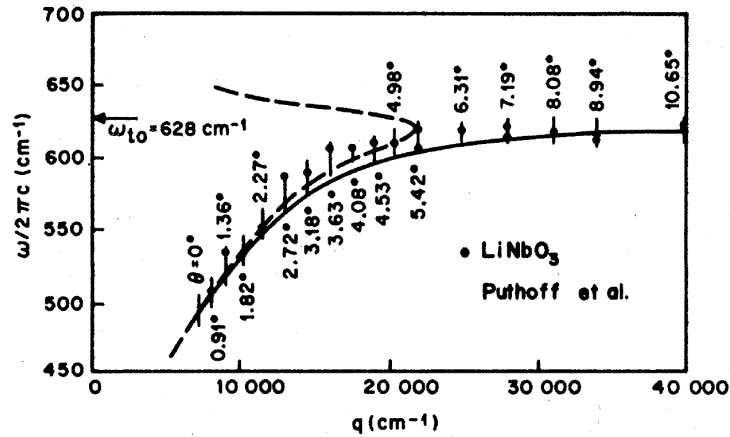

Figure 8.4: Near-forward Raman scattering measurement (black dots) of the higher branch of the dispersion curve of the phonon polaritons in $LiNbO_3$ published by Puthoff *et al.* [73] The dashed line is the calculated dispersion curve with the parameters listed in the first column of table 8.1 which are taken from reference [27]. The solid line shows the same calculation, but with a very small damping value Γ, as predicted by Barker and Loudon in reference [6].

8.5 Limits of the Model of the Phonon Polariton Dispersion

One may ask where the model, which describes the polariton dispersion, starts to break down. A possible answer to this question is discussed by Puthoff *et al.* in reference [73] who published data which were obtained by near-forward Raman scattering in $LiNbO_3$ and are reproduced in figure 8.4. The authors examined the higher polariton branch shown by the black dots which at first follows the drawn theoretical dispersion curve shown as dashed line and hereafter asymptotically approaches the purely mechanical phonon branch with the frequency $\omega_{T,4} = 628$ cm^{-1} (18.8 THz). The same situation seems to occur for the lower polariton branch which is investigated in the present work and are shown in figure 8.5.

In the main range of the dispersion relation the mechanical vibration and the infrared-field generated by the lattice vibration propagate through the crystal in-phase and the theoretical dispersion relation of phonon polaritons applies. For much higher wavevectors, the dispersion

is determined by only the mechanical vibration which is nothing else than a phonon. The infrared-wave and the mechanical vibration exhibit a phase mismatch and are not longer coupled in this frequency range. But the situation is even more complicated because an intermediate regime is found where the crossover from the phonon polariton to the purely phonon-like behavior takes place.
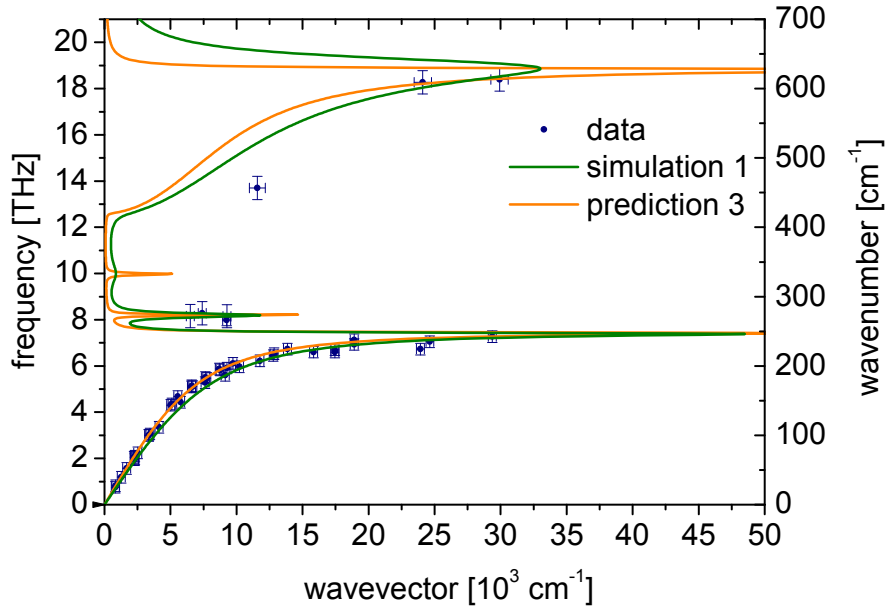

Figure 8.5: Measured and simulated dispersion relation of phonon polaritons in $LiNbO_3$. The experimental data are shown by the blue dots and are the same as displayed in figure 8.3. The green line shows the simulation according to equation 8.1. The optimized parameters are listed in the third column of table 8.1. The orange line is a prediction using parameters from a reflectivity measurement [27] but with ten times smaller damping rates $\Gamma_i = 1/10 \cdot \Gamma_{IR}$ according to Barker and Loudon [6].

8.6 Simulation of the Phonon Polariton Dispersion

The simulation of the dispersion relation is shown as the green line in figure 8.5 and exhibits a good agreement with the measured data. The curve extends to the data points with a large magnitude of the polariton wavevector. The analysis function is given by equation 8.2. The oscillator strength, frequency and damping where extracted with a fit routine, where the parameter space has been limited by physically reasonably boundaries. The obtained fit parameters are listed in the third column of table 8.1. In particular, the variation of each TO phonon frequency $\omega_{T,i}$ was fixed to $\Delta\omega_{T,i} = \pm 0.3$ cm^{-1} because it is well known that the exact value is very sensitive

to temperature [21], the exact composition [17, 18] and purity of the sample. The value of the high-frequency dielectric constant, ϵ_∞, is sensitive to the composition and purity of the sample. Further it is an extrapolated value which strongly depends on the range of the measurement data and the extrapolation method. Thus, the limits of ϵ_∞ was set to $\pm$ 0.2.

The simulation determines the low-frequency dielectric constant to $\epsilon_0 = 32.2$, which is 16% larger than for example measured by Kojima [99]. The simulation yields larger values of the oscillator strengths than obtained from the reflectivity measurement [27], but they seem to be reasonable. The observed damping rate $\Gamma_1 = 3.28$ cm^{-1} is very close to the value of $\Gamma_1 = 3.4$ cm^{-1}, which was reported by Schwarz and Meier from their stimulated Raman gain measurements in LiNbO$_3$ at 77 K [42]. Further, the determined damping rates Γ_1 and Γ_2 (5.8 cm^{-1}) from the simulation here exhibit a significant deviation: Γ_1 is 6.5 times smaller and Γ_2 is 2.5 times larger than the values reported by Barker and Loudon [27]. Thus, the determined parameters should be interpreted with caution.

8.7 Discrepancy of the Data and Theoretical Predictions

The discrepancy between the obtained data points and the theoretical predictions of the dispersion relation of the phonon polaritons was in detail examined by Barker and Loudon [6]. In their paper, a coupled two oscillator model was introduced to describe the polar lattice in the presence of mechanical and electromagnetic waves. They define a general response function F which describes the response of a polar mode in a dielectric material to an external force caused by a light field. For a phonon polariton the response function takes the form

$$F = 1/((q^2 c^2/\omega^2) - \epsilon(\omega)) \ \ .\tag{8.7}$$

Here the dielectric constant is defined as in equation 2.4. The maximum of the imaginary part of F indicates the frequency of the polariton mode itself that is observed by a Raman light scattering experiment. Furthermore, Barker and Loudon show that in most experimental cases–which are applicable as well to the present work–the measured dispersion relation is well described by the same dielectric function as previously discussed (see equations 2.4 and 8.1), but with much smaller and almost negligible damping constants Γ_i. They proved this finding by a comparison to the data from the forward Raman scattering experiment on phonon polaritons in LiNbO$_3$ which was reported by Puthoff *et al.* [73]. The black solid line which was calculated using the model of Barker and Loudon asymptotically approaches towards the fourth TO phonon branch in LiNbO$_3$ at 628 cm^{-1} as shown in figure 8.4.

In figure 8.5 another calculated curve is shown by the orange line. In this case, the damping rates are set to ten times smaller values than determined by the infrared reflectivity [27]. I obtain a good agreement of the prediction and the measured data for all detected phonon polariton

dispersion branches in LiNbO$_3$. It should be noted that in figures 8.1b and 8.1c the gray lines depict the calculated dispersion relations which already account for the fact that the damping rate Γ is negligibly small.

Note, the conclusions of the findings of this chapter are later presented in the end of chapter 9 in section 9.6. This is done to emphasize the close connection of the complex dispersion relation of phonon polaritons: the determined frequency-dependent damping of phonon polaritons is directly related to the imaginary part of the phonon polariton wavevector.

9 Frequency-Dependent Damping of Phonon Polaritons

Advances in the efficient generation of ultra-short terahertz pulses was essential for the development of terahertz time domain spectroscopy [108, 109]. Very recently, the generation of intense terahertz pulses with only one or a few-cycles via optical rectification in non-linear crystals was demonstrated [9, 110]. Peak fields amplitudes of up to 400 kV/cm were achieved [111]. Such large field amplitudes open new perspectives in non-linear terahertz spectroscopy [9] and enable an intense and direct excitation of lattice modes in solid samples [112].

Because of the high non-linearity, a relatively low absorption in the terahertz region, a large bandgap (~ 3.7 eV), and a high optical damage threshold in the visible range, samples of $LiNbO_3$ and its doped species show excellent suitability for the generation of high power ultra-short terahertz pulses [8, 48, 49, 56, 113, 114] via optical rectification of femtosecond laser pulses. In $LiNbO_3$ and in other used polar dielectrics the electromagnetic terahertz field propagates as a phonon polariton and can be coupled out into free space. Besides the pulse tilting and phase matching arguments [48, 54], the absorption or damping of the phonon polaritons is crucial for the actual emitted field amplitudes and power of terahertz radiation [113]. In this context, the knowledge of frequency-dependent damping of phonon polaritons is of special importance. The frequency-dependent damping of the phonon polaritons in samples of $LiNbO_3$ with different stoichiometry and doping was investigated with stimulated Raman gain and conventional Raman scattering [42, 115, 116]. The polariton damping was also determined by ISRS [7] and by terahertz time-domain spectroscopy [99, 100] in the linear regime of the dispersion relation, that is for small frequency values, too. These experimental findings cannot be well described by a simple model that includes a single polar phonon mode with an eigenfrequency $\omega_{T,1}$ and a damping constant Γ_1. These assumptions result in the dielectric function

$$\epsilon(\omega) = \epsilon_{eff} + S_1 \omega_{T,1}^2 / (\omega_{T,1}^2 - \omega^2 - i\omega\Gamma_1) \ , \tag{9.1}$$

where S_1 and ϵ_{eff} are the oscillator strength and the effective high-frequency dielectric constant, respectively. In order to include additional contributions that may lead to experimentally observed frequency-dependent increase of the observed polariton damping, the simple model has to be extended as will be explained in the following.

In section 9.1, the room temperature frequency-dependent damping rate of the phonon polaritons in LiNbO$_3$ as measured by ISRS is presented. In section 9.2, the effect of the propagation of the phonon polaritons out of the probe volume is discussed and the data are subsequently corrected for this effect. Next, in section 9.3 the determined damping rate is compared to a model of the polar phonon mode with constant damping Γ_1. In the same section it is shown that an improvement of the description of the experimental data can be achieved using a smaller damping constant of the phonon mode which was previously obtained from the fitting analysis of the dispersion relation in section 8.6. In sections 9.4, the coupling of the polaritons to the low-frequency defect modes is discussed. Next, the results of this work are compared with previously reported measurements [7, 42] and the contribution of the relaxational mode to the damping of phonon polaritons is discussed in section 9.5. Finally, section 9.6 draws a conclusion and shows that in this work the complex dispersion relation of phonon polaritons in LiNbO$_3$ is obtained by the simultaneous measurement of their frequency-dependent damping and wavevector-dependent frequency.

9.1 Damping of Phonon Polaritons Measured with ISRS

The impulsively stimulated phonon polaritons are measured using short and variably delayed probe pulses. The transient Raman scattered intensity decays according to equation 5.9 with twice the damping rate, $2\gamma_{pp}$. Hence, the data are evaluated with a Fourier analysis where the half width of the spectral peak corresponds to the polariton damping rate γ_{pp}, as it has been previously discussed in sections 4.2 and 4.3, respectively. The damping rate γ_{pp} of the phonon polaritons in LiNbO$_3$ is plotted versus the frequency ω_{pp} in figure 9.1 using the red and black squares, respectively. Note, the red data points have been obtained using laser beams with a spatial width of FWHM$\sim$ 1.2 mm whereas the black data points result from the measurement with laser beams with a spatial width of FWHM$\sim$ 0.8 mm.

9.2 Polaritons Leaving the Probe Volume

It is known that the phonon polaritons propagate with light-like speeds in the sample. Especially for small wavevector magnitudes in the linear region of the dispersion relation, the group velocity in LiNbO$_3$ amounts to $v_g 0.2c_0$, as previously discussed in sections 2.3.2 and 8.3. Because of their high velocity, the phonon polaritons leave the probed volume and thus do not longer contribute to the scattering of the probe light which consequently results in a decrease of the scattered intensity. To account for this effect the envelopes of the generated phonon polariton wavepacket and the probe pulse in the relevant dimensions have to be considered during the data analysis. Assuming an identical Gaussian envelope function for both interacting electromagnetic fields
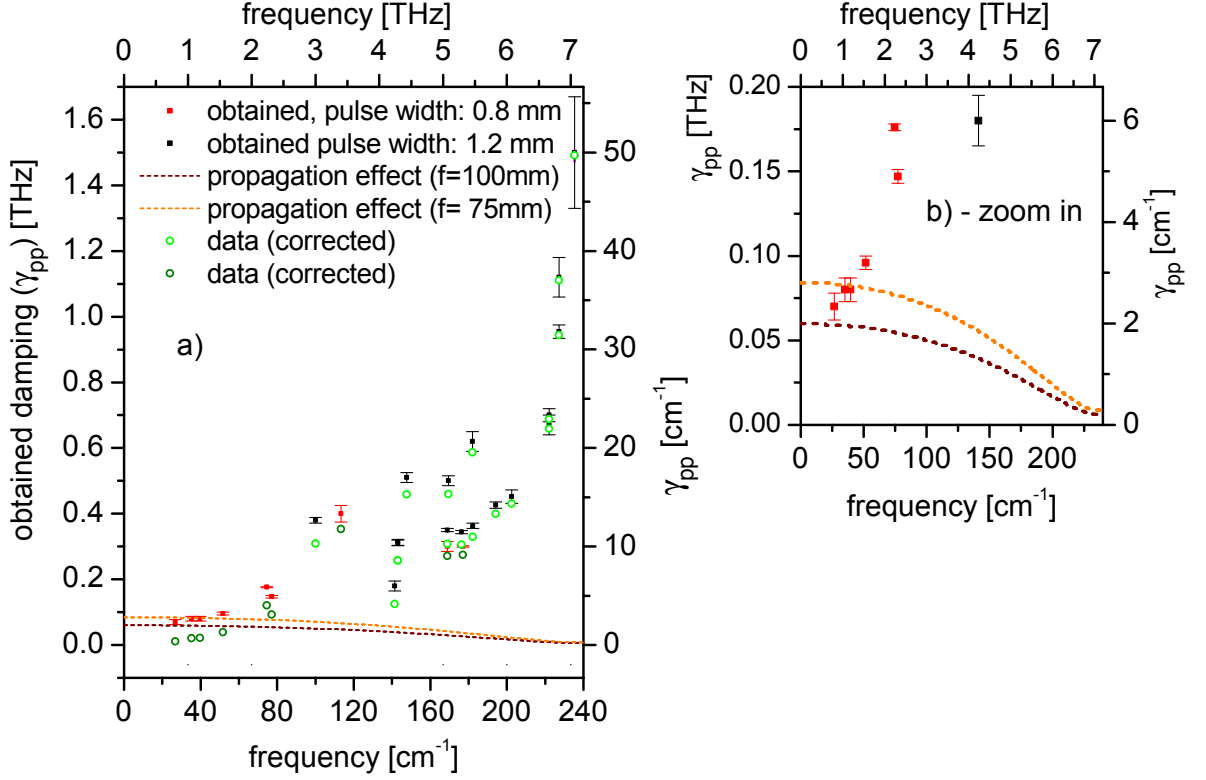
Figure 9.1: Propagation effect on the observed damping of the phonon polaritons. a) Frequency-dependent damping rate, γ_{pp}, of the phonon polaritons in LiNbO$_3$ as obtained by ISRS with short probe pulses shown by the red (width of the laser beams, FWHM = 1.2 mm) and black (width of the laser beams, FWHM = 0.8 mm) squares. The effect of phonon polaritons leaving the probe volume is indicated by the orange and brown lines for the case of the widths of the laser beams of 0.8 mm and 1.2 mm, respectively. Subsequently, the experimentally obtained data points are corrected for this effect and the resulting data points are shown by the olive and bright green open circles. b) Zoom into a).

and the relative velocity $v_g \cos \beta$ of the polariton wavepacket with respect to the probe light, the problem reduces to the calculation of the overlap integral of both Gaussian functions. The full calculation is presented in appendix (A.2). The decay of the scattered field is proportional to $\approx e^{-\frac{l}{2\sigma^2}}$, where l is the traveling distance after the excitation and σ is the width of the Gaussian function. The $1/e$ life time is then equal to

$$\tau_{\frac{1}{e}}(\omega_{pp}) = \frac{\text{FWHM}}{\sqrt{2\ln 2}} \frac{1}{v_g(\omega_{pp})\cos \beta} \quad . \tag{9.2}$$

The group velocity $v_g(\omega_{pp})$ is calculated using equation 2.5. The damping constant is obtained from the relation $\gamma_{\frac{1}{e}}(\omega_{pp}) = 1/\tau_{\frac{1}{e}}(\omega_{pp})$. In figures 9.1a and 9.1b the orange and brown lines represents the result of the calculation for the spatial widths of ~ 0.8 mm and ~ 1.2 mm of the

laser beam, respectively. From figure 9.1b it becomes obvious that only in the region of small polariton frequencies the contribution to the observed damping is significant.

In the following, the data can be corrected for the effect of the propagation of the polaritons out of the observation volume. In figure 9.1a the olive and bright green open circles show the corrected data points. For very small frequencies the determined polariton damping rate amounts to $\gamma_{pp} = 0.01$ THz, which corresponds to an average lifetime of $\tau_{av} = 100$ ps. This leads to to a propagation distance of $l = 6$ mm. Obviously, for the case of small damping the polaritons can travel up to several centimeters through the sample [92, 117].

9.3 Constant Damping Rate of the TO-Phonon Mode

In this section, the data are compared to the calculated damping rate with parameters obtained from far-infrared reflectivity measurements [27]. The imaginary part of the polariton wavevector $\mathrm{Im}(q)$ is related to the observed damping rate γ_{pp} via the relation $\gamma_{pp} = v_{ph}\mathrm{Im}(q)$. Further, the phase velocity is determined by the real part of the wavevector $v_{ph} = \omega_{pp}/\mathrm{Re}(q)$ which is the velocity of the propagation of a monochromatic plane polariton wave. The phonon polariton damping is subsequently calculated using

$$\gamma_{pp} = \omega_{pp}\frac{\mathrm{Im}(q)}{\mathrm{Re}(q)} = \omega_{pp}\frac{\mathrm{Im}[n(\omega_{pp})]}{\mathrm{Re}[n(\omega_{pp})]} \quad . \tag{9.3}$$

The analysis of the reflectivity measurement [27] yields $\Gamma_1 = 21$ cm^{-1}, $S_1 = 16$, and $\epsilon_{eff} = 8.3$. The corresponding frequency-dependent damping of the phonon polaritons is shown by the light blue line in figure 9.2. The experimentally determined data points follow the trend of the calculated curve for low values of ω but above 170 cm^{-1} (5 THz) the calculated damping rate increases drastically and implies higher damping rates. A better description of the experimental data could be obtained with a smaller value of the damping, which is shown by the red line in figure 9.2 for $\Gamma = 9$ cm^{-1}.

Next, this calculation is repeated using parameters obtained from the fitting procedure of the dispersion relation of phonon polaritons as discussed in section 8.6. The violet line in figure 9.2 shows the results of this calculation with the parameters $\Gamma_1 = 3.28$ cm^{-1}, $S_1 = 19.65$, and $\epsilon_{eff} = 12.08$. The result of the calculation seems to be not very sensitive to the exact value of the damping constant Γ_1. Here, all values between $9 < \Gamma_1 < 3$ can be used to describe the behavior of the obtained damping rate of phonon polaritons. To remain consistent with the results of the analysis presented in previous chapter 8, the discussion in the following will be based on the results of the fit procedure of the dispersion relation.
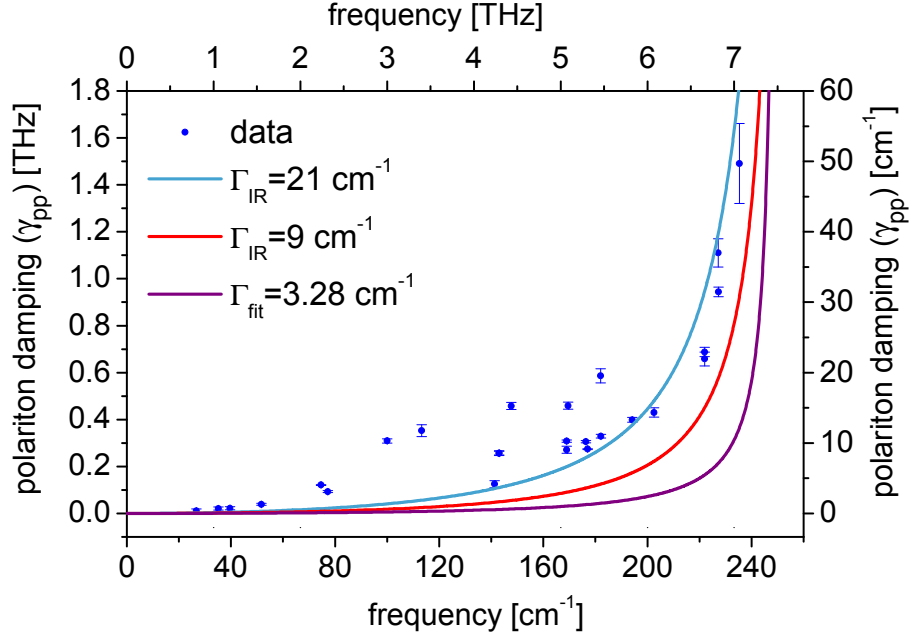
Figure 9.2: Frequency-dependent damping rate, γ_{pp}, of the phonon polaritons in LiNbO$_3$ as obtained by the ISRS experiment using short probe pulses shown as the blue circles. Calculated damping of phonon polaritons assuming a dielectric function with a constant damping rate $\Gamma_1 = 21$ cm^{-1} (light blue line), $\Gamma_1 = 9$ cm^{-1} (red line) and the result of the fit procedure of the dispersion relation with a damping rate of $\Gamma = 3.3$ cm^{-1} (violet line). For the details of the respective models, see sections 8.4 and 8.6, respectively.

9.4 Coupling to Low-Frequency Modes

The data discussed up to now exhibit in the region 2.5 THz $< \omega_{pp} <$ 6 THz signatures of additional contributions to the polariton damping rate. These signature cannot be explained by the simple model that assumes only a constant damping Γ_1. One possibility to explain the additional structures observed in the frequency-dependent damping rate of the phonon polaritons can for example be explained by coupling to low-frequency modes. Here, the mechanical part of the phonon polariton couples to the so-called defect modes which were previously reported [42,115,116]. In this case the damping constant Γ_1 is replaced with an effective damping constant

$$\Gamma_{eff}^{(2)} = \Gamma_1 + \frac{1}{i\omega} \sum_j \frac{K_j}{\omega_{low,j}^2 - \omega^2 - i\omega G_j} \quad . \tag{9.4}$$

$\omega_{low,j}$ and G_j are the eigenfrequency and damping constant of the j-th low-frequency mode, and K_j corresponds to the coupling constant of the phonon polariton to this particular excitation. Seven low-frequency modes were for example inferred from spontaneous Raman scattering and also stimulated Raman gain measurement at 77 K in a nearly stoichiometric LiNbO$_3$ sample [42].
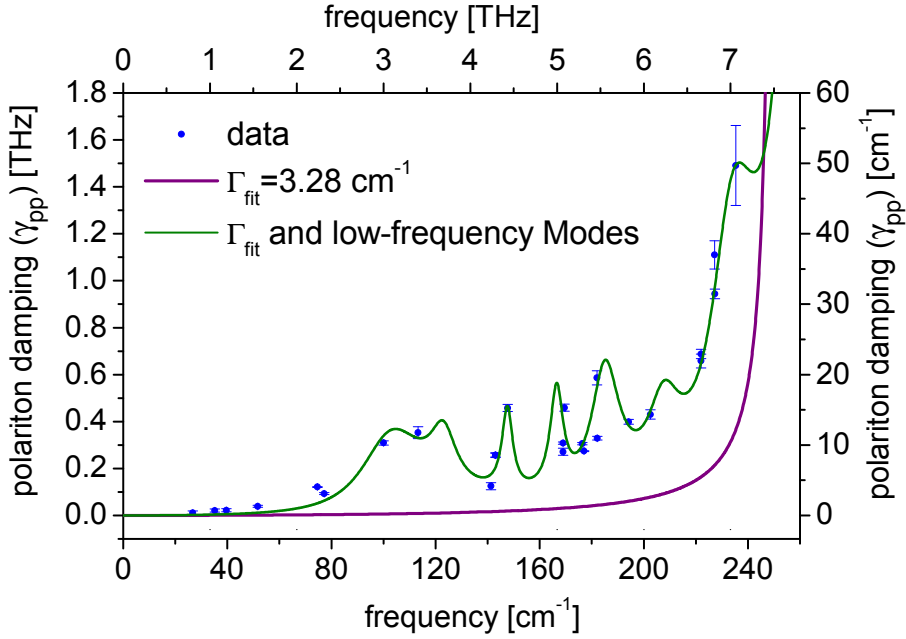
Figure 9.3: Frequency-dependent damping rate, γ_{pp}, of the phonon polaritons in $LiNbO_3$ as obtained by the ISRS with short probe pulses shown by the blue circles. Calculated damping γ_{pp} of phonon polaritons assuming a dielectric function (Eq.: 9.1) with parameters that are obtained in this work from the fit procedure is shown by the purple line. The measured data are very well reproduced by a model (green line) that additionally takes into account the coupling of the mechanical part of the phonon polaritons to low-frequency defect modes [42].

It is appropriate to attribute the observed structures to such modes even though the number of measured damping values for different q in this work is relatively small. Nevertheless, the result of the model including seven low-frequency modes which were reported by Schwarz *et al.* [42] is shown by the green line in figure 9.3. Accounting for these modes [42] enables a significantly better description of the observed frequency-dependent damping rate of phonon polaritons. The central frequencies, oscillator strengths, and damping constants of the modes that were included in the model calculation are listed in table 9.1.

The included resonance terms given by equation 9.4 also affect the real part of the calculated wavevector q. However, this influence is smaller than the resolution of the present experiment.

It is important to note that the determined damping constants in this work are comparable–up to factor of 2–with those reported in [42]. The coupling constants are larger than the ones previously reported in the same publication. Due to the different temperatures at which the experiments are performed–in the CARS experiment the sample was cooled down to 77 K, here the sample stays at room temperature,–one would expect an increase of the observed damping rates of phonon polaritons [101, 116]. This is not the case here. The direct comparison of the

parameters obtained in this work with those determined by Schwarz and Maier [42] is difficult, because the attributes of the defect modes, as well as of the phonon modes, are dependent on the exact composition, degree of purity, temperature, exact growth method and macroscopic and microscopic stresses in the sample [118–120].

Crystal	ω_{low}	G	K
LiNbO$_3$	[cm^{-1}]	[cm^{-1}]	[10^{6}cm^4]
	106	33 (29.7)	9.0 (45.0)
/nearly	125	20 (12)	3.0 (15.0)
stoich.	148	10 (5)	0.8 (7.2)
	167	20 (6)	1.2 (8.4)
77 K (300 K)	188	13 (13)	1.7 (1.9)
	217	10 (15)	2.0 (9.0)
	233	10 (22)	2.0 (2.0)

Table 9.1: Low-frequency modes obtained from spontaneous Raman scattering after Schwarz and Maier [42] at 77 K in a nearly stoichiometric LiNbO$_3$ sample and from present ISRS experiment at room-temperature in LiNbO$_3$ (optimized parameters are written in brackets). ω_{low} denotes the eigenfrequency, G the damping constant, and K the coupling constant of the low-frequency mode, as defined in equation 9.4.

9.5 Comparison With Other Measurements and Discussion

The measured damping rate is now compared to two other experimental measurements of the frequency-dependent damping rate of phonon polaritons. The red squares in figure 9.4a and 9.4b represent the results of the stimulated Raman gain measurement by Schwarz and Maier [42]. The experiment was carried out at $T = 77$ K in a nearly stoichiometric LiNbO$_3$ sample. This experiment exhibits a similar behavior of the damping rate as function of frequency, namely a first peak is centered around 3 THz, followed by several peaks in the region between 4.2 THz and 6 THz, and a distinct increase of the observed damping rate for frequencies larger than 6 THz. As expected, the measured damping in the CARS experiment at 77 K is lower than the ISRS data obtained at room temperature. The temperature dependence of the damping in congruent LiNbO$_3$ sample was also reported in reference [116].
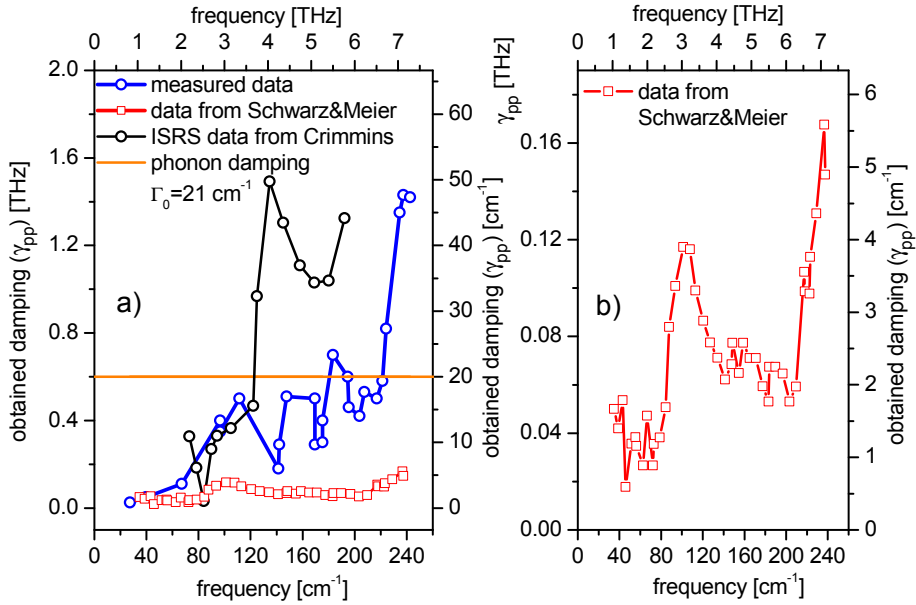
Figure 9.4: Comparison of the measured polariton damping rate, γ_{pp}, with published investigations of polariton damping in LiNbO$_3$. a) Measured data during this work are shown by the blue open circles, the results of the ISRS measurement reported by Crimmins *et al.* [7] is indicated by the black open circles, and the data obtained with the Raman gain experiment at 77 K in a nearly stoichiometric LiNbO$_3$ sample reported by Schwarz and Maier [42] are shown by the red open circles (A zoom in is shown in b)). The damping rate ($\Gamma_{TO,1} = 21$ cm^{-1}) of the first TO phonon mode is drown by the orange line.

A different measurement of the frequency depended damping of phonon polaritons is shown by the black open circles in figure 9.4a. This data are obtained by ISRS by Crimmins *et al.* at room temperature in LiNbO$_3$ [7]. Their data show two prominent peaks in the damping rate, γ_{pp}. For low-frequencies, a good agreement of the data obtained during this work and their results is obtained, albeit for higher frequencies ω_{pp} the reported values are larger than the ones measured in this work. In reference [7] no further explanation or discussion of the polariton damping in LiNbO$_3$ is found. However, the authors reference [79] where polaritons in LiTaO$_3$ are studied by ISRS. In this report a behavior of the polariton damping in LiTaO$_3$, which is very similar to that in LiNbO$_3$ was observed and explained in terms of a single polariton mode with a constant damping Γ and a coupling to a relaxational mode. However, the effect of the propagation of phonon polaritons out of the probe volume was not included in their calculations [79]. This fact might already account for the higher damping rates observed at small polariton frequencies.

In this work during the analysis of the data, the additional coupling of phonon polaritons to a relaxational mode was carefully considered. It is known that in ferroelectric materials a low-energy

relaxational mode–frequently called Debye mode–often plays an important role [83, 116, 121–123]. This concept applies well for example in the case of BaTiO$_3$ [124]. Qiu *et al.* explicitly included the coupling of phonon polaritons in congruent LiNbO$_3$ to the Debye relaxational mode in order to describe the observed behavior of the polariton damping even at room temperature [116]. Ridah *et al.* studied the temperature-dependence of Raman lines in a nearly stoichiometric LiNbO$_3$ crystal in the temperature range between 300 K and 1100 K [28]. They found evidence for the appearance of a Debye relaxational mode in their data for temperatures above 450 K. In contrast, the room temperature Raman spectra do not show any signatures of a Debye contribution to the scattered intensity. In this work, the ISRS data measured at small polariton frequencies ω_{pp} are well described by the model of a damped harmonic oscillator and no evidence of a contribution of the relaxational mode is observed. Moreover, the inclusion of the effect of propagation to the observed damping can completely describe the obtained damping of the phonon polaritons at small wavevectors q_{pp}. According to the present data obtained at room temperature, the coupling of phonon polaritons to a relaxational Debye mode does not play an important role.

9.6 Conclusions

In this chapter, the obtained frequency-dependent damping γ_{pp} of phonon polaritons in LiNbO$_3$ was analyzed. The data are well described by a model, which assumes the complex dielectric function with parameters, as previously determined by the fit analysis of the measured frequency dependent real part of the phonon polariton wavevector, see the discussion in chapter 8.

The coupling to defect modes, which were previously inferred for example by Schwarz and Maier [42], is included in the description of the observed sub-structure of the frequency-dependent damping rate. The measured data can be recalculated in order to obtain the imaginary part of the phonon polariton wavevector, Im(q), using equation 9.3. In figure 9.5a, Im(q) is shown as function of frequency by the red dots.

The calculated imaginary part of the wavevector is shown by the violet and green lines, respectively. The former one corresponds to the violet line in figure 9.3 and the latter one to the green line in figure 9.3. All data shown in figure 9.5a (red dots) are obtained using short probe pulses.

On the right hand side in figure 9.5b the real part of the measured (blue and violet dots) and simulated dispersion relation of the phonon polaritons is shown in the same way as in figure 8.5. As long as the time resolution is sufficient to resolve the frequency of the phonon polaritons, the ISRS experiment with short probe pulses yields both, the frequency and the damping of the impulsively excited phonon polaritons. Thus, the real and the imaginary parts of the dispersion relation are simultaneously mapped out, as shown in figures 9.5a and 9.5b.
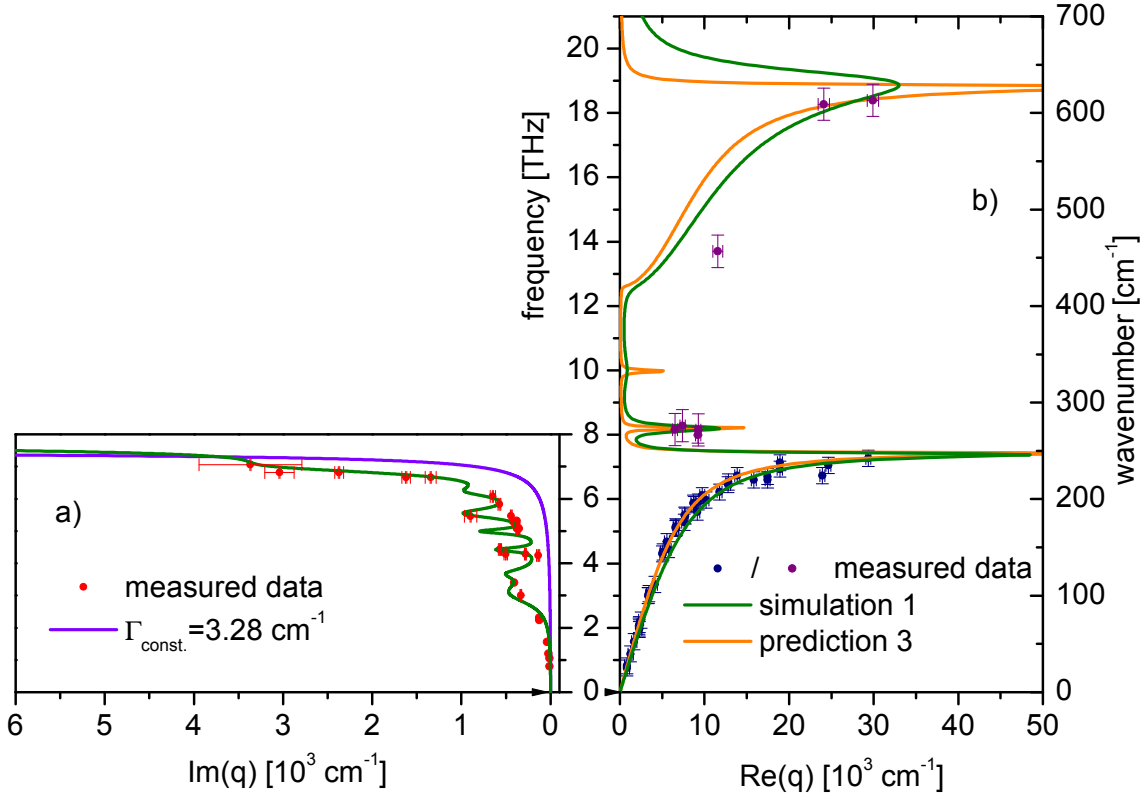
Figure 9.5: Complex dispersion relation of phonon polaritons as obtained in $LiNbO_3$ with ISRS. The frequency of the phonon polaritons is plotted versus the imaginary (a) and real part (b) of the phonon polariton wavevector q. The red, violet, and blue dots are obtained with temporally short, narrow bandwidth, and with temporally short as well as with narrow bandwidth probe pulses, respectively. Purple line: calculated damping γ_{pp} of phonon polaritons assuming a dielectric function (Eq.: 9.1) with parameters that are obtained in this work from the fit procedure of the data shown in b). Green line (in (a)) shows the calculation where additionally the coupling of the mechanical part of the phonon polaritons to low-frequency defect modes [42] is taken into account. The orange line is a model using parameters from a infrared reflectivity measurement [27] but with ten times smaller damping rates $\Gamma_i = 1/10 \cdot \Gamma_{IR}$ according to Barker and Loudon [6]. The simulation of the real part of the dispersion relation is shown as the green line in b). The optimized parameters are listed in the third column of table 8.1.

In this work, the time resolution is sufficient to study the lower dispersion branch of phonon polaritons in $LiNbO_3$. In figure 9.5b, the obtained data that describe the lower branch of the phonon polariton dispersion relation are measured with both, narrow bandwidth and temporally short probe pulses, and are shown by the blue dots. Further, the fit-analysis of the real part of the dispersion relation yields a TO phonon damping constant of $\Gamma_1 = 3.28$ cm^{-1}, which is significantly smaller than the damping constants which were measured by infrared reflectivity and Raman

scattering experiments. The measured frequency-dependent damping rate or the imaginary part of the phonon polariton wavevector is well-described using the same $\Gamma_1 = 3.28$ cm^{-1}. This is an additional prove for the determined damping rate of the TO phonon.

Using narrow bandwidth probe pulses measures and confirms the frequency of higher lying modes, which exhibit a frequency higher than 7.5 THz and are shown by the violet dots in figure 9.5b. The dispersion relation is subsequently extended to higher frequencies, where three additional phonon modes have to be taken into account. Thus, a full picture of the real part of the dispersion relation is obtained as shown in figure 9.5b.

10 Outlook

This chapter consists of two parts. In the first part preliminary ISRS experiments in ferroelectric LiTaO$_3$ are discussed. The findings are compared with other ISRS studies of phonon polaritons in LiTaO$_3$ and further ISRS experiments are suggested. In the second part, an experiment composed of femtosecond optical excitation and subsequent hard X-ray probing of coherent phonon polariton wavepackets is proposed. This approach allows the direct monitoring of the lattice dynamics on femtosecond timescales with sub-nanometer resolution.

10.1 Phonon Polaritons in LiTaO$_3$

The implementation of temporally short laser pulses for the excitation of the phonon polaritons in the transient grating geometry enables a wavevector-selective and coherent generation of polariton modes. The detection of the polaritons with narrow band pulses permits an unambiguous assignment of the frequencies of the observed modes. This is particularly important if several modes, which belong to different branches of the dispersion relation, are simultaneously excited because all possess the same wavevector magnitude, which is within the bandwidth of the pump laser beams. Furthermore, if the probe pulses are temporally short, the Raman scattered light from different modes would be incident on the same pixel of the spectrometer and thus these fields would interfere. The interpretation of such a resulting transient intensity may be difficult. But in case of narrow bandwidth probe pulses, the Raman scattered fields would be detected by different pixels, because the frequency shifts are different and thus no interference is expected.

In addition to the wavevector selectivity, the frequency selectivity is achieved through inserting narrow bandpass filters with different central wavelengths into the path of the first and second laser pump pulse, as described in section 7.1 for the case of LiNbO$_3$. The same experiment is repeated for a LiTaO$_3$ sample. Like LiNbO$_3$, LiTaO$_3$ is a well-known ferroelectric material [125] and exhibits non-linear optical properties. Its phononic and polaritonic behavior was intensively characterized by Raman scattering [19,126,127], forward Raman scattering [75], reflectivity measurements [107], and in the time-domain by ISRS experiments [47,48,55,79,81,83,91,117,128,129].

In the following, an exemplary measurement of the phonon polaritons in LiTaO$_3$ using the transient grating geometry is presented. This experiment shows that the wavevector and frequency selectivity of the transient grating geometry allows us to detect even very weak polariton modes

as they appear in LiTaO$_3$. The diffracted spectrum, obtained for time-delays for which the phonon polaritons are still within the probe volume, is shown in figure 10.1. The intersection angle Θ of the pump pulses was tuned such that a wavevector of $q_R = 3927$ cm^{-1} is excited. The spectra of the pump pulses were already depicted in figure 7.1b. The energy difference of the central wavelengths (795 nm and 810 nm) of the pump pulses corresponds to a frequency of $\omega = 6.5 \pm 2.5$ THz. Three intensity maxima indicate modes of phonon polaritons with the
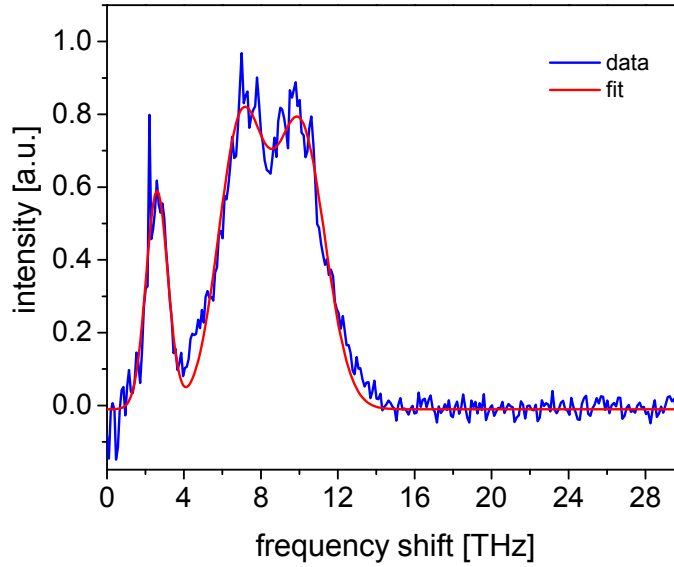

Figure 10.1: The blue line shows the spectrum of Raman scattered light from a selectively prepared phonon polariton with the wavevector magnitude of $q_R = 3927$ cm^{-1} in LiTaO$_3$. The spectra of the pump laser pulses, $\mathbf{k}_1$ and $\mathbf{k}_2$, with their center wavelengths of 795 nm and 810 nm are shown in figure 7.1b. The frequency difference of the maxima of the spectra of the pump pulses corresponds to $\Delta\omega = 6.5 \pm 2.5$ THz. The measurement is performed with narrow band probe pulses with a width of 2 nm. Besides the phonon polariton in the lower dispersion branch ($\omega_{pp} = 2.6$ THz), scattering from two other modes is visible by the peaks centered at 7.0 THz and 10 THz. The red line shows a fit to the data by a Gaussian function. The determined FWHM is 1.3 THz, 3.0 THz, and 3.2 THz, respectively.

frequency 2.6 THz, 7.0 THz, and 10 THz, respectively. The lowest frequency corresponds to a mode of the lowest polariton branch, which is not efficiently excited, because the frequency difference of the pump pulses is too large (~ 6.5 THz). This increases the visibility of the higher frequency modes, which would otherwise be covered by the low frequency mode.

The TO modes in LiTaO$_3$ have the resonance frequencies of $\omega_{TO,2} = 7.5$ THz, $\omega_{TO,3} = 10.7$ THz, and $\omega_{TO,4} = 18$ THz, as reported in references [107, 126]. Crimmins *et al.* deduce from an ISRS study [7] several phonon branches with the frequencies of 7.5 THz, 11.5 THz, and 13.0 THz. The

present experiment, however, does not show any signature of a branch at 13.0 THz (figure 10.1), because we selectively excite at 6.5 THz. For the same reason, no intense peaks are observed in the transient spectrum of LiTaO$_3$ for frequencies which are larger than $\omega = 10$ THz. In the future, the discrepancy of the data reported by Crimmins *et al.* [7] and the measured data in this work may be clarified by further measurements with narrow band probe pulses.
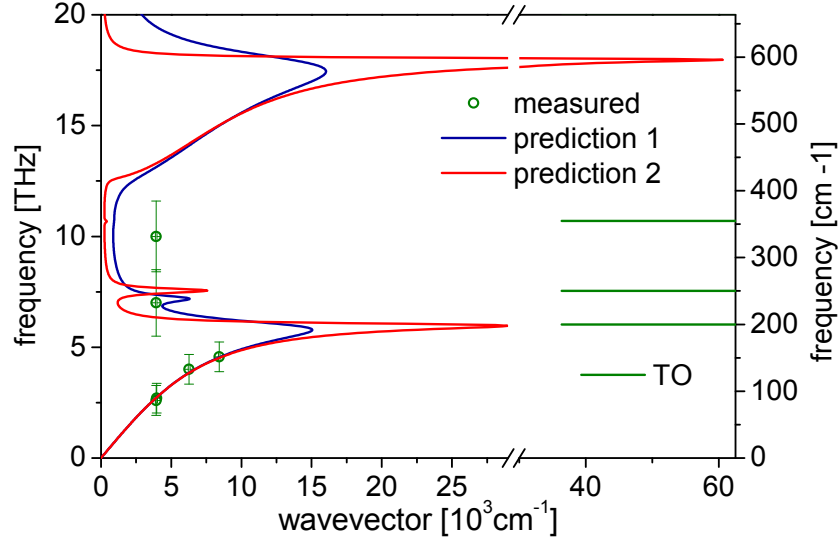

Figure 10.2: Dispersion relation of phonon polaritons in LiTaO$_3$. Data obtained with short probe pulses and with narrow band probe pulse are shown by the green open circles. Three lower TO phonon modes as observed in other experiments (see text) are indicated by the green lines. The predicted dispersion relation is calculated with equation 8.1 and parameters as obtained from the Raman scattering experiment [126] (red line) and the infrared reflectivity study [107] (blue line). Parameters are listed in table 10.1.

In figure 10.2, a few measured points of the dispersion relation of phonon polaritons in LiTaO$_3$ are shown. Two theoretical dispersion curves are calculated using equation 8.1 and parameters determined from an infrared reflectivity experiment [107] and from a Raman scattering experiment [126]. They are shown by the red and blue lines in figure 10.2, respectively. The parameters are given in table 10.1. In the lower part of the dispersion relation both calculations describe the experimental data from this thesis equally well. The second branch is observed at the frequency of 7.59 THz (253 cm^{-1}) by the Raman experiment [126] and at 7.23 THz (241 cm^{-1}) by the reflectivity experiment [107]. The Raman value for the spectral line position can vary by about 0.15 THz, depending on the exact stoichiometry and purity of the sample. Thus both predictions are consistent with the data point at 7.0 THz. The detected frequency of

i	υ cm^{-1} (THz)	γ cm^{-1}	S	υ cm^{-1} (THz)	γ cm^{-1}
1	200 (6.0)	30	28	201 (6.0)	10
2	241 (7.2)	2	30	253 (7.6)	0.64
3	357 (10.7)	0.005	11	356 (10.7)	0.18
4	596 (17.9)	2.66	18	600 (18.0)	3.2
5	657 (19.7)	0.34	56		
	ϵ_∞	= 4.527			

Table 10.1: Room-temperature central frequency υ, linewidth γ, and absorption strength, S, of the four (five) TO phonons in LiTaO$_3$ which are polarized parallel to the c-axis. First column: parameters are obtained with the reflectivity study reported in [107]. Second column: parameters are obtained from the Raman scattering experiment reported in [126].

10 THz can be assigned to the third TO mode of LiTaO$_3$ with the frequency 10.7 THz. Both model calculations fail to describe this data point.

It is worth to note that in this case one would gain no information from a more detailed data fitting analysis, because of the lack of data points. In summary, these first measurements confirm the theoretical dispersion relation of the phonon polaritons of the lower dispersion branch in LiTaO$_3$. Moreover, some of the previously observed higher lying branches are confirmed by the present experiment. No clear signature of polariton modes were found at 13 THz, which is in contradiction to the previous report by Crimmins *et al.* [7].

10.2 UXRD View on Phonon Polaritons

As already discussed in this thesis, phonon polaritons are quasi-particles that consist of a mixture of electromagnetic wave and transverse optical lattice mode. The proportion of the lattice part and electromagnetic wave of the excited phonon polariton depends on the frequency and on the wavevector of the quasi-particle. A standard all-optical pump-probe spectroscopy experiment cannot determine this ratio, which thus remains an open question. However, a time-resolved experiment that is sensitive to the lattice part of the phonon polariton could separate the lattice and the electromagnetic field part of the phonon polariton. A suitable experimental method for this question is ultrafast hard X-ray diffraction (UXRD). Since X-ray diffraction in the hard X-ray regime is predominantly sensitive to the lattice structure, the amplitude of a vibrational lattice mode and consequently the stored energy in the mechanical part of the excited mode can be determined.

To follow the ultrafast lattice dynamics caused by phonon polaritons and more general by optical phonons in time domain, one has to use short X-Ray pulses that are shorter than the time of one oscillation of the lattice vibration. In the case of the phonon polaritons the relevant time scale is of the order of sub-picoseconds. Due to the technical challenges related to such an experiment, only one report on this topic has been published so far. This experiment on coherent phonon polaritons in LiTaO$_3$ was performed by Cavalleri *et al.* [130]. A broad frequency spectrum of phonon polaritons was excited by a single femtosecond laser pulse and subsequently probed by X-ray pulses derived from the femto-slicing [131] beam line at the synchrotron storage ring at the Advanced Light Source, Berkely, USA. The measured maximum amplitude of the mode was relatively small ($u = 0.005$ Å). This is caused by the distribution of the the laser pulse energy between between the broad spectral components of generated phonon polaritons. Each of these modes induces only small transient lattice changes. Because of this very challenging experimental conditions, this experiment has not been reproduced by other groups, yet. One possibility to gain a larger amplitude of the lattice mode would be to excite the phonon polaritons by the wavevector-selective excitation. This will lead to an excitation of a very narrow mode, but with a relatively high amplitude in comparison to the excitation with a single incident laser pulse, as was done by Cavalleri. Moreover, the generated spectrum of the phonon polaritons in the case of the wavevector-selective excitation is much sharper. Thus, the expected transient modulation could easily be simulated. In contrast, the oscillation frequency (1.5 THz) as determined by Cavalleri has to be met with caution. It is the central frequency of a very broad spectrum.

Obviously, small transient lattice changes induced by coherent phonon polaritons require high fluxes of the X-Ray source for their detection. Therefore, measuring the frequency-dependent vibrational amplitude of the lattice part of the phonon polariton a free electron laser (FEL) [132] is likely to be most appropriate. In principle, such a measurement is possible at plasma X-ray

sources (PXS) [133–136] and femto-slicing beam lines [131, 137], but the number of photons is relatively low in this cases ($N_{femto} = 2 \cdot 10^6$ s^{-1} and $N_{PXS} = 5 \cdot 10^6$ s^{-1} (on the sample)), which will require long integration times to resolve relative changes of the diffraction efficiency of the order of $\Delta a/a_0 = 1 - 5 \cdot 10^{-3}$ [130]. Moreover, PXS and femto-slicing beam lines [131, 137] exhibit a temporal resolution of $100 - 200$ fs. This sets a limitation for the observation of frequencies of phonon polaritons of about $2 - 2.5$ THz. However, the temporal duration of the FEL pulses is of the order of 10 fs. Certainly, the jitter in the arrival time of the FEL probe pulse and laser pump pulse is typically much larger and amounts to 100-200 fs. The most recent experiments show, that the arrival time of each pulse can be measured with an temporal uncertainty of ~ 40 fs [138], which sets the limit for the temporal resolution in the UXRD experiment at the FEL. Further, the energy of the PXS source is not easily tunable but relies on a certain medium (e.g. copper) to generate X-rays with a characteristic energy. In this case, some of the Bragg reflections that are sensitive to the transient lattice changes, are not accessible. One has to consider that the phonon polariton mode is associated with an oscillation of the differently charged ions within the structural unit cell. The generation of a phonon polariton hence results in a transient modulation of the structure factor, which defines the intensity of the diffraction peak [32]. This is true, as long as the scattering wavevector has a component along the direction of the atomic motion. With the know-how of the selective excitation of the narrow band modes of phonon polaritons in non-linear crystals that have been accumulated in this work, an experiment at a FEL seems to be feasible for determining the lattice part of the phonon polariton mode: the dependency of the vibrational amplitude on the frequency and the optical pump intensity could be studied. A simultaneous measurement of the generated terahertz fields would enable us to disentangle the vibrational and the electromagnetic part of the impulsively generated phonon polaritons. This could in turn provide new insight into the elementary generation process of phonon polaritons and will be of great interest for the generation of intense and ultra-short terahertz pulses via optical rectification in polar non-linear crystals.

A Appendix

A.1 Calculation of the Transient Diffracted Intensity

In chapter 5 the homodyne detection of two counter-propagating phonon polaritons with a variably delayed probe pulse is derived for the case of the energy-resolved detection scheme, where a spectrometer is used to detect the transient diffracted intensity. In the following, equation 5.7

$$I_{sig} = |E_+ + E_- + E_{el}|^2 \tag{A.1}$$

sis explicitly evaluated for the case where all three field amplitudes, namely the Stokes field E_-, the anti-Stokes field E_+, and the Rayleigh field E_{el}, contribute to the detected intensity I_{sig}. The fields have the form

$$E_- = E_{-,0} \cdot e^{-\gamma\tau} \cdot e^{i(\omega_4 t - \omega_{pp}\tau - \pi/2)} \tag{A.2}$$

$$E_+ = E_{+,0} \cdot e^{-\gamma\tau} \cdot e^{i(\omega_4 t + \omega_{pp}\tau + \pi/2)} \tag{A.3}$$

$$E_{el} = E_{el,0} \cdot e^{i\omega_4 t} \quad , \tag{A.4}$$

where ω_4 is an arbitrary frequency which is detected by a single pixel of a spectrometer, τ is the delay-time between pump and probe pulses, γ is the damping rate of phonon polaritons, and the factors $-\pi/2$, $+\pi/2$ represent the phase shift that originates by Stokes or anti-Stokes scattering of light, respectively. Now, equation A.1 is evaluated:

$$\begin{aligned} I_{sig} =& (E_+ + E_- + E_{el}) \cdot (E_+^* + E_-^* + E_{el}^*) \\ \Rightarrow& E_+ E_+^* + E_- E_-^* + E_{el} E_{el}^* \ + \ E_+ E_-^* + E_- E_+^* \ + \ E_{el}(E_+^* + E_-^*) + E_{el}^*(E_+ + E_-). \end{aligned} \tag{A.5}$$

All individual terms of the sum can be calculated. The first three terms yield the contribution

$$I_a = E_{el,0}^2 + (E_{+,0}^2 + E_{-,0}^2)e^{-2\gamma\tau} = I_{el,0} + (I_{+,0} + I_{-,0})e^{-2\gamma\tau} \quad . \tag{A.6}$$

The term $I_{el,0}$ yilds a constant offset and the second term shows no oscillatory behavior and decays exponentially with 2γ. The next two terms in equation A.5, where the Stokes (-) and the anti-Stokes (+) fields are multiplied, yield

$$
\begin{aligned}
I_b &= E_{+,0}E_{-,0}e^{-2\gamma\tau}e^{i(-2\omega_{pp}\tau-2\pi/2)} + E_{-,0}E_{+,0}e^{-2\gamma\tau}e^{i(2\omega_{pp}\tau+2\pi/2)} \\
&\Rightarrow I_{\pm}e^{-2\gamma\tau}(e^{i(-2\omega_{pp}\tau-\pi)} + e^{i(2\omega_{pp}\tau+\pi)}) \\
&\Rightarrow 2\cdot I_{\pm}e^{-2\gamma\tau}\cos(2\omega_{pp}\tau+\pi) = -2\cdot I_{\pm}e^{-2\gamma\tau}\cos(2\omega_{pp}\tau) \ .
\end{aligned}
\tag{A.7}
$$

This intensity oscillates with $2\omega_{pp}$ and decays with 2γ. The evaluation of the last terms in equation A.5 leads to the contribution

$$
\begin{aligned}
I_c &= (E_{0,el}E_{-,0}e^{i(\omega_{pp}\tau+\pi/2)} + E_{-,0}E_{0,el}e^{i(-\omega_{pp}\tau-\pi/2)})e^{-\gamma\tau} \\
&\quad + (E_{0,el}E_{+,0}e^{i(-\omega_{pp}\tau-\pi/2)} + E_{+,0}E_{0,el}e^{i(+\omega_{pp}\tau+\pi/2)})e^{-\gamma\tau}
\end{aligned}
\tag{A.8}
$$

$$
\Rightarrow 2I_{el,-}e^{-\gamma\tau}\cos(\omega_{pp}\tau+\pi/2) + 2I_{el,+}e^{-\gamma\tau}\cos(\omega_{pp}\tau+\pi/2) \ .
$$

For the case $E_{-,0} = E_{+,0}$, equation A.8 simplifies to:

$$
I_c = 4I_{el,\pm}e^{-\gamma\tau}\cos(\omega_{pp}\tau+\pi/2) = -4I_{el,\pm}e^{-\gamma\tau}\sin(\omega_{pp}\tau) \ .
\tag{A.9}
$$

This expression shows, that the intensity I_c decays exponentially with γ and exhibits a modulation with ω_{pp}. The total transient detected intensity $I_{sig} = I_a + I_b + I_c$ shows different temporal evolution depending on the ratio of the filed amplitudes $E_{+,0}$, $E_{-,0}$, and $E_{el,0}$. In the following the different cases, that are examined in this work, are discussed in detail:

Negligible elastic field regime

Here, the Rayleigh field is much smaller than the Stokes and anti-Stokes fields, $E+,0 \approx E-,0 \gg E_{el,0}$, hence

$$
I = 2\cdot I_{\pm}e^{-2\gamma\tau}(1-\cos(2\omega_{pp}\tau)) = 4\cdot I_{\pm}e^{-2\gamma\tau}\sin^2(\omega_{pp}\tau) \ .
\tag{A.10}
$$

Local oscillator field

In this case, the Rayleigh field is much larger than the Stokes and anti-Stokes fields, $E+,0 \approx E-,0 \ll E_{el,0}$, thus

$$
I = I_{el,0} - 4I_{el,\pm}e^{-\gamma\tau}\sin(\omega_{pp}\tau) \ .
\tag{A.11}
$$

Increased elastic field contribution

This is the case where all three fields have approximately the same amplitudes: $E+, 0 \approx E-, 0 \approx E_{el,0}$, which finally leads to

$$I = I_{el,0} - 4I_{el,\pm}e^{-\gamma\tau}\sin(\omega_{pp}\tau) + 2 \cdot I_{\pm}e^{-2\gamma\tau}(1 - \cos(2\omega_{pp}\tau)) \tag{A.12}$$

$$= I_{el,0} - 4I_{el,\pm}e^{-\gamma\tau}\sin(\omega_{pp}\tau) + 4 \cdot I_{\pm}e^{-2\gamma\tau}\sin^2(\omega_{pp}\tau) \quad .$$

Displaced probe region

For the case where only one phonon polariton reaches the observation area, the field which would be diffracted from the other wavepacket is set to zero ($E_+ = 0$, $E+, 0 \approx E_{el,0}$):

$$I = I_{el,0} - 2I_{el,-}e^{-\gamma\tau}\sin(\omega_{pp}\tau) + I_{-,0}e^{-2\gamma\tau} \quad . \tag{A.13}$$

A.2 Overlap Integral of the Gaussian Envelope Functions

For the calculation of the effective overlap of the probe volume with the generated wavepacket of the phonon polariton let us assume that the envelopes of both, the probe beam and the polariton wavepacket can be described by Gaussian functions with approximately the same widths. We begin with the solution of two useful integrals, namely the integral over the Gaussian function and over the square of the same Gaussian function:

$$\int_{-\infty}^{\infty} e^{-\frac{x^2}{\sigma^2}} = \sqrt{\pi}\sigma \tag{A.14}$$

$$\int_{-\infty}^{\infty} e^{-2\frac{x^2}{\sigma^2}} = \sqrt{\frac{\pi}{2}}\sigma \tag{A.15}$$

The latter integral describes the situation where the pump and probe volumes are equal and overlap perfectly. Next, one of the Gaussian functions is displaced with respect to the first one by a spatial distance l. This overlap integral has the following solution:

$$E(x) = \int_{-\infty}^{\infty} e^{-\frac{x^2}{\sigma^2}} e^{-\frac{(l-x)^2}{\sigma^2}} = \sqrt{\frac{\pi}{2}}\sigma e^{-\frac{l^2}{2\sigma}} \quad . \tag{A.16}$$

A normalized expression is obtained if one divides equation A.16 by A.15. Assuming that the relative decrease of the scattered field amplitude is $1/e$ the expression for characteristic distance l can be derived according to

$$\frac{1}{e} = e^{-\frac{l^2}{2\sigma}} \Rightarrow l = \sqrt{2}\sigma \Rightarrow l = \frac{FWHM}{\sqrt{2\ln 2}} \quad . \tag{A.17}$$

To relate equation A.17 with the group velocity v_g of phonon polaritons, the assumptions $v_{rel} = v_g \cos\beta$ and $l = v_g \cos\beta \cdot \tau_{\frac{1}{e}}$ have to be made, which define the relative velocity v_{rel} of the polariton wavepacket with respect to the wavevector k of the probe light and defines the relation between the characteristic distance l and lifetime of phonon polaritons. The expression for $\cos\beta$ was already derived in section 2.21 and has the form $\cos\beta = (1 - \frac{n_l^2}{n_{THz}^2})^{0.5}$. The lifetime $\tau_{\frac{1}{e}}$ is then calculated from

$$\tau_{\frac{1}{e}} = \frac{\sigma}{\sqrt{2}\frac{1}{v_g \cos\beta}} \tag{A.18}$$

and the characteristic damping rate is given by

$$\gamma_v = \frac{1}{\tau_{\frac{1}{e}}} \quad . \tag{A.19}$$

In the measurement, this damping rate γ_v adds to the natural polariton damping rate γ_{pp}. Especially for small wavevectors, where γ_{pp} is relatively small and the group velocity v_g is relatively high, one has take this effect into account. The calculated damping rate γ_v is shown for two different diameters of the laser beams in figure A.1.
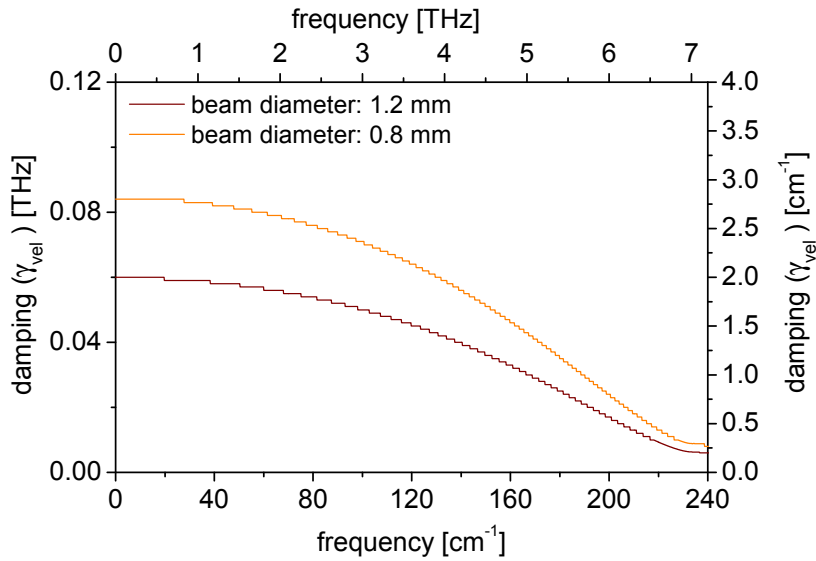

Figure A.1: Calculated damping rate γ_v using equations A.19 and A.18 for the case of two the laser beams with diameter ~ 0.8 mm (orange line) and ~ 1.2 mm (brown line), respectively.

Abbreviations

DFG	Difference Frequency Generation
fs	femtosecond
FROG	Frequency Resolved Optical Gating
gr	group
IR	Infrared
ISRS	Impulsive Stimulated Raman Scattering
PP	Phonon Polariton
SFG	Sum Frequency Generation
SHG	Second Harmonic Generation
sig	signal
TG	transient grating
TO	transverse optical
UXRD	Ultrafast X-Ray Diffraction

Bibliography

[1] Henry, C. H. and Hopfield, J. J. *Raman scattering by polaritons.* Phys. Rev. Lett., vol. 15: 964–966, 1965.

[2] Huang, K. *Lattice vibrations and optical waves in ionic crystals.* Nature, 1951.

[3] Huang, K. *On the interaction between the radiation field and ionic crystals.* Proceedings of the Royal Society of London. Series A. Mathematical and Physical Sciences, vol. 208(1094): 352–365, 1951.

[4] Loudon, R. *The Raman effect in crystals.* Advances in Physics, vol. 13(52): 423 — 482, 1964.

[5] Scott, J. F. *Light scattering from polaritons.* American Journal of Physics, vol. 39(11): 1360–1372, 1971.

[6] Barker, A. S. and Loudon, R. *Response functions in the theory of Raman scattering by vibrational and polariton modes in dielectric crystals.* Rev. Mod. Phys., vol. 44(1): 18–47, 1972.

[7] Crimmins, T. F., Stoyanov, N. S. and Nelson, K. A. *Heterodyned impulsive stimulated Raman scattering of phonon–polaritons in LiTaO3 and LiNbO3.* The Journal of Chemical Physics, vol. 117(6): 2882–2896, 2002.

[8] Hebling, J., Yeh, K.-L., Hoffmann, M. C., Bartal, B. and Nelson, K. A. *Generation of high-power terahertz pulses by tilted-pulse-front excitation and their application possibilities.* J. Opt. Soc. Am. B, vol. 25(7): B6–B19, 2008.

[9] Hoffmann, M. C. and Fülöp, J. A. *Intense ultrashort terahertz pulses: generation and applications.* Journal of Physics D: Applied Physics, vol. 44(8): 083001, 2011.

[10] Rullière, C. H. . (editor). *Femtosecond Laser Pulses : Principles and Experiments*, (Springer, New York;[Heidelberg]2005), 2nd ed. Includes index. - Previous ed.: 1998; hbk.. - : £54.00.

[11] Diels, W., Jean-Claude ; Rudolph. *Ultrashort Laser Pulse Phenomena : Fundamentals, Techniques and Applications on a Femtosecond Time Scale*, (Academic Press, Amsterdam, Heidelberg [u.a.]2006), 2nd ed.

[12] Ballman, A. A. *Growth of piezoelectric and ferroelectric materials by the Czochralski technique.* Journal of the American Ceramic Society, vol. 48(2): 112–113, 1965.

[13] Abrahams, S. C., Levinstein, H. J. and Reddy, J. M. *Ferroelectric lithium niobate. 5. Polycrystal X-ray diffraction study between 24 and 1200 C.* Journal of Physics and Chemistry of Solids, vol. 27(6–7): 1019 – 1026, 1966.

[14] Abrahams, S. C., Reddy, J. M. and Bernstein, J. L. *Ferroelectric lithium niobate. 3. Single crystal X-ray diffraction study at 24C.* Journal of Physics and Chemistry of Solids, vol. 27(6–7): 997 – 1012, 1966.

[15] Subarao, E. C. *Soft Modes in Ferroelectrics and Antiferroelectrics*, (E.C. Subarao, North-Holland, Amsterdam1974).

[16] Nassau, K. and Levinstein, H. J. *Ferroelectric behavior of lithium niobate.* Applied Physics Letters, vol. 7(3): 69–70, 1965.

[17] Bergman, J. G., Ashkin, A., Ballman, A. A., Dziedzic, J. M., Levinstein, H. J. and Smith, R. G. *Curie temperature, birefringence, and phasematching temperature variations in LiNbO3 as a function of melt stoichiometry.* Applied Physics Letters, vol. 12(3): 92–94, 1968.

[18] Weis, R. S. and Gaylord, T. K. *Lithium niobate: Summary of physical properties and crystal structure.* Applied Physics A, vol. 37: 191–203, 1985.

[19] Johnston, W. D. and Kaminow, I. P. *Temperature dependence of Raman and Rayleigh scattering in LiNbO3 and LiTaO3.* Phys. Rev., vol. 168: 1045–1054, 1968.

[20] Dhar, A. and Mansingh, A. *Optical properties of reduced lithium niobate single crystals.* Journal of Applied Physics, vol. 68(11): 5804–5809, 1990.

[21] Hobden, M. V. and Warner, J. *The temperature dependence of the refractive indices of pure lithium niobate.* Physics Letters, vol. 22(3): 243 – 244, 1966.

[22] Boyd, R. W. *Nonlinear Optics*, (Elsevier Academic Press, Amsterdam2008), 3rd ed.

[23] Wu, Q. and Zhang, X. C. *Ultrafast electrooptic field sensors.* Applied Physics Letters, vol. 68(12): 1604–1606, 1996.

[24] Kien, D. P., Loulergue, J. C. and Etchepare, J. *Nonlinear response to polariton waves driven in perovskites by femtosecond pulses.* Optics Communications, vol. 101(1–2): 53 – 59, 1993.

[25] Johnston, W. D. and Kaminow, I. P. *Contributions to optical nonlinearity in GaAs as determined from Raman scattering efficiencies.* Phys. Rev., vol. 188: 1209–1211, 1969.

[26] Boyd, G. D. and Pollack, M. A. *Microwave nonlinearities in anisotropic dielectrics and their relation to optical and electro-optical nonlinearities.* Phys. Rev. B, vol. 7: 5345–5359, 1973.

[27] Barker, A. S. and Loudon, R. *Dielectric properties and optical phonons in LiNbO3.* Phys. Rev., vol. 158: 433–445, 1967.

[28] Ridah, A., Fontana, M. D. and Bourson, P. *Temperature dependence of the Raman modes in LiNbO3 and mechanism of the phase transition.* Phys. Rev. B, vol. 56: 5967–5973, 1997.

[29] Kuzmany, H. *Solid-state Spectroscopy - an Introduction*, (Springer Verlag, Berlin2009), 2nd ed.

[30] Born, M. and Huang, K. *Dynamical theory of crystal lattices*, (Oxford University Press, Loudon1956), 1st ed.

[31] Gross, R. and Marx, A. *Festkörperphysik*, (Oldenbourg Wissenschaftsverlag, Berlin, Boston2012), 2nd ed.

[32] Kittel, C. *Introduction to Solid State Physics*, (Wiley, New York [u.a.]1996), 7th ed.

[33] Ashcroft, N. D. and Mermin, N. W. *Solid state physics*, (Saunders College, Fort Worth1976), 1st ed.

[34] Carcione, J. M., Gei, D. and Treitel, S. *The velocity of energy through a dissipative medium.* Geophysics, vol. 75(2): T37–T47, 2010.

[35] Gerasik, V. and Stastna, M. *Complex group velocity and energy transport in absorbing media.* Phys. Rev. E, vol. 81: 056602, 2010.

[36] Loudon, R. *The propagation of electromagnetic energy through an absorbing dielectric.* J. Phys. A, vol. 3(3): 233–245, 1970.

[37] Eichler, H. J., Günter, P. and Pohl, D. W. *Laser Induced Dynamic Gratings*, vol. 50 of *Springer series in optical sciences*, (Springer, Berlin [u.a.]1986).

[38] Yan, Y., Gamble, E. B. and Nelson, K. A. *Impulsive stimulated scattering: General importance in femtosecond laser pulse interactions with matter, and spectroscopic applications.* The Journal of Chemical Physics, vol. 83(11): 5391–5399, 1985.

[39] Yan, Y.-X. and Nelson, K. A. *Impulsive stimulated light scattering. I. General theory.* The Journal of Chemical Physics, vol. 87(11): 6240–6256, 1987.

[40] Yan, Y.-X. and Nelson, K. A. *Impulsive stimulated light scattering. II. Comparison to frequency-domain light-scattering spectroscopy.* The Journal of Chemical Physics, vol. 87(11): 6257–6265, 1987.

[41] Yarborough, J. M., Sussman, S. S., Purhoff, H. E., Pantell, R. H. and Johnson, B. C. *Efficient, tunable optical emission from LiNbO3 without a resonator.* Applied Physics Letters, vol. 15(3): 102–105, 1969.

[42] Schwarz, U. T. and Maier, M. *Damping mechanisms of phonon polaritons, exploited by stimulated Raman gain measurements.* Phys. Rev. B, vol. 58: 766–775, 1998.

[43] Brennan, C. J. *Femtosecond wavevector overtone spectroscopy of anharmonic lattice dynamics in ferroelectric crystals.* Ph.D. thesis, MIT, 1997.

[44] Hebling, J. *Determination of the momentum of impulsively generated phonon polaritons.* Phys. Rev. B, vol. 65: 092301, 2002.

[45] Wahlstrand, J. K. and Merlin, R. *Cherenkov radiation emitted by ultrafast laser pulses and the generation of coherent polaritons.* Phys. Rev. B, vol. 68: 054301, 2003.

[46] Planken, P. C. M., Noordam, L. D., Kennis, J. T. M. and Lagendijk, A. *Femtosecond time-resolved study of the generation and propagation of phonon polaritons in LiNbO3.* Phys. Rev. B, vol. 45: 7106–7114, 1992.

[47] Auston, D. H., Cheung, K. P., Valdmanis, J. A. and Kleinman, D. A. *Cherenkov radiation from femtosecond optical pulses in electro-optic media.* Phys. Rev. Lett., vol. 53: 1555–1558, 1984.

[48] Stepanov, A., Hebling, J. and Kuhl, J. *Generation, tuning, and shaping of narrow-band, picosecond THz pulses by two-beam excitation.* Opt. Express, vol. 12(19): 4650–4658, 2004.

[49] Hoffmann, M. C., Yeh, K.-L., Hebling, J. and Nelson, K. A. *Efficient terahertz generation by optical rectification at 1035 nm.* Opt. Express, vol. 15(18): 11706–11713, 2007.

[50] Faust, W. L. and Henry, C. H. *Mixing of visible and near-resonance infrared light in GaP.* Phys. Rev. Lett., vol. 17: 1265–1268, 1966.

[51] Mahajan, V. N. and Gaskill, J. D. *Doppler interpretation of the frequency shifts of light diffracted by sound waves.* Journal of Applied Physics, vol. 45(6): 2799–2800, 1974.

[52] Jackson, J. D. *Classical Electrodynamics*, (Wiley, New York [u.a.]1999), 3rd ed.

[53] Feurer, T., Stoyanov, N. S., Ward, D. W., Vaughan, J. C., Statz, E. R. and Nelson, K. A. *Terahertz Polaritonics.* Annual Review of Materials Research, vol. 37(1): 317–350, 2007.

[54] Feurer, T., Vaughan, J. C., Hornung, T. and Nelson, K. A. *Typesetting of terahertz waveforms.* Opt. Lett., vol. 29(15): 1802–1804, 2004.

[55] Feurer, T., Vaughan, J. C. and Nelson, K. A. *Spatiotemporal coherent control of lattice vibrational waves.* Science, vol. 299(5605): 374–377, 2003.

[56] Lin, K.-H., Werley, C. A. and Nelson, K. A. *Generation of multicycle terahertz phonon-polariton waves in a planar waveguide by tilted optical pulse fronts.* Applied Physics Letters, vol. 95(10): 103304, 2009.

[57] Hornung, T., Vaughan, J. C., Feurer, T. and Nelson, K. A. *Degenerate four-wave mixing spectroscopy based on two-dimensional femtosecondpulse shaping.* Opt. Lett., vol. 29(17): 2052–2054, 2004.

[58] Ward, D. W., Beers, J. D., Feurer, T., Statz, E. R., Nelson, K. A. and Stoyanov, N. S. *Coherent control of phonon-polaritons in a terahertz resonator fabricated with femtosecond laser machining.* Opt. Lett., vol. 29(22): 2671–2673, 2004.

[59] Salin, F., Piché, M. and Squier, J. *Mode locking of Ti:Al2O3 lasers and self-focusing: a Gaussian approximation.* Opt. Lett., vol. 16(21): 1674–1676, 1991.

[60] Brabec, T., Spielmann, C., Curley, P. F. and Krausz, F. *Kerr lens mode locking.* Opt. Lett., vol. 17(18): 1292–1294, 1992.

[61] Cerullo, G., Silvestri, S. D. and Magni, V. *Self-starting Kerr-lens mode locking of a Ti:sapphire laser.* Opt. Lett., vol. 19(14): 1040–1042, 1994.

[62] Cerullo, G., Silvestri, S. D., Magni, V. and Pallaro, L. *Resonators for Kerr-lens mode-locked femtosecond Ti:sapphire lasers.* Opt. Lett., vol. 19(11): 807–809, 1994.

[63] *Operator's Manual, Coherent Legend Elite*, 1st ed., 2008.

[64] Strickland, D. and Mourou, G. *Compression of amplified chirped optical pulses.* Optics Communications, vol. 55(6): 447 – 449, 1985.

[65] Mukamel, S. *Principles of Nonlinear Optics and Spectroscopy*, (Oxford University Press, New York1995), 1st ed.

[66] Maznev, A. A., Nelson, K. A. and Rogers, J. A. *Optical heterodyne detection of laser-induced gratings.* Opt. Lett., vol. 23(16): 1319–1321, 1998.

[67] Eckbreth, A. C. *BOXCARS: Crossed-beam phase-matched CARS generation in gases.* Applied Physics Letters, vol. 32(7): 421–423, 1978.

[68] Voehringer, P. and Scherer, N. F. *Transient grating optical heterodyne detected impulsive stimulated Raman scattering in simple liquids.* The Journal of Physical Chemistry, vol. 99(9): 2684–2695, 1995.

[69] Sweetser, J. N., Fittinghoff, D. N. and Trebino, R. *Transient-grating frequency-resolved optical gating.* Opt. Lett., vol. 22(8): 519–521, 1997.

[70] Polli, D., Brida, D., Mukamel, S., Lanzani, G. and Cerullo, G. *Effective temporal resolution in pump-probe spectroscopy with strongly chirped pulses.* Phys. Rev. A, vol. 82: 053809, 2010.

[71] Trebino, R., DeLong, K. W., Fittinghoff, D. N., Sweetser, J. N., Krumbügel, M. A., Richman, B. A. and Kane, D. J. *Measuring ultrashort laser pulses in the time-frequency domain using frequency-resolved optical gating.* Review of Scientific Instruments, vol. 68(9): 3277–3295, 1997.

[72] Porto, S. P. S., Tell, B. and Damen, T. C. *Near-forward Raman scattering in zinc oxide.* Phys. Rev. Lett., vol. 16: 450–452, 1966.

[73] Puthoff, H. E., Pantell, R. H., Huth, B. G. and Chacon, M. A. *Near-forward Raman scattering in LiNbO3.* Journal of Applied Physics, vol. 39(4): 2144–2146, 1968.

[74] Pinczuk, A., Burstein, E. and Ushioda, S. *Raman scattering by polaritons in tetragonal BaTiO3.* Solid State Communications, vol. 7(1): 139 – 142, 1969.

[75] Penna, A. F., Chaves, A., Andrade, P. d. R. and Porto, S. P. S. *Light scattering by lithium tantalate at room temperature.* Phys. Rev. B, vol. 13: 4907–4917, 1976.

[76] Kurtz, S. K. and Giordmaine, J. A. *Stimulated Raman scattering by polaritons.* Phys. Rev. Lett., vol. 22: 192–195, 1969.

[77] Charles, S. *Investigation of ultrafast phenomena in the femtosecond time domain.* Science, vol. 233(4770): 1276–1280, 1986.

[78] Auston, D. H. and Nuss, M. C. *Electrooptical generation and detection of femtosecond electrical transients.* Quantum Electronics, IEEE Journal of, vol. 24(2): 184–197, 1988.

[79] Wiederrecht, G. P., Dougherty, T. P., Dhar, L., Nelson, K. A., Leaird, D. E. and Weiner, A. M. *Explanation of anomalous polariton dynamics in LiTaO3.* Phys. Rev. B, vol. 51: 916–931, 1995.

[80] Etchepare, J., Grillon, G., Antonetti, A., Loulergue, J. C., Fontana, M. D. and Kugel, G. E. *Third-order nonlinear susceptibilities and polariton modes in PbTiO3 obtained by temporal measurements.* Phys. Rev. B, vol. 41: 12362–12365, 1990.

[81] Cheung, K. P. and Auston, D. H. *Excitation of coherent phonon polaritons with femtosecond optical pulses.* Phys. Rev. Lett., vol. 55: 2152–2155, 1985.

[82] Albert, O., Kien, D. P., Loulergue, J. C. and Etchepare, J. *Time-resolved phase deformation analysis of induced Kerr nonlinearities: application to phonon mode determination.* Optics Communications, vol. 114(3–4): 315 – 320, 1995.

[83] Dougherty, T. P., Wiederrecht, G. P. and Nelson, K. A. *Impulsive stimulated Raman scattering experiments in the polariton regime.* J. Opt. Soc. Am. B, vol. 9(12): 2179–2189, 1992.

[84] Landsberg, G. and Mandelstam, L. *Eine neue Erscheinung bei der Lichtzerstreuung in Krystallen.* Naturwissenschaften, vol. 16(28): 557–558, 1928.

[85] Raman, C. V. *The diamond.* Proc. Indian Acad. Sci. Sect., vol. A 44: 99, 1956.

[86] Raman, C. V. *A new radiation.* Indian J. Phys., vol. 2: 387, 1928.

[87] Raman, C. V. and Krishnan, K. S. *A new type of secondary radiation.* Nature, vol. 121, 1928.

[88] Goldshteyn, J., Bojahr, A., Gaal, P., Schick, D. and Bargheer, M. *Selective preparation and detection of phonon polariton wavepackets by stimulated Raman scattering.* Phys. Stat. Sol. B, 2013.

[89] Merlin, R. *Generating coherent THz phonons with light pulses.* Solid State Communications, vol. 102(2–3): 207 – 220, 1997. Highlights in Condensed Matter Physics and Materials Science.

[90] Kien, D. P., Loulergue, J. C. and Etchepare, J. *Phase-transition analysis through soft-phonon˘polariton behavior in the temporal domain: A_1-symmetry investigation of the* PbTiO$_3$ *perovskite.* Phys. Rev. B, vol. 47: 11027–11030, 1993.

[91] Bakker, H. J., Hunsche, S. and Kurz, H. *Observation of THz phonon-polariton beats in LiTaO3.* Phys. Rev. Lett., vol. 69: 2823–2826, 1992.

[92] Stoyanov, N. S., Ward, D. W., Feurer, T. and Nelson, K. A. *Terahertz polariton propagation in patterned materials.* Nat Mater, 2002.

[93] Werley, C. A., Nelson, K. A. and Tait, C. R. *Direct visualization of terahertz electromagnetic waves in classic experimental geometries.* American Journal of Physics, vol. 80(1): 72–81, 2012.

[94] Inoue, H., Katayama, K., Shen, Q., Toyoda, T. and Nelson, K. A. *Terahertz reflection response measurement using a phonon polariton wave.* Journal of Applied Physics, vol. 105(5): 054902, 2009.

[95] Inoue, H., Katayama, K., Shen, Q., Toyoda, T. and Nelson, K. A. *Comparative study of by near-field heterodyne transient grating and continuously variable spatial frequency transient grating methods for measurements of terahertz reflection responses.* Journal of Physics: Conference Series, vol. 214(1): 012123, 2010.

[96] Stoyanov, N. S., Feurer, T., Ward, D. W. and Nelson, K. A. *Integrated diffractive terahertz elements.* Applied Physics Letters, vol. 82(5): 674–676, 2003.

[97] Ward, D. W., Statz, E. R., Nelson, K. A., Roth, R. M. and Osgood, R. M. *Terahertz wave generation and propagation in thin-film lithium niobate produced by crystal ion slicing.* Applied Physics Letters, vol. 86(2): 022908, 2005.

[98] Stoyanov, N. S., Ward, D. W., Feurer, T. and Nelson, K. A. *Direct visualization of phonon-polariton focusing and amplitude enhancement.* The Journal of Chemical Physics, vol. 117(6): 2897–2901, 2002.

[99] Kojima, S., Kitahara, H., Nishizawa, S. and Wada Takeda, M. *Complex dispersion relation of phonon-polariton in stoichiometric LiNbO3.* Phys. Stat. Sol. C), vol. 1(11): 2674–2677, 2004.

[100] Kojima, S., Nishizawa, S., Kitahara, H. and Takeda, M. W. *Complex phonon-polariton dispersion of congruent lithium niobate studied by THz time-domain spectroscopy.* Ferroelectrics, vol. 314(1): 19–26, 2005.

[101] Rokni, M., Wall, L. S., Amzallag, E. and Chang, T. S. *Temperature study of the polariton associated with the 248 cm^{-1} soft mode in LiNbO3.* Solid State Communications, vol. 10(1): 103 – 105, 1972.

[102] Hopfield, J. J. *Proc. Int. Conf. on the Physics of Semiconductors.* J. Phys. Soc. Jpn. Suppl., vol. 21(77), 1966.

[103] Philipp, H. R. and Taft, E. A. *Optical constants of germanium in the region 1 to 10 Ev.* Phys. Rev., vol. 113: 1002–1005, 1959.

[104] Spitzer, W. G. and Kleinman, D. A. *Infrared lattice bands of quartz.* Phys. Rev., vol. 121: 1324–1335, 1961.

[105] Thomas, D. G. and Hopfield, J. J. *Exciton spectrum of cadmium sulfide.* Phys. Rev., vol. 116: 573–582, 1959.

[106] Barker, A. S. *Infrared lattice vibrations and dielectric dispersion in corundum.* Phys. Rev., vol. 132: 1474–1481, 1963.

[107] Barker, A. S., Ballman, A. A. and Ditzenberger, J. A. *Infrared study of thelattice vibrations in LiTaO3.* Phys. Rev. B, vol. 2: 4233–4239, 1970.

[108] S.L., D. *Terahertz Spectroscopy: Principles and Applications*, (edited by S.L. Dexheimer, New York, CRC Press,2008).

[109] Sakai, K. *Terahertz optoelectronics: an expanding field.* In *Infrared and Millimeter Waves, 2000. Conference Digest. 2000 25th International Conference on*, 3–4 (2000).

[110] Blanchard, F., Sharma, G., Razzari, L., Ropagnol, X., Bandulet, H.-C., Vidal, F., Morandotti, R., Kieffer, J., Ozaki, T., Tiedje, H., Haugen, H., Reid, M. and Hegmann, F. *Generation of intense terahertz radiation via optical methods.* Selected Topics in Quantum Electronics, IEEE Journal of, vol. 17(1): 5–16, 2011.

[111] Nagai, M., Matsubara, E. and Ashida, M. *High-efficiency terahertz pulse generation via optical rectification by suppressing stimulated Raman scattering process.* Opt. Express, vol. 20(6): 6509–6514, 2012.

[112] Rini, M., Tobey, R., Dean, N., Itatani, J., Tomioka, Y., Tokura, Y., Schoenlein, R. W. and Cavalleri, A. *Control of the electronic phase of a manganite by mode-selective vibrational excitation.* Nature, vol. 449(7158): 72–74, 2007.

[113] Hebling, J., Stepanov, A. G., Almási, G., Bartal, B. and Kuhl, J. *Tunable THz pulse generation by optical rectification of ultrashort laser pulses with tilted pulse fronts.* Applied Physics B: Lasers and Optics, vol. 78(5): 593–599, 2004.

[114] Yeh, K.-L., Hebling, J., Hoffmann, M. C. and Nelson, K. A. *Generation of high average power 1 kHz shaped THz pulses via optical rectification.* Optics Communications, vol. 281(13): 3567 – 3570, 2008.

[115] Schwarz, U. T. and Maier, M. *Frequency dependence of phonon-polariton damping in lithium niobate.* Phys. Rev. B, vol. 53: 5074–5077, 1996.

[116] Qiu, T. and Maier, M. *Long-distance propagation and damping of low-frequency phonon polaritons in LiNbO3.* Phys. Rev. B, vol. 56: R5717–R5720, 1997.

[117] Koehl, R. M., Adachi, S. and Nelson, K. A. *Direct visualization of collective wavepacket dynamics.* The Journal of Physical Chemistry A, vol. 103(49): 10260–10267, 1999.

[118] Ridah, A., Bourson, P., Fontana, M. D. and Malovichko, G. *The composition dependence of the Raman spectrum and new assignment of the phonons in LiNbO3.* Journal of Physics: Condensed Matter, vol. 9(44): 9687, 1997.

[119] Schlarb, U., Klauer, S., Wesselmann, M., Betzler, K. and Wöhlecke, M. *Determination of the Li/Nb ratio in lithium niobate by means of birefringence and Raman measurements.* Applied Physics A, vol. 56(4): 311–315, 1993.

[120] Wöhlecke, M., Corradi, G. and Betzler, K. *Optical methods to characterise the composition and homogeneity of lithium niobate single crystals.* Applied Physics B, vol. 63(4): 323–330, 1996.

[121] Dougherty, T. P., Wiederrecht, G. P., Nelson, K. A., Garrett, M. H., Jenssen, H. P. and Warde, C. *Femtosecond time-resolved spectroscopy of soft modes in structural phase transitions of perovskites.* Phys. Rev. B, vol. 50(13): 8996–9019, 1994.

[122] Okamoto, Y., Wang, P.-c. and Scott, J. F. *Analysis of quasielastic light scattering in LiNbO3 near T_C.* Phys. Rev. B, vol. 32: 6787–6792, 1985.

[123] Zhang, M.-s. and Scott, J. F. *Analysis of quasielastic light scattering in LiTaO3 near T_C.* Phys. Rev. B, vol. 34: 1880–1883, 1986.

[124] Hlinka, J., Ostapchuk, T., Nuzhnyy, D., Petzelt, J., Kuzel, P., Kadlec, C., Vanek, P., Ponomareva, I. and Bellaiche, L. *Coexistence of the phonon and relaxation soft modes in the terahertz dielectric response of tetragonal BaTiO3.* Physical Review Letters, vol. 101(16): 167402, 2008.

[125] Matthias, B. T. and Remeika, J. P. *Ferroelectricity in the ilmenite structure.* Phys. Rev., vol. 76: 1886–1887, 1949.

[126] Kaminow, I. P. and Johnston, W. D. *Quantitative determination of sources of the electro-optic effect in LiNbO3 and LiTaO3.* Phys. Rev., vol. 160: 519–522, 1967.

[127] Chang, T. S., Johnson, B. C., Amzallag, E., Pantell, R. H., Rokni, M. and Wall, L. S. *Temperature dependence of polariton dispersion in LiTaO3.* Optics Communications, vol. 4(1): 72 – 74, 1971.

[128] Bakker, H. J., Hunsche, S. and Kurz, H. *Time-resolved study of phonon polaritons in LiTaO3.* Phys. Rev. B, vol. 48: 13524–13537, 1993.

[129] Brennan, C. J. and Nelson, K. A. *Direct time-resolved measurement of anharmonic lattice vibrations in ferroelectric crystals.* The Journal of Chemical Physics, vol. 107(22): 9691–9694, 1997.

[130] Cavalieri, A., Wall, S., Simpson, C., Statz, E., Ward, D. W., Nelson, K. A., Rini, M. and Schoenlein, R. W. *Tracking the motion of charges in a terahertz light field by femtosecond X-ray diffraction.* Nature, vol. 442(7103): 664–666, 2006. 10.1038/nature05041.

[131] Schoenlein, R. W., Chattopadhyay, S., Chong, H. H. W., Glover, T. E., Heimann, P. A., Shank, C. V., Zholents, A. A. and Zolotorev, M. S. *Generation of femtosecond pulses of synchrotron radiation.* Science, vol. 287: 2237, 2000.

[132] Khan, S. *Free-electron lasers.* Journal of Modern Optics, vol. 55(21): 3469–3512, 2008.

[133] Zhavoronkov, N., Gritsai, Y., Bargheer, M., Woerner, M. and Elsaesser, T. *Generation of ultrashort K-alpha radiation from quasipoint interaction area of femtosecond pulses with thin foils.* Applied Physics Letters, vol. 86(24): 244107, 2005.

[134] Elsaesser, T. and Woerner, M. *Photoinduced structural dynamics of polar solids studied by femtosecond X-ray diffraction.* Acta Crystallographica Section A, vol. 66(2): 168–178, 2010.

[135] Tsen, K.-T., Song, J.-J., Betz, M. and Elezzabi, A. Y. (editors). *Time-resolved X-ray scattering*, vol. 7937, (SPIE2011).

[136] Hannaford, P. *Femtosecond Laser Spectroscopy*, (Springer2005).

[137] Khan, S., Holldack, K., Kachel, T., Mitzner, R. and Quast, T. *Femtosecond undulator radiation from sliced electron bunches.* Phys. Rev. Lett., vol. 97: 074801, 2006.

[138] *Dr. Markus Gühr (Stanford)–private communication.*

Danksagung